

IMPACTS OF VOLCANIC ERUPTIONS AND GEOENGINEERING
ON ARCTIC CLIMATE

By

MIRA BERDAHL

A Dissertation submitted to the
Graduate School-New Brunswick
Rutgers, The State University of New Jersey
in partial fulfillment of the requirements
for the degree of
Doctor of Philosophy

Graduate Program in Atmospheric Science

written under the direction of

Alan Robock

and approved by

New Brunswick, New Jersey

May, 2014

ABSTRACT OF THE DISSERTATION

Impacts of Volcanic Eruptions and Geoengineering on Arctic Climate

By

MIRA BERDAHL

Dissertation Director:

Alan Robock

Stratospheric aerosols can produce large radiative forcing and climate response, often amplified in the Arctic. Here I study the Arctic response to natural (volcanic eruptions) and potential anthropogenic (geoengineering) stratospheric sulfate aerosols. I use a regional climate model and global climate model output from two modeling intercomparison projects. First, I investigate the relative impacts of changes in radiation and advection on snow extent over Baffin Island with the Weather Research and Forecasting model. Model results show it is possible to suddenly lower the snowline by amounts comparable to those seen during the Little Ice Age with an average temperature decrease of -3.9 ± 1.1 K from present. Further, sea ice expansion following large volcanic eruptions would have significant effects on inland temperatures, especially in the fall. Next, I analyze Last Millennium simulations from the Paleoclimate Modeling Intercomparison Project 3 to assess whether state-of-the-art global climate models produce sudden changes and persistence of cold conditions after large volcanic eruptions as inferred by geological records and previous climate modeling. North Atlantic sea ice and Baffin Island snow cover showed large-scale expansion in the simulations, but none of the models produced significant centennial-scale effects. Warm Baffin Island summer climates stunt snow expansion in some models completely, and model topography misses the critical elevations that could sustain snow on the island. This has critical

consequences for ice and snow formation and persistence in regions such as the Arctic where temperatures are near freezing and small temperature changes affect the state of water. Finally, I analyze output from the Geoengineering Modeling Intercomparison Project to examine whether geoengineering by injection of sulfate aerosols into the lower stratosphere prevents the demise of minimum annual sea ice extent, or slows spring snow cover loss. Despite geoengineering September sea ice and summer snow extents still decrease, although not as quickly as in the global warming scenario. Because of the climate system lag in responding to the existing radiative forcing, to stop Arctic sea ice and snow from continuing to melt, the imposed forcing would have to be large enough to also counteract the existing radiative imbalance.

MY CONTRIBUTION TO THE WORK

We wrote three journal articles based on this dissertation work. The first and second paper were inspired by the field and modeling work by Dr. Gifford Miller and his colleagues at the University of Colorado-Boulder. His field work on Baffin Island over the past decade suggested that there was a sudden expansion of ice caps after closely spaced eruptions near the onset of the Little Ice Age. Further modeling work using a global climate model suggested a mechanism for long term North Atlantic cooling after multiple volcanic eruptions each with transient affects.

The first project I did was to use a regional climate model to examine the snow line sensitivity to a variety of changes in boundary conditions that were meant to simulate conditions after a large volcanic eruption [*Berdahl and Robock, 2013a*]. Dr. Robock had the idea to use a regional climate model so that we could better resolve snowline evolution than the global climate models do. I learned to run the Weather Research and Forecasting (WRF) model for extended simulation periods (6 months), analyzed the results, produced all of the graphics and conclusions, and wrote my first article titled “Baffin Island snow extent sensitivity: Insights from a regional climate model,” now published by the *Journal of Geophysical Research – Atmospheres*. Dr. Robock was involved in general discussion during the course of the project and contributed to editing the manuscript. Dr. Miller contributed the useful idea to compare WRF runs relative to each other rather than to the actual climate since the model could not correctly simulate it due to insufficient cloud production. Dr. Robinson was generous with time, helping me understand the snow cover observations from the Interactive Multisensor Snow and Ice Mapping System (IMS). Michael Barlage from NCAR was helpful in explaining how

WRF handles snow cover and Aaron Wilson from Ohio State University helped with cloud fraction calculations.

My second project was motivated by the same suggestion that the LIA could be triggered by successive volcanic eruptions in the late 13th century [Berdahl and Robock, 2013b]. Since the work of Dr. Miller and his colleagues had used a global climate model, I decided to analyze the last millennium simulations for their response to eruptions during that time period. These simulations had already been run as part of the Paleoclimate Modeling Intercomparison Project 3 (PMIP3). The simulations covered the past 1000 years (850-1850 C.E.), and included volcanic aerosol loading from reconstructions as part of their external forcing. The models were run by a variety of groups around the world, and their output was available for download through the Earth System Grid Federation (ESGF). I synthesized and analyzed the data for this project, produced all of the graphics and conclusions, and wrote the manuscript. Dr. Robock was involved in general discussions throughout and editing of the manuscript. Reto Ruedy was helpful in explaining how to compute historical GISS temperatures from anomalies. The paper, titled “Northern Hemispheric cryosphere response to volcanic eruptions in the Paleoclimate Modeling Intercomparison Project 3 last millennium simulations,” is now published by the *Journal of Geophysical Research – Atmospheres*.

The third study in this dissertation was to examine the effects of sulfate geoengineering on the Arctic cryosphere [Berdahl et al., 2014]. I knew Dr. Robock’s other work focused on geoengineering, and I wanted to look at the effects on the Arctic by the more realistic geoengineering scenarios, since no one had focused on this region specifically for the cases I was interested in. I used the modeling output from the

Geoengineering Modeling Intercomparison Project (GeoMIP), also available for download on the ESGF. David Robinson provided me with the snow cover data from the Rutgers University Snow Lab. I prepared and analyzed the data, produced the graphics and conclusions and wrote the manuscript with help from Dr. Robock on the general synthesis and editing of the paper. We included the modelers for each model used in the analysis as co-authors on this paper. They were helpful in providing editorial comments on the manuscript before submission and in the review process. This manuscript, titled “Arctic Cryosphere Response in the Geoengineering Modeling Intercomparison Project (GeoMIP) G3 and G4 scenarios,” is now accepted to the *Journal of Geophysical Research – Atmospheres* as part of the GeoMIP Special Issue.

ACKNOWLEDGMENTS

There are a multitude of people at Rutgers to whom I owe thanks for their support and guidance during the past four years. First and foremost, to Alan Robock, for knowing when I needed extra pressure to move things along and when to allow me to work at my own pace. His understanding during the ‘WRF Days’ and his continual support and direction in the years that followed helped this thesis come together.

Of course, the rest of my committee has been nothing but supportive during my years at Rutgers. Both Åsa Rennermalm and Dave Robinson, warmly welcomed me into their research communities from the beginning. We have had plenty of useful and insightful conversations for which I am deeply grateful. I also genuinely appreciate Giff Miller’s willingness to share original ideas and helpful advice whenever and wherever we were able to meet, from Boulder to Montreal, Selfoss to San Francisco.

My time in New Jersey has been made all the more rich by the friends I’ve made while here. Stephen Nicholls was essential in getting me started with the WRF – without him I wouldn’t have survived the many months of segmentation faults. I am grateful to have met my academic confidant, Lili Xia, with whom I’ve shared every milestone in the last four years. And of course, the Princeton crew: Caroline, Bethel, Liliana, Albert, Colin, Christina, Matt, Sebastian, Iain, Lolly and all the others in Princeton who have made me part of their family.

My family has almost everything to do with my alleged grounded and sane nature during this more difficult of passages in life. Verizon Communications has surely taken a loss with its ‘Unlimited North America’ plan given the number of times I’ve dialed the

519, 905, 914 and 403 area codes. From the beginnings at Grewenow to my final hurrah at Rutgers, my parents have taught me the discipline, heart and wit it takes to complete any level of academic achievement. This PhD is as much theirs as it is mine. My brother and sister, always slightly older and wiser than me, have, as ever, provided me with their humor-laced advice and perspective during these trailer park days. Hvala, hvala.

Finally, for my husband Andrew, fawning thanks are insufficient. He carried me through this PhD as he carries me through this life.

This work was supported by NSF grants ARC-0908834 and AGS-1157525.

TABLE OF CONTENTS

ABSTRACT OF THE DISSERTATION	ii
MY CONTRIBUTION TO THE WORK.....	iv
ACKNOWLEDGMENTS.....	vii
TABLE OF CONTENTS.....	ix
LIST OF TABLES.....	xi
LIST OF FIGURES.....	xii
CHAPTER 1: INTRODUCTION.....	1
1.1 Volcanic Eruptions and Climate	2
1.2 Arctic Climate of the Last Millennium.....	3
1.2.1 The Little Ice Age.....	5
1.3 Current and future Arctic climate change	8
1.3.1 Effects of Geoengineering on the Arctic in a high-CO ₂ World	10
1.4 Summary of dissertation work.....	12
CHAPTER 2: REGIONAL CLIMATE MODELING OF BAFFIN ISLAND SNOW EXTENT SENSITIVITY.....	15
2.1. Model, Experiments, and Data	15
2.1.1 Model Description.....	15
2.1.2 Experimental Approach	18
2.1.3. Data.....	19
2.2. Results.....	21
2.2.1. Assessing the Control Run.....	21
2.2.2. WRF Experiments.....	27
2.3 Discussion.....	34
2.4. Conclusions	36
CHAPTER 3: ARCTIC CRYOSPHERE RESPONSE TO VOLCANIC ERUPTIONS IN THE LAST MILLENNIUM PMIP3 SIMULATIONS	39
3.1 Methods.....	39
3.2 Results.....	42
3.2.1 Hemispheric, Arctic and Regional Temperatures	42
3.3 Sea Ice	44

3.4 Model Elevation	46
3.5 Model Response to Volcanic Eruptions in the Last Millennium	47
3.5.1 Temperature	47
3.5.2 Sea Ice	48
3.5.3 Snow.....	49
3.5.4 Model Sensitivity.....	50
3.6 Discussion.....	51
3.7 Conclusions	55
CHAPTER 4: ARCTIC CRYOSPHERE RESPONSE TO GEOENGINEERING	57
4.1 Methods.....	57
4.2 Results.....	59
4.2.1 Temperature	59
4.2.2 Sea Ice	61
4.2.3 Snow Response	64
4.3 Summary	65
4.4 Discussion and Conclusions	67
CHAPTER 5: SUMMARY AND DISCUSSION.....	69
5.1 Summary	69
5.2 Discussion.....	72
REFERENCES.....	75
TABLES.....	87
FIGURES.....	97

LIST OF TABLES

2.1	Weather station locations, elevation and record frequency.....	82
2.2	Correlation between WRF Control Run near-surface temperature and station temperature with and without seasonal cycle removed.....	83
2.3	Minimum snow cover percent for each WRF run.....	84
3.1	PMIP3 Last Millennium modeling groups, volcanic and solar forcing.....	85
3.2	Top 10 eruptions ranks for <i>Gao et al.</i> [2008] and <i>Crowley et al.</i> [2008] datasets based on aerosol optical depth.....	86
3.3	Temperature, sea ice and snow anomaly response per unit forcing integrated from year 0 to year 10 lag after the eruption.....	87
4.1	Models participating in GeoMIP and the number of ensemble members run for each model.....	88
4.2	Arctic amplification measures for annual, summer and fall averages.....	89
4.3	Percent of September sea ice loss prevented by the geoengineering experiments in the last decade of geoengineering.....	90
4.4	Change of snow extent from 2020 to 2070 in April, May and June.....	91

LIST OF FIGURES

1.1	Schematic of volcanic inputs to the atmosphere.....	92
1.2	Composite proxy reconstruction of Northern Hemisphere temperatures for the last two millennia.....	93
1.3	Arctic summer temperature anomaly based on proxy records.....	94
1.4	Climate model results from [Miller <i>et al.</i> 2012].....	95
1.5	Average monthly Arctic sea ice extent from satellite observations.....	96
1.6	Schematic of geoengineering experiments from GeoMIP.....	97
2.1	Map of WRF domains.....	98
2.2	2 m station and WRF Control run mean, maximum and minimum daily temperatures.....	99
2.3	Mean monthly station near-surface temperature bias.....	100
2.4	Monthly average cloud fraction from WRF and MODIS.....	101
2.5	Observed and modeled sea ice cover	102
2.6	Observed and modeled snow cover.....	103
2.7	Bias vs. RMSE between station and WRF for 2 m temperature from April-Sept 2005.....	104
2.8	Monthly average temperature difference between WRF Control Run and sensitivity experiments.....	105
2.9	Minimum snow extent maps for each cooling experiment.....	106
2.10	Fraction of snow-covered area on minimum extent day as a function of elevation.....	107
2.11	Minimum snow line elevation as a function of average 6 month temperature difference between Control Run and cooling experiments.....	108
3.1	Map showing Arctic, North Atlantic and Baffin Island.....	109
3.2	JJA temperature time series for PMIP3 simulations in the Northern Hemisphere, Arctic and Baffin Island.....	110

3.3	Comparison of paleoclimate temperature reconstructions to PMIP3 temperatures.....	111
3.4	Comparison of reconstructed August sea ice extent with PMIP3 sea ice.....	112
3.5	North Atlantic sea ice extent anomalies for PMIP3 models.....	113
3.6	Modeled representation and actual elevation distributions for Baffin Island.....	114
3.7	Superposed temperature anomaly response to top 10 eruptions in the last millennium.....	115
3.8	Superposed sea ice area anomaly response to top 10 eruptions in the last millennium.....	116
3.9	Superposed snow anomaly response to top 10 eruptions in the last millennium.....	117
3.10	Snow response after eruptions compared to mean model summer climate.....	118
4.1	Global annual average temperatures for RCP4.5, G3 and G4.....	119
4.2	Summer average temperature for Arctic in RCP4.5, G3 and G4.....	120
4.3	Summer temperature trend from 2030 to 2070 in the Northern Hemisphere for RCP4.5, G3 and G4.....	121
4.4	Summer temperature trend from 2070 to 2090 in the Northern Hemisphere for RCP4.5, G3 and G4.....	122
4.5	March and September sea ice extent for RCP4.5, G3 and G4.....	123
4.6	Arctic sea ice extent anomaly for G3 and G4 with respect to RCP4.5.....	124
4.7	Mean September sea ice extent maps before and after geoengineering.....	125
4.8	Monthly sea ice extent by decade.....	126
4.9	Monthly sea ice volume by decade.....	127
4.10	Spring snow cover extent for Northern Hemisphere for RCP4.5, G3 and G4....	128

CHAPTER 1: INTRODUCTION

Recent surface temperature increases as a result of anthropogenic greenhouse gas emissions have been faster in the Arctic than the global average. This characteristic feature of the high north, coined “Arctic Amplification,” was first predicted by Svante Arrhenius in 1896, who mused that increased carbon dioxide (CO₂) would cause greater warming at higher latitudes [Arrhenius, 1896]. Although Arrhenius (correctly) suspected that this was due to the albedo feedback, there are more aspects to the Arctic climate system that make it particularly reactive to changes in climate forcings. In addition to the albedo feedback, the Arctic gives rise to and is affected by the sea ice feedback, permafrost feedback, vegetation feedback, and the cloud cover and water vapor feedbacks [Miller *et al.*, 2010; Serreze *et al.*, 2011]. All of these processes combine to create a region that is highly sensitive to changes in climate forcings, such as volcanic eruptions or anthropogenic CO₂ changes [Serreze *et al.*, 2011].

This dissertation consists of three studies with the objective of understanding how the Arctic climate system might respond to changes in climate forcings, both in the past and future. The first two serve to better understand the overarching question of whether a sequence of large volcanic eruptions in the late 13th Century CE initiated the Little Ice Age [Miller *et al.*, 2012]. Specifically, this work intends to address the following scientific questions:

- 1) What causes variations in summer snow extent over Baffin Island? What are the relative contributions of changes in radiation and advection?

2) Do state-of-the-art global climate models produce the observed sustained centennial-scale cold anomalies and expanded sea ice and snow cover in the North Atlantic and Baffin Island regions following multiple, successive large volcanic eruptions? If not, why not?

3) Would geoengineering by injection of sulfate aerosols into the lower stratosphere from the years 2020 to 2070 prevent the demise of minimum annual sea ice extent or slow spring snow cover loss?

1.1 Volcanic Eruptions and Climate

It is well-understood that the effects of volcanic aerosol loading into the stratosphere are transient, with global cooling lasting only a few years after a single large eruption [Robock, 2000]. Explosive volcanoes can inject sulfur dioxide (SO_2) and hydrogen sulfide (H_2S) species into the stratosphere which react with hydroxide (OH) and water (H_2O) to form sulfuric acid (H_2SO_4) on timescales of about a week [Pollack et al., 1976; Robock, 2000]. H_2SO_4 is the dominant byproduct of such eruptions that acts to modify the radiative balance. Figure 1.1 shows a schematic of the major processes for both quiescent and explosive eruptions. There is a net global cooling at the surface after explosive eruptions, which models can successfully reproduce [Hansen et al., 1992], and stratospheric warming that lasts about 1-3 years. In the year after the Mount Pinatubo eruption in 1991 which injected 20 Tg of sulfate aerosols in the stratosphere [Robock et al., 2008; Bluth et al., 1992], globally averaged surface air temperature was reduced by approximately 0.5°C [Lacis and Mishchenko, 1995].

There are also seasonal and hemispheric effects. Following a tropical eruption, winters in North America, Europe and Siberia tend to be warmer while summers are cooler due to both radiative and dynamic effects [*Robock and Mao, 1992; Robock, 2000*]. Such eruptions may produce a stratospheric temperature gradient since heating of the tropical stratosphere is stronger than that at higher latitudes [*Robock, 2000*]. This in turn can induce a stronger jetstream and consequently a stronger polar vortex. A stronger polar vortex amplifies the North Atlantic Oscillation (NAO) circulation, whereby the Icelandic Low and the Azores High strengthen, causing winter warming of northern hemisphere continents that can exceed the direct radiative effects of the eruption [*Robock, 2000*].

Given that a single explosive eruption has an interannual effect on climate, multiple successive eruptions could cause decadal-scale cooling given the accumulation of stratospheric sulfate aerosol concentrations. Furthermore, systems with longer memory such as oceans and sea ice could feedback and perpetuate the volcanically induced cooling [e.g., *Mignot et al., 2011; Miller et al., 2012*].

1.2 Arctic Climate of the Last Millennium

Earth's temperature history over the past millennium provides a critical framework for accurately generating and understanding projections of future change. Northern Hemisphere (NH) proxy reconstructions over this period [e.g. *Jones et al., 1998; Briffa et al., 2001; Mann et al., 2009, 2008; Jansen et al., 2007*] have large uncertainties and show variable timing, amplitude, and spatial extent of multidecadal events such as the Little Ice Age (LIA, circa 1300–1850 Common Era (C.E.)) and the

Medieval Climate Anomaly (circa 900–1250 C.E.) [*Frank et al.*, 2010; *Miller et al.*, 2010] (Figure 1.2). Over the last millennium, volcanic eruptions and solar variability are the two primary natural drivers of forced climate variability [*Schneider et al.*, 2009]. Volcanism is the most prominent natural forcing factor for climate variability of the last 700 years [*Hegerl et al.*, 2007]. In concert, volcanism and solar variability can explain much of the decadal to centennial-scale surface temperature reconstructions in the Northern Hemisphere [*Amman et al.*, 2007].

Climate proxies from the Arctic generally reflect summer temperature anomalies, for example from lake sediment cores, tree rings, or radiocarbon dating of entombed vegetation along the margins of receding ice caps [*Kaufman et al.*, 2009; *Miller et al.*, 2010]. Ice cores typically reflect mean annual temperatures. From these proxy records, it is understood that Arctic temperature changes have been greater than the Northern Hemisphere average, both during summer and annually averaged. In general, there is broad agreement among proxies over the past millennium: they show modest summer warmth during Medieval Period followed by a fluctuating but colder climate from about 1250-1850 CE. The instrumental period indicates unprecedented warming which is also confirmed in paleoclimate records [*Miller et al.*, 2010].

Kaufman et al. [2009] present an integration of decadal resolved proxy temperature records from 23 sites across the Arctic which record back at least 1000 years from present (Figure 1.3). Based on this proxy evidence, they found that pervasive Arctic cooling dominated the past 2 millennia. They confirmed this using the Community Climate System Model, and attribute the cooling to an orbitally-driven reduction in summer insolation. This long-term cooling was reversed during the 20th

century, with four of the five warmest decades in the past 2 millennia occurring between 1950 and 2000.

1.2.1 The Little Ice Age

The Little Ice Age (LIA) occurred in fits and starts between the 13th and 19th centuries, although clues from the field suggest regional variability in timing, location and magnitude. In the Arctic, the LIA caused expansion of ice caps and glaciers to their largest extents in the past 8000 years [Miller *et al.*, 2010], but it is still unclear what triggered and sustained the transition into a colder climate. Field studies since the 1960s have noted that in areas of Baffin Island, in the eastern Canadian Arctic, sparse lichen cover over large areas could indicate that widespread glacierization was so recent that little recolonization had yet taken place [Ives, 1962; Andrews *et al.*, 1972; Williams, 1978a]. In north central Baffin Island, the terrain is a shallowly undulating plateau with an elevation range of 400–700m [Andrews *et al.*, 1972]. Lowering the snow line into this zone could cause a drastic increase in area of snow coverage. This region of Baffin Island is where the LIA snow expanded and could even have been where the Laurentide ice sheet originated [Miller, 1973; Williams, 1978a]. It is thus important to understand the sensitivity of snow cover to temperature changes in a highly responsive region such as Baffin Island.

Proxy-based evidence recently collected from ice caps on Baffin Island suggests that a sudden expansion of ice caps began soon after a succession of several large eruptions in the 13th century, the approximate onset of the LIA [Anderson *et al.*, 2008; Geirsdóttir *et al.*, 2009; Zhong *et al.*, 2010; Miller *et al.*, 2012]. The paleoclimate proxies

show intermittent ice melt and growth between the late thirteenth century and mid-fifteenth century, followed by continuous ice cover from the mid-fifteenth century until roughly a century ago. The sudden cooling in the mid-thirteenth century coincides with four roughly decadal paced eruptions, the first of which was the 1257 Samalas eruption [Lavigne *et al.*, 2013], the largest eruption in the last 7000 years [Langway *et al.*, 1988].

Using the Community Climate System Model-3 (CCSM3) at T42 (about 2.8° horizontal resolution, Zhong *et al.* [2010] found that it was possible to induce long-term North Atlantic wide cooling with only transient volcanic aerosol forcing. The mechanism found in the model to account for this widespread drop in temperature was a coupled sea ice ocean feedback, wherein an expanded sea ice state perpetuated the typically short-lived effects of explosive volcanism [Robock, 2000]. Zhong *et al.* [2010] found that under particular stability scenarios of the upper North Atlantic (NA) Ocean, the CCSM3 simulations were able to induce abrupt snowline depressions and sustained expanded snow and ice conditions on centennial time-scales. In particular, after the 1257 Samalas eruption, sea surface temperatures (SSTs) in the NA never recovered to their pre-eruption temperatures, as several more large and closely spaced volcanoes erupted and caused cumulative cooling. Cooler NA surface water was then advected to the Atlantic sector of the Arctic Ocean, reducing the rate of basal sea ice melt and allowing sea ice to remain in an expanded state for more than 100 years. Ship records corroborate this with evidence that severe summer ice occurred in the years immediately following large volcanic eruptions during the 19th century [Catchpole *et al.*, 1989]. Miller *et al.* [2012] expanded on the results from Zhong *et al.* [2010] and showed that large changes in irradiance are not required to produce persistent cold summers in Arctic Canada. Such

cooling is best explained by sea ice/ocean feedbacks after an anomalous 50-year period of explosive volcanic activity. Figure 1.4 shows results from *Miller et al.* [2012] illustrating their modeling results which produce long term sea ice expansion, decreased northward heat transport in the North Atlantic and decreased summer surface air temperature over North Atlantic Arctic land as a result of volcanic perturbations only.

Proxy records [*Briffa et al.*, 1998] and other modeling experiments have also suggested that it is possible to induce long-term cooling given closely spaced multiple volcanic eruptions. *Mignot et al.* [2011] found results consistent with the *Miller et al.* [2012] and *Zhong et al.* [2010] findings. Post-thirteenth century eruptions, *Mignot et al.* [2011] found a weakened Atlantic Meridional Overturning Circulation and a sustained cooling and sea ice expansion in the North Atlantic region. *Schleussner and Feulner* [2013] suggest that an increase in Nordic sea ice extent on decadal timescales as a consequence of major eruptions leads to a spin-up of the subpolar gyre and a weakened Atlantic Meridional Overturning Circulation, eventually causing a persistent basin-wide cooling.

Entombed vegetation collected from the margins of ice caps in north central Baffin Island and analyzed by *Miller et al.* [2012] suggests two periods during the descent into the LIA with sudden advances in snow line. The first, from 1275 to 1300 CE, reveals sites in an elevation range of 660–1000 m and the second from 1430 to 1455 CE from sites in a range of 660–900 m elevation. That is, there was a sudden and persistent drop in snow line by about 300 m in a matter of only a few decades. Since the most reliable summer temperature proxies at high northern latitudes are glaciers, where 90% of their mass balance variation can be explained by summer temperature [*Koerner,*

2005], ice cap advances or recessions inform us about the local summer temperature. Based on these proxy climate reconstructions and their previous climate modeling results, *Miller et al.* [2012] suggested that the LIA onset was an abrupt event late in the 13th century which intensified later in the 15th century and that it could be explained by repeated explosive volcanism.

1.3 Current and future Arctic climate change

The Arctic has been warming twice as quickly as the global average in recent decades [e.g., *Serreze and Francis, 2006; Solomon et al., 2007*] and three times as quickly as the average of all other non-polar regions of the world [*Ahmed et al., 2013*] – a characteristic known as Arctic Amplification. Recent work by *Miller et al.* [2013] suggests that 5000 years of regional summertime cooling in Arctic Canada has been reversed, with average summer temperatures of the last century now higher than during any century in more than 44,000 years, including the peak warmth of the early Holocene when high-latitude summer insolation was 9% greater than current. One of the major concerns associated with such extreme rates of warming is the demise of Arctic sea ice. All monthly extents of Arctic sea ice have declined over the period of observations, most rapidly for September (Figure 1.5) [*Serreze et al., 2007*]. This decline has been shown to be congruent with strong surface warming [*Screen and Simmonds, 2010*]. For example, *Tingley and Huybers* [2013] showed that the summers of 2005, 2007, 2010, and 2011 were warmer than those of all prior years back to 1400 in the high northern latitudes. These years are also associated with very low minimum sea ice extents [*NSIDC, 2013*]. *Serreze et al.* [2009] and *Screen and Simmonds* [2010] demonstrated that strong positive

ice-temperature feedbacks have already emerged in the Arctic, increasing the chances of further warming and ice loss. The Coupled Model Intercomparison Project (CMIP5) models range in estimates for when ice-free conditions will occur, some predicting as early as 2020 [Stroeve *et al.*, 2012; Wang and Overland, 2012]. Stroeve *et al.* [2012] found that, even with the same emissions scenario, there is large scatter between different model simulations (both between different models and between ensemble members from the same model) as to the timing of a seasonally ice-free Arctic Ocean. Under the same emissions scenario, models project this could occur as early as 2020 or well beyond 2100. Uncertainty in future greenhouse gas emissions leads to further uncertainty regarding when ice free conditions will occur.

Along with the rapid deterioration of Arctic sea ice, Arctic snow cover on land has also been quickly receding over the past several decades. Derksen and Brown [2012] found statistically significant reductions in May and June Arctic snow cover extent from 1967-2012. They also noted that the rate of June snow cover loss between 1979 and 2011 is greater than the loss of September sea ice extent over the same period, emphasizing the importance of the observed changes. As with sea ice, Brown and Robinson [2011] showed that significant reductions observed in Northern Hemisphere spring snow cover extent over the past 90 years are mainly driven by warmer temperatures. Projections for future spring snow cover duration suggest a decrease by about 10–20% over much of the Arctic by the year 2050 [Callaghan *et al.*, 2011]. Observed changes in the Arctic could have further reaching implications than just physical effects. Losses in Arctic sea ice and earlier snow melt on high-latitude land have been linked to more persistent mid-latitude weather patterns, which may lead to an

increased probability of extreme weather events [*Francis and Vavrus, 2012*]. Further, the permanent loss of permafrost, and increases in active layer thickness do not only have consequences for transportation and the livelihood of high-latitude communities, but the thaw and release of carbon from the ground may amplify surface warming and initiate a positive permafrost carbon feedback on climate [*Schaefer et al., 2011*].

1.3.1 Effects of Geoengineering on the Arctic in a high-CO₂ World

Geoengineering has been proposed in recent literature as a way to curb global warming and reduce some of the risks associated therein [e.g., *Lauder and Thompson, 2009*]. *Crutzen [2006]* suggested that artificial reduction of incoming solar radiation, called Solar Radiation Management (SRM) [*Lane et al., 2007*], could be a means of offsetting the effects of increasing greenhouse gas concentrations by reducing solar absorption [*Shepherd et al., 2009*]. Several SRM approaches have been suggested, but *Lenton and Vaughan [2009]* contend that among the most effective would be by stratospheric aerosol injection. The possible regional effects are still uncertain. *Robock et al. [2008; 2009]* and *Tilmes et al. [2008]* identify the possibility of unintended consequences such as ozone depletion and disruptions to the global hydrologic cycle. Although large volcanic eruptions show a dynamical response to stratospheric heating, such as winter warming over the Northern Hemisphere continents, *Robock et al. [2008]* did not find such responses in their simulations of sulfate aerosol geoengineering. It is thus of paramount interest to assess the effects of geoengineering on the Arctic, given its high sensitivity to increases in greenhouse gases and the weighty consequences of continued warming.

Previous work on the effects of geoengineering showed warmer poles and cooler tropics with respect to preindustrial conditions [Lunt *et al.*, 2008; Govindasamy and Caldeira, 2000; Matthews and Caldeira, 2007]. Yet, certain geoengineering scenarios produce a reduction in the melt of sea ice [Kravitz *et al.*, 2013] and ice sheets [Irvine *et al.*, 2009] compared to the preindustrial. These inconclusive results, partly due to differing experiments and models, spurred the Geoengineering Model Intercomparison Project (GeoMIP) [Kravitz *et al.*, 2011a]. GeoMIP constitutes a suite of 4 SRM experiments, aimed at understanding how geoengineering might offset climate change projected in some of the CMIP5 experiments.

Figure 1.6 shows a schematic of the four GeoMIP experiments. Of these, G3 and G4 represent the more “realistic” scenarios in that they use the RCP4.5 [representative concentration pathway, with a radiative forcing of 4.5 Wm^{-2} in the year 2100; Moss *et al.*, 2010] global warming scenario as the control run, and they model stratospheric aerosol injection rather than insolation reduction. Whereas G1 and G2 balance top of atmosphere radiation by reducing the solar constant to a lower value, the G3 experiment adds stratospheric aerosol gradually to the lower stratosphere. Prior to GeoMIP, only a handful of independent studies using general circulation models have simulated SRM scenarios by injection of SO_2 into the lower stratosphere [Robock *et al.*, 2008; Rasch *et al.*, 2008; Jones *et al.*, 2010; Niemeier *et al.*, 2011].

G3 injects sulfate aerosols beginning in 2020 to balance the anthropogenic forcing and attempts to keep the net forcing constant (at 2020 levels) at the top of the atmosphere [Kravitz *et al.*, 2011a]. The G4 experiment is similar to G3 in simulating a stratospheric sulfate layer beginning in 2020, but it does not attempt radiative balance with

anthropogenic emissions. Rather, it injects stratospheric aerosols at a rate of 5 Tg SO₂ per year to effectively delay global warming by about 40 years [Kravitz *et al.*, 2011a]. This may be compared with the 20 Tg of SO₂ injected into the stratosphere by the 1991 eruption of Mount Pinatubo [Robock *et al.*, 2008; Bluth *et al.*, 1992]. Both G3 and G4 cease sulfate aerosol injection in 2070, and the models then continue to run from 2070 for at least 20 more years, such that the post-engineered rebound of the climate system can be assessed. Large volcanic eruptions that inject sulfate aerosols into the stratosphere with an e-folding decay time of approximately 1 year [e.g. Barnes and Hoffman, 1997] can cause global cooling for up 2 or 3 years [Robock, 2000]. Similarly short aerosol lifetimes are expected with the G3 and G4 sulfate injections such that a sudden suspension of SRM will cause a rapid rebound in the climate. Whereas in G1 and G2 the forcing disappears immediately when insolation is returned to the control value, in G3 and G4 there is a delay of 1-2 years as the aerosol forcing gradually disappears. For a more technical overview of GeoMIP experiment specifications, refer to Kravitz *et al.* [2011b].

1.4 Summary of dissertation work

In this thesis, I address Arctic climate change of the past and future. Motivated by the modeling and proxy data described in Zhong *et al* [2010] and Miller *et al.* [2012] (presented in Section 1.2.1), Chapter 2 details how I used a regional climate model, the Weather Research and Forecasting Model (WRF) to examine the relative effects of radiation and advection on snow line altitude in the Northeastern Canadian Arctic. I present results from eight unique 6-month long high-resolution simulations with imposed

atmospheric temperature, solar constant, and sea ice perturbations, which are aimed to simulate what conditions may have led to the lowering of the snow line on Baffin Island. The experiments are designed to simulate conditions likely to have occurred after a series of volcanic eruptions, such as colder air temperatures, a reduction in surface radiation, and the expansion of sea ice.

In Chapter 3, I ask how the models of the Paleoclimate Modeling Intercomparison Project Phase 3 (PMIP3) last millennium simulations compare to paleoclimate reconstructions in the Arctic and Northern Hemisphere. I assess whether any of these global climate models produce the reconstructed and previously modeled sustained centennial-scale cold anomalies and expanded sea ice and snow cover in the North Atlantic and Baffin Island regions following multiple, successive large volcanic eruptions.

Chapter 4 focuses on future climate change and investigates the effects of sulfate aerosol geoengineering on Arctic climate by using output from the global climate models that participated in the Geoengineering Modeling Intercomparison Project (GeoMIP). I use the G3 and G4 experiments of GeoMIP to assess impacts on the Arctic. This way we benefit from a multi-model and multi-experiment comparison, each model having consistent inputs and parameters, and two unique sulfate aerosol experiments. I ask how much the Arctic would cool in the G3 and G4 scenarios, and whether geoengineering in a higher CO₂ world would prevent the demise of multi-year sea ice. I also examine the effects of geoengineering on the already decreasing Arctic spring snow cover on land. Furthermore, I examine the post-geoengineering period (after 2070) to see how the Arctic

cryosphere rebounds after the cessation of aerosol injection, deemed the “Termination Effect” [e.g., *Wigley, 2006; Jones et al., 2013*].

Finally, Chapter 5 presents a summary and conclusions based on the results in Chapters 2-4.

CHAPTER 2: REGIONAL CLIMATE MODELING OF BAFFIN ISLAND SNOW EXTENT SENSITIVITY

The field observations by *Miller et al.* [2012] motivated us to investigate how sensitive the snow line elevation is; specifically, what are the relative impacts of changes in radiation or advection on minimum summer snow extent over Baffin Island? We used a high-resolution regional climate model to allow improved representation of atmospheric and snow processes given the steep and complex terrain of Baffin Island. In this Chapter, we present results from eight unique 6-month long high-resolution simulations with imposed atmospheric temperature, solar constant, and sea ice perturbations, which are aimed to simulate what conditions may have led to the lowering of the snow line on Baffin Island. The experiments are designed to simulate conditions likely to have occurred after a series of volcanic eruptions, such as a reduction in cooling and surface radiation, and the expansion of sea ice. We ran all the simulations from April through September of 2005 to capture the full spring thaw through to the early fall. The results from Chapter 2 are published [*Berdahl and Robock, 2013a*] in the *Journal of Geophysical Research - Atmospheres*¹.

2.1. Model, Experiments, and Data

2.1.1 Model Description

We used the Advanced Research Weather Research and Forecasting (WRF-ARW) regional weather and climate model version 3.3 [*Skamarock et al., 2008*] for all

¹ Berdahl, M., and A. Robock (2013), Baffin Island snow extent sensitivity: Insights from a regional climate model, *J. Geophys. Res. Atmos.*, 118, 3506–3519, doi:10.1002/jgrd.50249.

simulations. The ARW core was chosen as it is used as a research tool at the National Center for Atmospheric Research, as opposed to the non-hydrostatic mesoscale model core that is used operationally at the National Centers for Environmental Prediction. The 2-way nested model was fixed for all experiments, with a parent domain of 30 km horizontal resolution encompassing much of northern Canada and Greenland, and the inner domain of 10 km resolution, hedging Baffin Island (Figure 2.1a). There were 27 vertical levels in the WRF runs, with a model top at 50mb. Each WRF simulation was run during the 6-month period of April-September 2005, a year without a strong North Atlantic Oscillation signal, typical Arctic minimum sea ice extent given the current decline, and relatively abundant remotely sensed data available. The results were compared to snow, cloud, and surface meteorological observations. Following *Hines et al.* [2011], we forced all runs with initial and boundary conditions from the National Centers for Environmental Prediction Global Forecasting System Final Analysis (GFS-FNL), which has a resolution of $1^\circ \times 1^\circ$. GFS-FNL provides input to WRF every 6 hours of model time, and the time step in WRF is 120 seconds.

The following parameterizations were used for all runs:

1. Noah land surface model (LSM) [*Chen and Dudhia, 2001*]
2. WRF Single Moment 5-class microphysics scheme [*Hong et al., 2004*]
3. Yonsei University planetary boundary layer scheme [*Hong et al., 2006*]
4. Goddard shortwave scheme [*Chou and Suarez, 1994*]
5. Rapid Radiative Transfer Model longwave scheme [*Mlawer et al., 1997*]
6. Kain Fritsch (new Eta) cumulus scheme [*Kain, 2010*]

These parameterizations were chosen after we ran a set of 1 month long sensitivity tests for July of 1981, where we tested variations of parameterization choices and found that this combination did a good job of reproducing the climate for one summer month in the region. A very similar combination of parameterization choices is recommended by *Hines and Bromwich* [2008] based on the performance of their Polar WRF experiments over the Greenland Ice Sheet. All of our simulations applied spectral nudging to the u and v windfields above the boundary layer (about 1500m altitude) to only the parent domain (the larger, 30 km resolution domain (Figure 2.1a)) as recommended by *Miguez-Macho et al.* [2004], since it has been shown to improve performance of Polar WRF [Cassano et al., 2011]. By nudging the u and v components of the wind, we maintain realism in the simulation while allowing temperature to remain a free parameter, since we want it to be predicted by the model.

Sea ice in the model is prescribed by the GFS boundary conditions, updated every 6 h of model time. Sea ice in WRF V3.3 is handled by the Noah LSM, and is treated much the same as land. The sea ice has a fixed thickness of 3 m, and is divided into four layers just as the land surface is, with thermal conductivities modified from land-relevant values to ice-relevant values. Sea ice in the model is always 100% snow covered, and the skin temperature above the ice is then calculated above the snow in the same way it is calculated over snow-covered land. Versions Polar WRF 3.2 and standard WRF 3.2.1 could not complete the full 6-month simulation without crashing with unexplained segmentation faults. When the domain boundaries were placed in regions without strong topography, standard WRF 3.3 ran without problems, so this was the version used for all of our simulations.

2.1.2 Experimental Approach

Since we are interested in sensitivity of snow extent to temperature perturbations, we performed eight experiments, the first of which was a Control Run where the model was forced with the GFS input data for the given time period. Four temperature experiments were run where the boundary conditions of the Control Run were perturbed for the full simulation by -1.5 K, -3 K, -4.5 K, and -6 K, and labeled the WRF -1.5 K, WRF -3 K, WRF -4.5 K, and WRF -6 K runs. By perturbing only the temperature of air in these runs, we only change one variable at a time, and thus, we know that any effects seen are purely from the advection of cooled air. However, we acknowledge that cooler air advected into the domain should be drier as well, but we did not remove moisture when cooling the boundaries. The model takes care of this “extra” moisture on its own by raining out at the boundaries of the parent (outer) domain so that air advected to the inner domain is drier in the cooled experiments than the Control Run. This drying effect increases with increasing temperature perturbation, as it should.

In the sixth experiment, we ran the Control Run again, but with the solar constant set to 1301 W/m², 95% of its current value, labeled 95SOLCON. This is approximately a -12 W/m² change in radiative forcing at the tropopause, about three times the effect immediately following the 1991 Mount Pinatubo eruption [McCormick *et al.*, 1995]. This run is another approach to cooling the domain, where instead of applying temperature perturbations to the boundary conditions only, in which the magnitude dissipates as it propagates into the inner domain a uniform perturbation is applied across the entire domain. It must be noted, however, that this experiment represents only a lower bound

on the effects of such a reduction in solar radiation since the boundary conditions feeding WRF are not subjected to the same reduction in radiation.

Motivated by the results from *Zhong et al.* [2010], where an expanded sea ice state was induced and sustained after four sequential volcanic eruptions took place in the 13th century, we ran the simulation with sea ice fixed to the 1 April state for the full 6 months (labeled FixedSI). Finally, we ran a simulation where we both applied the -3K temperature perturbation to the boundaries and fixed the sea ice to the 1 April state (WRF -3K and FixedSI). We hypothesized that this final run would allow the cooled boundary temperatures to remain colder as winds were advected across the sea ice and would represent more realistic LIA-type conditions where temperature drops and expanded sea ice occur in concert.

2.1.3. Data

In situ Environment Canada Automatic Weather Stations (AWS) observations in Nunavut, in addition to being sparse, tend to be biased toward low elevations, as most stations are along the coastline. This limits our ability to evaluate our high-resolution model output, but at the same time illustrates the necessity for running such models as a way to fill the gap in surface observations across the Island's interior. Here we focused on near-surface summer temperature output from the model, as it has been found to be the primary driver of high latitude glacier mass balance throughout most of the Holocene in parts of the eastern Canadian Arctic [*Koerner, 2005*].

In addition to temperature, we evaluated the evolution of snow cover extent. We compared our model runs to the 4 km resolution Interactive Multisensor Snow and Ice

Mapping System (IMS) satellite snow and sea ice cover daily data, from the National Climatic Data Center [National Ice Center, 2008], and Moderate Resolute Imaging Spectroradiometer (MODIS) Cloud Gap-Filled (CGF) Daily Snow Product at 0.5° horizontal resolution. As *Brown et al.* [2010] described, the IMS product is generated by trained analysts who use snow cover information from satellites, station observations, and passive microwave readings to create 4 km resolution maps for the entire Northern Hemisphere. Any cell containing more than 50% snow cover is classified as snow-covered. Since the product is predominantly derived from visible satellite imagery, it can be misleading during days of extensive cloud cover, a common occurrence during Arctic spring and summer. IMS maps have been documented to produce excessive snow cover fractions over the Arctic during the spring melt period. This artifact has been attributed to extensive cloud cover and less frequent satellite coverage over the Arctic [*Wang et al.*, 2005a; *Brown et al.*, 2007]. *Wang et al.* [2005a] also commented that the analysts have been trained to be “aggressive” with their snow cover classification, often designating areas of patchy snow as completely snow-covered.

We also used the MODIS CGF snow product for comparison to WRF, which is available between October and mid-June, and provides a daily snow coverage map irrespective of cloud cover [*Hall et al.*, 2010]. The product provides a snow-cover map based on the most recent clear-sky observation and gives each cell a confidence based on the number of days since the last recorded view.

Comparison of 10 km average (WRF), 4 km average (IMS), and point measurements (weather stations) should be interpreted with care. Area-averaged snow cover and temperature can be skewed in steep terrain. Much of Baffin Island’s coastline

is dramatic and contains sudden transition from sea level to high mountains and deeply carved fjords. Since most station locations are along the coast, low resolution grid cells would tend to smooth the transition from ocean to steep land. In their WRF modeling study of the Colorado Rockies, *Ikeda et al.* [2010] found that snowfall decreased at high elevations as model resolution became coarser. Since the higher resolution (2 km and 6 km) runs resolved the higher peaks in the mountain range, cooler conditions are simulated and thus snow lasted longer on the peaks than the lower resolution (18 km and 36 km) runs. We chose 10 km resolution in an effort to approach the high resolution suggested by *Ikeda et al.* [2010] while conserving computation expenses.

Gardner et al. [2009] derived an average ablation season lapse rate of 4.9 K/km from four ice caps in the Canadian Arctic. However, near-surface lapse rates over melting glaciers are often lower than those over land [*Greuell and Böhm*, 1998]. Thus, when comparing WRF to station data, we corrected surface temperatures produced by WRF with a standard lapse rate of 6 K/km [*Lucas-Picher et al.*, 2012].

2.2. Results

2.2.1. Assessing the Control Run

2.2.1.1. Temperature

It is first necessary to assess the quality of the WRF Control Run. As mentioned above, summer temperature is the primary control of glacier mass balance in our study region, so we first assess the quality of the model in terms of temperature. Table 2.1 shows the station names, locations, elevation, and frequency of record available at each site. Figure 2.1b shows the inner domain and the AWS station locations. There are six

available hourly AWS records of temperature in our 10 km resolution domain during April-September 2005. The other 11 stations record daily average temperature.

All WRF temperatures reported below were corrected with a lapse rate of 6 K/km [Lucas-Picher *et al.*, 2012] to match the closest WRF grid elevation to the elevation of the AWS to which it is being compared. Figure 2.2 shows the time series of observed and modeled minimum, maximum, and average 2 m temperatures at the six stations with hourly records. The only inland station available and one of the most poorly simulated locations by the model is Dewar Lakes. Despite a very high and significant correlation between the station and modeled temperature, the WRF Control Run at Dewar Lakes tends to over exaggerate the diurnal temperature cycle. Other stations show more faithful representations of temperatures. Table 2.2 shows the correlation coefficients, r , between 2 m temperature of the WRF Control run and the station records. All correlations presented in Table 2.2 are statistically significant, with p values of <0.01 (Student's t -test). Some stations have records of both hourly and daily average temperatures, so both are reported in this table. The correlation improves slightly for daily averaged temperature records. Table 2.2 also shows the correlation coefficient, r , after the seasonal cycle is removed. For the daily average data, this is a measure of how well the model captures the synoptic systems, and for the hourly data, it measures both the ability to model the diurnal cycle and the synoptic systems. The values are all statistically significant, and range between 0.40 and 0.69, suggesting WRF captures both diurnal and synoptic variations with fair accuracy.

We define the temperature bias as the difference between the WRF and the station data temperatures (WRF-Station). The mean monthly WRF Control Run bias at each of

the 17 available stations is shown in Figure 2.3a. The temperature bias of the Control Run, averaged over time and stations, is -0.3 K, consistent with the overall cold bias seen in results from *Wilson et al.* [2011], the cause of which is yet to be determined but is likely due to the land surface model. However, on average WRF tends to overestimate summertime temperatures and underestimate spring and fall season temperatures (Figure 2.3a). The WRF Control Run produces a strong summertime warm bias at 11 of the 17 locations (Figure 2.3b). Eight of these 11 stations show the highest overestimate to be in July. The largest bias is at Dewar Lakes with an average July temperature bias of over +5 K.

2.2.1.2. Clouds

Statistically significant correlations with station temperatures (Table 2.2) suggest that WRF does a reasonable job of reproducing the daily average temperature (r values > 0.90) and the timing of the diurnal cycle (r values between 0.40 and 0.69). However, the model tends to highly exaggerate the diurnal cycle and overestimate summertime average temperatures while underestimating the shoulder season average temperatures. Both of these phenomena were also observed by *Wilson et al.* [2011], who ran the Polar WRF at 60 km resolution for January to December of 2007 over the Arctic System Reanalysis domain. In their follow-up study, *Wilson et al.* [2012] suggested that the diurnal cycle issue was a result of a reduced cloud fraction produced by WRF as compared to satellite observations. This is further supported by excessive incoming shortwave (SW) radiation and low longwave (LW) radiation in the model, both a byproduct of a lack of cloud cover.

To assess if we have the same cloud issue in our simulations, we calculated monthly average cloud fraction for the inner WRF domain, using the polar-adjusted algorithm recommended by *Fogt and Bromwich* [2008], and compared to MODIS Aqua observations (Figure 2.4a). The difference between WRF and MODIS clouds (Figure 2.4b) shows that WRF consistently underestimates cloud fraction throughout the 6 month period. Unfortunately, in our case there are no radiation measurements available at the surface within our domain and time period so we cannot further diagnose the WRF with surface observations. We speculate that the lack of cloud cover would cause an excess in SW radiation, particularly in the summer months when the high latitudes receive many sunlight hours. This effect superimposed on a generally cold biased model [*Wilson et al.*, 2011] produces a warm bias in summer months and cold bias in spring and fall months (Figure 2.3a). Subsequently, an exaggeration of peak daytime temperatures would likely cause snow to melt too fast in the model. A lack of clouds in the model would also remove any LW warming effect from cloud presence overnight, and thus, minimum daily temperatures are also exaggerated in WRF. This deficiency in WRF is an unfortunate limitation for its use in the Arctic.

To see if cloud simulations could be improved, we conducted several 1 month sensitivity tests. *Wilson et al.* [2012] suggested potential influential factors on cloud fraction amounts, so we independently varied the microphysics scheme (double moment instead of single moment), longwave and shortwave radiation schemes (RRTMG instead of RRTM), and cloud fraction calculation coefficients (standard instead of polar-adjusted). None of these changes significantly increased cloud cover fraction.

2.2.1.3. Sea Ice and Snow Cover

The time series for sea ice coverage in the inner domain is shown in Figure 2.5. Sea ice extent is the same across WRF experiments (except for the FixedSI cases where it is held constant) since it is prescribed at each input time by the GFS input. However, there is still a difference between the WRF (GFS) sea ice evolution and the IMS observations, although not as large as that for the snow cover. The GFS input for ice observations shows consistently less sea ice coverage than the IMS observations. This could play a part in the warmer temperatures in the WRF Control run, as less ice would cause warmer temperatures to be advected inland.

Figure 2.6a shows time series of percent of the inner domain covered in snow for the WRF Control Run, and the two observational datasets, IMS and MODIS CGF. The maximum value of 40% represents full snow cover on land, as there is also ocean (and sea ice) in the domain. The nonzero minimum snow cover extent represents permanent snow and ice fields in the domain. WRF snow cover begins to melt almost a month prior to the IMS observations, but coincides better with the MODIS CGF snow cover time series.

The Noah LSM handles snow evolution in the WRF model. *Hall et al.* [2010] showed that Noah LSM underestimates the snow water equivalent and snowpack depth, which could cause the date of bare ground exposure to be too early in the WRF model output. We checked the WRF snow depths upon model initialization (1 April 2005) and compared to all available snow depth records and found that initial snow cover was accurately represented at initial conditions; however, this does not rule out the notion that as the model progressed, it did not handle the snowpack depth properly. The Noah LSM,

in general, has been known to melt the spring snowpack too fast as a result of excessive sublimation and early melt start dates [Barlage *et al.*, 2010]. Given WRF's overestimate of daytime high temperatures, it is likely that in addition to the model's tendency to remove snow too fast, the excess temperatures provide even more residual energy toward snow melt.

In addition to problems with the modeled snow cover, IMS observations are well known for keeping snow on the ground too long. According to Brown *et al.* [2007], IMS and its coarser ancestor, the National Oceanic and Atmospheric Administration (NOAA) snow product, exhibited delays in melt of 22–26 days, and attribute them to elevation effects and frequent cloud cover. Wang *et al.* [2005b] discussed the older NOAA snow product and found that it reported snow cover for up to 4 weeks too long in this region. Cloud cover increased dramatically from May–August (Figure 2.4), indicating the strong potential for error in the IMS observations and dampened diurnal temperature cycle in the station records. Despite the poor corroboration of the WRF's snow melt timing by the IMS product, the MODIS CGF result is more encouraging. The timing of melt for the MODIS CGF is much more in line with WRF's. That said, the MODIS CGF is known to employ far too conservative a cloud mask, greatly limiting the automated recognition of surface conditions. Thus, the closer agreement between WRF and MODIS CGF is not necessarily indicative of more realistic modeling on the part of WRF.

To see if 2005 was an anomaly in the IMS snow observation record, we also looked at 2004 and 2006 IMS data. These years show similar melt onset timing (not shown here) and rate of disappearance for 2004 and 2006, suggesting that 2005 was not

an unusually late and sudden snow melt in the IMS records. However, a consistent late-melt bias in the IMS observations cannot be discounted.

We also investigated whether the difference in grid resolution between the IMS observations and WRF grid, and the subsequent snow cover threshold (>50% grid cover = total snow cover) would affect the snow cover results. We tried varying the WRF threshold for snow cover to 20%, 30%, 40%, and 50%, but this produced only minor differences (not shown). Thus, we retained the canonical 50% threshold and concluded that this was likely only a minor factor in the difference between WRF and IMS snow melt timing.

In more than one instance, WRF cannot resolve very narrow and steep fjords, particularly on the east coast of the island, where some stations lay. The discrepancy between modeled and station elevation likely plays another role in explaining discrepancies between observed and modeled temperature and snow cover.

WRF is a state-of-the-art regional climate model, but its issues with clouds, 2m temperature, and snow are an ongoing area of research [*Hines and Bromwich*, 2008; *Hines et al.*, 2011; *Wilson et al.*, 2011, 2012]. Despite the inherent problems with the WRF Control Run, we proceed to assess our snow sensitivity experiments by considering relative changes to the Control Run.

2.2.2. WRF Experiments

2.2.2.1. Radiation vs. Advection

Since we are seeking to evaluate the snow sensitivity in the model, the WRF experiments are evaluated below, predominantly in terms of how effective they are at

retaining snow on the ground during the 6 month simulation. First, though, we look at how the model performance (Bias and Root Mean Square Error (RMSE)) is affected by the WRF experiments by comparing station temperature records to each WRF temperature simulation at that location. 6-hourly temperature bias is strongly a function of model run (which is to be expected with the given experiments), while RMSE is affected more by station location (Figure 2.7a). Using average daily temperatures instead of 6-hourly records (Figure 2.7b), the bias is unchanged, but the RMSE is systematically reduced. Thus, the model does a better job at computing daily average temperature as compared to the diurnal cycle, which tends to exhibit over-exaggerated variability. Figure 2.7c shows the same as Figure 2.7b, but with additional stations that only record daily average temperature. The larger the experimental temperature perturbation, the higher the RMSE becomes. The bias values here are not just a result of the experimental temperature perturbation, but would also include effects from the difference between the closest WRF grid elevation and the actual station elevation. Next, we examine the *effective* temperature change inland as a result of the perturbation experiments. Since the temperature changes in the temperature perturbation cases are only applied to the lateral boundaries of the parent domain every 6 h of model time, the temperature is not expected to propagate in full magnitude toward the center of the inner domain. We examined the effective monthly average temperature change at all grid cells of the inner domain as a result of each experiment for two elevation categories, 0–0.5m (ocean grid cells predominantly) and 0.5–2900m (land). The WRF –1.5 K, –3 K, –4.5 K, and –6 K temperature experiments are not realized in full magnitude at the beginning of the runs, particularly at sea level, as seen in Figures 2.8a and 2.8b. This is important to keep in

mind, as the effective temperature change is less than that imposed on the boundaries, so snow extent may not be as affected as one would expect from a full 1.5 K, 3 K, 4.5 K, or 6 K cooling.

In Figures 2.8a and 2.8b, all experiments show decay toward zero bias in the effective temperature difference from the Control Run with time, although the runs with fixed sea ice deviate from this trend after July, as we discuss later. Figure 2.8b (land) shows a less pronounced decay toward zero than Figure 2.8a (ocean), partly because it is masked by a dip in July for the -4.5 K and -6 K cases, which has to do with the presence of more snow on the ground in these runs and will be explained in more detail later.

In both Figures 2.8a and 2.8b, a robust feature of the FixedSI runs stands out, where temperature differences plummet in September. This feature is particularly strong in the sea level panel results (Figure 2.8a) which makes sense since the sea surface temperatures and sea ice are fixed to 1 April conditions for the whole experiment period, and the surface temperature of sea ice does not have the lower bound that open water has. However, we do see a very strong cooling signal of about 7 K in September at elevations above 0.5m (Figure 2.8b) for the FixedSI run, implying a very strong influence of the sea ice presence on inland temperatures. In the Control Run, September has the minimum sea ice distribution, and the sea surface temperatures are otherwise warm compared to colder temperatures on land. Thus, imposing sea ice stunts an otherwise energy-rich ocean from providing warmth inland. Instead, extremely cold temperatures are simulated by the model. The slight warming during July in the FixedSI run in Figure 2.8b is likely a result of the large overestimates of near-surface temperatures on land by the model. These high temperatures (at Dewar Lakes, the Control Run sometimes reached over 10 K

difference between modeled and observed daily highs in July) outcompete the cooling effects of the expanded sea ice. Figure 2.8b shows a robust cooling in the -6 K case in July. This is likely attributed to the anomalous snow cover (Figure 2.6b), which would reflect incoming solar radiation and further cool the local atmosphere and dedicate more energy to melting snow instead of warming the atmosphere [Williams, 1978b]. To further explore this, we compare the available snow depth observations from in situ stations to snow cover in the WRF -6 K experiment. We find that the station locations that experienced delayed bare ground exposure in the WRF -6 K experiment until at least mid-July (often later) are also the stations that exhibited anomalous cooling by at least 5 K compared to the Control Run. Thus, a feedback is induced where colder temperatures can produce anomalous snow cover, which in turn produce further cooling.

It is of interest to examine whether the sum of the WRF -3 K and FixedSI runs produces the equivalent temperature effect as the run where the two effects are combined simultaneously (WRF -3 K and FixedSI). The insets in Figures 2.8a and 2.8b show the difference between the sum of the -3 K run and the FixedSI run, and the WRF -3 K and FixedSI run in which both perturbations act in concert. All months in the insets show a positive difference which increases as the simulations progress. This shows that the run which combines the two perturbations at once has a greater cooling effect than the sum of the constituent parts run independently and that this effect increases over time. The advection of the perturbed temperatures over sea ice keeps the temperatures cooler than if the surface were open ocean. This effect is amplified in the autumn months when open ocean otherwise provides energy to the atmosphere.

Next, we examine how snow extent is affected by the WRF experiments. It is clear from Figure 2.6b that the experiments affect the rate of melt much more than the date of melt onset. The snow accumulation in the fall season shows that WRF captures the synoptic systems that cause precipitation and that the experiments cause more precipitation in the form of snow than the Control Run. The 95SOLCON case begins to melt very similarly to the -3 K case, but deviates mid-melt season, arriving at a total bare ground situation before the -3 K case. The combined -3 K and FixedSI run is more effective at keeping snow cover on the ground longer during the spring thaw compared to the regular -3 K case; however, by mid-July, it reaches the same minimum level snow cover. The effects of the 95% solar constant on surface radiation are not as strong in the polar regions as at the equator. At summer solstice, for example, such a reduction of the solar constant at the equator would result in a daily average change in insolation of -23.8 W/m^2 , whereas at 67°N , the change would only be -18.9 W/m^2 . This equates to about a 20% difference between the average daily insolation on June 21 at the equator and at 67°N . Thus, the effect of changing the solar constant is not realized as strongly at high latitudes. Perhaps more importantly though, as was mentioned earlier, the boundary conditions feeding WRF are not subjected to a reduction in solar radiation, so the response of the climate is limited. As a result, advection dominates and radiation has very little impact. It is then not surprising that the 95SOLCON experiment does not produce more severe changes, despite the rather severe drop in radiation. Table 2.3 gives the minimum snow cover of the inner domain for each run. The -3 K, -4.5 K, -6 K, and -3 K and FixedSI runs are the cases where the snow does not melt to the same as the Control Run. The -6 K run is the only run that substantially increases (almost 50%

increase in area snow coverage compared to the Control Run) the snow cover extent at summer's end, showing that this advective perturbation is more effective at inducing a snow cover change than the 5% radiation change, at least in our simulations.

2.2.2.2. WRF Temperature Experiments

Since we are ultimately interested in the sensitivity of snow extent to temperature perturbations, particularly when the minimum snow cover is reached in each run, we examine the relative changes of snow cover extent as a function of WRF temperature experiments (WRF -1.5 K, -3 K, -4.5 K, and -6 K). Figure 2.9 illustrates that on the minimum snow extent day, the WRF -6 K case keeps snow cover north of 66°N , west from the north central Baffin Island plateau region, and into the Northwest peninsula of the island. Melville Peninsula, to the west of Baffin Island, also retains a good amount of snow cover. This agrees quite well with the LIA snow line regions demarked by *Williams* [1978a] from sparse lichen-covered areas, who noted that the LIA snow extended more in the North than the South, and from the north central plateaus, there was a distinct lowering to the west. Thus, despite problems with the 2 m temperature and the Noah LSM, WRF can realistically simulate where snow cover is most likely to expand, in effect characterizing the regional snow sensitivity.

Figure 2.10 shows snow cover percent as a function of 50 m elevation bands for each cooling experiment and the Control Run on the minimum snow extent day, excluding Greenland and all latitudes below 66°N . There is almost no change between the Control Run and the -1.5 K and -3 K minimum snow extent for any elevation range. The -4.5 K and -6 K cases, however, show different departures from the Control, -1.5 K

and -3 K runs. The Control Run shows that full snow coverage exists above about 1200 m elevation, agreeing with current field estimates, but that patchy snow exists below that. Defining the equilibrium line altitude from this plot becomes problematic, since there is not a clear step change from no snow to full snow cover, but rather a gentler transition from bare ground to full snow cover. Indeed, the slope is steeper for the Control, -1.5 K and -3 K runs, than the colder runs, suggesting that the snow cover is not just a function of elevation but of other considerations such as terrain aspect and local temperature.

For a given snow cover percent threshold, it is possible to extract snow line elevation and determine its sensitivity to temperature. We show the minimum snow line elevation is shown as a function of the average 6 month temperature difference between the Control Run and the given cooling experiment (Figure 2.11). There are no changes between the Control Run, -1.5 K run and the -3 K run, for reasons outlined in sections above, so if we take the slope of the coldest three points, we find the sensitivity of the snow line for the given threshold. The corresponding sensitivities are listed beside the curves in Figure 2.11. The choice of threshold affects the sensitivity result, and the elevation range of interest. The 50% cover threshold shows the largest change between WRF runs in snow cover. On average, it produces a sensitivity of about 7 K/km, and is relevant to elevations in the range of 300–700 m elevation, coinciding with the elevation range of Baffin Island's north central plateau. This value is also the upper end of the free-air moist adiabatic lapse rate, the value often used to extrapolate from station temperatures in this region [Gardner *et al.*, 2009]. The minimum snow line elevation change between the Control Run and the -6 K run given the 50% snow cover threshold is 350 m, the upper end of what was observed by Miller *et al.* [2012].

Even though an average temperature decrease of roughly 2 K did not impact the snow cover, it is not clear how much of this cooling was necessary to produce the observed snow changes. We can only conclude, then, that the magnitude of average temperature change that caused the modeled snow cover change in the WRF -6 K case is as much as -4.9 K or as little as -2.8 K, or otherwise -3.9 ± 1.1 K. Thus, given the 50% snow cover threshold, with an average temperature decrease of -3.9 ± 1.1 K, WRF is capable of producing an abrupt snow line elevation change within only one summer season which is comparable in magnitude to that observed during the LIA.

2.3 Discussion

Our major findings can be summarized as follows. The WRF Control Run shows significant correlations with observed temperature records at all stations. Part of this strong agreement is related to the forcing of WRF with a global model that assimilates observations and to the spectral nudging of the u and v wind fields above the boundary layer. The diurnal cycle is often highly exaggerated, with differences in peak daily temperatures up to 10 K, but daily average temperatures are better predicted than the diurnal temperature cycle. The lack of cloud cover predicted by the model is a likely reason for these problems, an issue that has been observed in other WRF studies in the Arctic [Wilson *et al.*, 2012]. At more than half of the stations, the WRF Control Run tends to overestimate summer temperatures and underestimate spring and fall temperatures. The WRF Control Run begins to lose snow cover about a month earlier than the IMS data suggest, but matches very well with the timing of MODIS CGF snow cover product. This discrepancy with IMS could be a result of errors in observations

(e.g., cloud cover obstruction during IMS data collection) or a tendency for the Noah LSM to sublimate or melt snow more readily than in the real world [Wang *et al.*, 2005a; Brown *et al.*, 2007; Barlage *et al.*, 2010].

Despite issues with the WRF Control Run, relative changes between the Control Run and the experiments provide insights into the sensitivity of this particular environment to sudden changes in temperature, sea ice expansion, and solar radiation. The 95SOLCON, FixedSI, and -3 K and FixedSI runs were unable to cool the domain enough to retain more snow than the Control Run. However, the FixedSI run did exhibit a robust average near-surface cooling of about 7 K over land in September, suggesting that a sudden expansion of sea ice has quite significant effects inland in seasons when the ocean is otherwise heating the atmosphere. This hints at the strong potential for expanded sea ice to affect inland temperature and snow cover beyond the simulation's end date of 30 September. The run which applied the -3 K and FixedSI perturbations simultaneously (-3 K and FixedSI) showed a greater cooling effect on inland temperatures than the addition of the two independent constituent runs (WRF -3 K) + (FixedSI), and this effect was amplified over the course of the 6month simulation. Greater sea ice coverage would be expected in colder years so one would expect them to interact, which, as this experiment suggests, would lead to cooling greater than the sum of the parts. The temperature sensitivity experiments (WRF -1.5 K, -3 K, -4.5 K, and -6 K), applied at the boundaries of the outer domain, did not propagate to the inner domain in their full magnitude, and this effect became more evident in the later months of the runs. The WRF experiments influenced the rate of melt, but the date of melt onset

was relatively unchanged between runs. The only runs successful in substantially suppressing the snow line were WRF -4.5 K and WRF -6 K. The WRF -6 K run showed increased snow cover north of 66°N , moving west into the north central plateau and NW peninsulas of Baffin Island, and into Melville Peninsula in Nunavut. These regions coincide with the LIA snow line outlined by *Williams* [1978a], suggesting that the WRF does a realistic job of highlighting regional sensitivity to snow line change. The amount of actual cooling necessary to expand the area of snow cover by 50% from the Control Run to the -6 K run is -3.9 ± 1.1 K.

Using 50 m elevation bands, snow cover varies continuously from bare ground to full snow cover. Thus, there is not one obvious choice which defines the snow line, and the snow line's sensitivity to temperature change depends on this choice. We find that the sensitivity of snow line to temperature is greatest, 7 K/km, when the snow line is defined as 50% snow cover. Given this definition, the minimum snow line elevation difference between the Control Run and the -6 K run is 350 m. Such a change in elevation is on the upper end of what was observed by *Miller et al.* [2012]. Thus, the WRF model can lower the snowline by comparable elevation changes seen during the descent into the LIA, in only one season, with an average temperature decrease from current temperatures by -3.9 ± 1.1 K. Given the WRF's sensitivity of 7 K/km, and *Miller et al.*'s [2012] data which show two events where the snow line elevation changed by 240 m and 340 m, a temperature decrease of 1.7 and 2.4 K would be necessary to cause such a change.

2.4. Conclusions

In the scenario suggested by *Miller et al.* [2012], successive volcanic eruptions suppressed summer temperatures enough to cause expanded snow cover and sea ice. In our high-resolution WRF simulations, we examined the effect that a sudden suppression of temperatures, reduction of incoming solar radiation, and expansion of sea ice might have on snow cover after only one summer season on Baffin Island. Despite WRF's inherent issues with cloud cover, diurnal temperature variations, and snow cover, the simulations still produced reasonable estimates of snow line sensitivity. In particular, the WRF model showed excellent correspondence between where snow expansion was observed in the -6 K case, and where *Williams* [1978a] demarked the LIA snow line. We found that the region responding with most sensitivity to a summer temperature reduction of -3.9 ± 1.1 K from the Control Run was the northern Baffin Island plateau between 400 and 700 m elevation, where snowline lowered by 350 m, similar to the reconstructed snowline of *Williams* [1978a].

Applying the maximum snow line sensitivity we observed in the WRF model (7 K/km) to the *Miller et al.* [2012] data, which show snow line lowering by 240–340 m, we find that a temperature decrease from current conditions of 1.7–2.4 K would be necessary to reproduce what they observed. By comparison, applying the mean ablation season lapse rate of 4.9 K/km derived from ice sheets in the Canadian Arctic [*Gardner et al.*, 2009] suggests that even less of a temperature decrease, 1.2–1.7 K, could be necessary to produce the observed snow line descent. Our WRF results also showed that expanded sea ice has the strong potential to reduce inland temperatures.

Proxy records from Devon and Agassiz Ice Caps near Baffin Island show summer temperature anomalies from 1400 to 1700 CE that were about 6 K cooler than the 1860–

1959 mean [Bradley and Jones, 1993]. Arctic averaged decadal summer temperature anomaly estimates based on a composite of proxy records shows about 1.5 K difference between the LIA and current values [Kaufman *et al.*, 2009]. Thus, if Baffin regional temperatures during the LIA were roughly 2 K lower than present (which is reasonable, given the proxy records), and there was a more extensive sea ice cover; this together would have been enough to perpetuate an ice sheet on Baffin Island throughout the LIA.

It is important and useful to highlight the gaps in performance in the high-resolution modeling and observations in high latitude applications, particularly for those interested in evaluating snow cover. The WRF's poor simulations of diurnal temperatures, particularly at the inland sites, the lack of cloud cover produced in an otherwise overcast region, and the land surface model's tendency to melt snow too fast leave the model results wanting. On the other hand, satellite observations of snow cover in the high latitudes are flawed as well, given the high frequency of cloud cover in the summer season. The combination of error-prone observations and model output tend to bring one to an enigmatic crossroad. However, in an application such as this, we have shown that looking at relative changes can yield valuable information about how the model works, and what that might mean in the real world.

CHAPTER 3: ARCTIC CRYOSPHERE RESPONSE TO VOLCANIC ERUPTIONS IN THE LAST MILLENNIUM PMIP3 SIMULATIONS

In this Chapter, we investigate how the models from the Paleoclimate Modeling Intercomparison Project Phase 3 (PMIP3) last millennium (LM) simulations compare to paleoclimate reconstructions in the Arctic and NH. We assess whether any of the models produce the reconstructed and previously modeled sustained centennial-scale cold anomalies and expanded sea ice and snow cover in the North Atlantic and Baffin Island regions following multiple, successive large volcanic eruptions. The work presented in Chapter 3 [Berdahl and Robock, 2013b] is published in the *Journal of Geophysical Research – Atmospheres*².

3.1 Methods

Seven modeling groups participated in the LM intercomparison project (Table 3.1). Each group participating ran their coupled atmosphere-ocean model from 850 to 1850 C.E., except Flexible Global Ocean-Atmosphere-Land System (FGOALS), which ran from 1000 to 1999 C.E. The models were forced with volcanic aerosol reconstructions from either *Gao et al.* [2008] or *Crowley et al.* [2008], as outlined in Table 3.1. Both reconstructions are based on ice core sulfate records from both polar regions and differ in the transfer function from the ice core sulfate to aerosol optical depth (AOD) and in the filtering of globally important eruptions [Schmidt et al., 2011]. There are two Goddard Institute for Space Studies (GISS) simulations, which differ predominantly in their choice of volcanic forcing data set, hereafter referred to as GISSG,

² Berdahl, M., and A. Robock (2013), Northern Hemispheric cryosphere response to volcanic eruptions in the Paleoclimate Modeling Intercomparison Project 3 last millennium simulations, *J. Geophys. Res. Atmos.*, 118, doi:10.1002/2013JD019914.

which used the *Gao et al.* [2008] reconstruction and GISSC, which used the *Crowley et al.* [2008] reconstruction. Table 3.1 also notes the solar forcing used in each simulation. *Schmidt et al.* [2011] described the full details of climate forcing reconstruction options for the PMIP3 LM simulations.

Some models did not have snow or ice concentrations available for download. Therefore, we are able to analyze nine unique models for temperature, of which one was GISS which had been run with two different volcanic forcing reconstructions (GISSC and GISSG), seven models for sea ice, and five models for snow.

Due to computational constraints, some of the models were not able to properly spin-up and reach quasi equilibrium. The Model for Interdisciplinary Research on Climate (MIROC) and GISS models show a drift in climate, the former over the entire millennium and the latter over the first 500 years. We address this in the GISS models by removing the linear-fitted trend of the first 500 years of the control run from the forced simulations (GISSG and GISSC) [*Brohan et al.*, 2012] and then adding the climatology of the rest of the control run (the last 500 years) back so we have absolute temperature instead of anomaly. However, for MIROC, since the entire millennial record is drifting, we cannot return to absolute temperature since we do not know the true climate. Thus, we leave MIROC uncorrected. The sea ice and snow in the GISS simulations are corrected in a similar fashion, as is seen, for example, in Figure 3.5.

Typically, PMIP3 climate model results are compared to proxy records as temperature anomalies, as opposed to absolute temperatures [*Brohan et al.*, 2012; *Landrum et al.*, 2013]. While this method may be appropriate to evaluate variability as relative responses to external forcing, in regions such as the Arctic where temperatures

are near the freezing point (and phase changes occur), it is important to report actual temperatures to evaluate the fundamental processes and states of the climate change. Thus, when reporting temperatures in this article, we focus on absolute temperatures intentionally.

We compute area-weighted average temperatures for the Arctic region (north of 66°N), the NA region, and Baffin Island region, shown in Figure 3.1. Unless otherwise noted (e.g., using land only in these regions or Arctic defined as north of 60°N instead of 66°N), these are the regions referred to in the rest of this article. In some cases we apply a third-order low-pass Butterworth filter as in *Otterå et al.* [2010] so that we retain only multidecadal and slower variability for comparison to proxy reconstructions. To make the model results comparable to sea ice reconstructions, sea ice extent in Figures 3.4 and 3.5 is calculated as the areal sum of cells with ice concentration greater than 15%. If the grid cell has a sea ice concentration $\geq 15\%$, we consider it to be fully ice covered; otherwise, it is considered ice free, in line with the National Snow and Ice Data Center (NSIDC) sea ice extent definition.

Finally, we perform a superposed epoch analysis (SEA) for our analysis of response to volcanic eruptions. We convert the *Gao et al.* [2008] NH sulfate aerosol loading to aerosol optical depth (AOD) with the conversion factor they recommend of 1.5×10^{14} g. We take the linear average of the *Crowley et al.* [2008] AOD data for the 0°N–30°N and 30°N–90°N latitude bands to generate a NH data set for comparison to *Gao et al.* [2009]. We then find the top 10 volcanic eruptions based on AOD in the NH for both data sets (Table 3.2). We superpose each eruption event and take the average of their response in temperature, sea ice area, and snow cover area to each major eruption for the

25 years following each event. Each parameter in the SEA analysis is reported as an anomaly with respect to the 5 year average prior to the eruption. Sea ice in the SEA analysis is computed as an area as opposed to extent as in the other calculations in this article. That is, no threshold of 15% is set; instead, we compute the areal sum of the product of grid cell area with ice concentration.

3.2 Results

3.2.1 Hemispheric, Arctic and Regional Temperatures

Figure 3.2 shows the average June-July-August (JJA) temperature series for the available PMIP3 LM simulations for the Northern Hemisphere, Arctic (north of 66°N), and Baffin Island (land only) region (270°E–300°E, 60°N–75°N). Since we are interested in decadal-scale variability, we used a third-order low-pass Butterworth filter with a cutoff frequency of 15 years [Otterå *et al.*, 2010] to filter the temperature records. The lowest panel shows the *Gao et al.* [2008] NH stratospheric loading of sulfates from volcanic eruptions as an indicator of timing and magnitude of eruptions during the period. A prominent feature of all three temperature panels is the clear difference in mean states for each model, ranging 1.3 K, 2.8 K, and 5.3 K in the NH, Arctic, and Baffin Island, respectively. The order of warmest to coldest model differs depending on the region of interest. Over Baffin Island, the average summer temperatures all tend to be above freezing and those that dip below freezing in post-eruption years are CCSM4 and GISSG.

Next, we compare the PMIP3 model results to paleoclimate records in Figure 3.3. Since the temperature reconstructions are calibrated to instrumental records, there is no

large uncertainty in their absolute calibration. All models except MIROC underestimate Arctic-wide JJA near-surface land temperatures. There is better representation by the models of NH annual temperatures, except for the Institut Pierre- Simon Laplace (IPSL) model which underestimates it by several degrees. The GISS models are particularly strong at representing the mean NH climate. These features are also seen in the zonal mean temperatures (not shown) for the NH mean annual and mean JJA temperatures for the full millennium.

The reconstructed temperature response to the eruptions is generally muted compared to almost all of the modeled responses (Figure 3.3). *Timmreck et al.* [2009] show that the temperature response of the 1257 eruption (and presumably all eruptions) is sensitive to the aerosol particle sizes prescribed in the simulation. They estimate the range of maximum summer NH cooling after the 1257 eruption to be from 0.6 K to 2 K. They show that only aerosol particle sizes substantially larger than observed after Pinatubo yield temperature responses consistent with reconstructions. The *Gao et al.* [2008] reconstruction contains no information about particle size distribution, and the *Crowley et al.* [2008] data set includes uncertain estimates of particle size, so using the wrong size distribution may be the reason that the temperature response in the models to the 1257 eruption, and others, is overestimated. The magnitude of response in the Arctic and the NH after the 1257 eruption (Figure 3.3) is comparable between the GISSG than the GISSC simulations, although this is not the case for other major eruptions throughout the simulations. Further error sources, such as location of the volcano and season of eruption, complicate matters even more [*Anchukaitis et al.*, 2012; *Toohey et al.*, 2011]. In their assessment of the CCSM4 LM simulation, *Landrum et al.* [2013] found the

response of the model to large eruptions to be 2–3 times larger than the NH anomalies estimated from tree rings. The twentieth century response to volcanic eruptions is also noted to be too strong [Meehl *et al.*, 2012]. Indeed, errors in the paleoclimate reconstructions are very possible as well. Mann *et al.* [2012] suggested that NH volcanic responses were being underestimated by tree ring-based reconstructions, although there has been opposition to this suggestion [Anchukaitis *et al.*, 2012].

Lastly, we assess whether or not the models are able to reproduce a sustained Arctic LIA cooling. Proxy records suggest that NH temperatures decreased by roughly 0.5 K [Mann *et al.*, 2009] and that at least a regional summer temperature lowering of 2 or 3 K occurred in the North Atlantic sector of the Arctic [Miller *et al.*, 2012]. We test whether the models produce an Arctic and Baffin Island cooling with LIA period definition of 1450–1850 and 1600–1850. We compare this to the periods 850–1450 and 850–1600, respectively. We find that all models (except MIROC with the LIA defined as 1450–1850) produce statistically significant colder summer Arctic average temperatures (based on a Student's *t* test), no matter which period is defined as the LIA. The maximum cooling is 0.3 K in the CCSM4 model. All other models produce less than 0.2 K change. We do the same analysis for Baffin Island summer land temperatures and find that four models produce statistically significant colder temperatures in the LIA than in the period before. The maximum cooling achieved is again by the CCSM4 model, of 0.5 K. Thus, the LIA is generated in most models, but its magnitude is very weak compared to what proxy records suggest.

3.3 Sea Ice

Despite the issues with model resolution and snow cover representation on Baffin Island, another measure of multidecadal model response to repeated volcanic forcing is in the sea ice. *Miller et al.* [2012] cite an ocean/sea ice feedback mechanism by which a centennial-scale expansion of snow cover and sea ice is maintained. Here, we assess whether any of the PMIP3 models show a sustained sea ice expansion in the North Atlantic region.

First, we compare the PMIP3 NH sea ice extent to the *Kinnard et al.* [2011] Arctic August sea ice extent reconstruction, which is based on 69 proxies predominantly derived from ice cores, but also from tree rings, lake sediments, and historical observations of sea ice. The reconstruction was calibrated against an historical index of late-summer extents (at least 15% concentration) from 1870–1995. All PMIP3 model ice extents are calculated with a 15% concentration threshold as well, consistent with the paleoclimate reconstruction and NSIDC methodology, where any grid cell with $\geq 15\%$ ice concentration is considered fully covered; otherwise, it is considered ice free. Aside from CCSM4 and the Beijing Climate Center (BCC) model, which largely fall within the reconstruction uncertainty range, the models tend to underestimate the sea ice extent for the duration of the last millennium (Figure 3.4). The correlation of the models with reconstruction is usually significant (p values of < 0.05 using Student's t test), but in seven of the eight runs, it is negative. MIROC shows the least sea ice area, although it is the only model to positively correlate with the reconstruction. We did not find any consistent lags between individual models or between models and reconstructions.

The CCSM4 simulation shows a period of generally higher sea ice extent between about 1250 and 1500 C.E., suggesting that this model has a multidecadal sea ice response

after the 1257 eruption. Figure 3.5 shows the minimum annual sea ice extent in the NA region for each model. The 40 year low-pass filtered time series exceeds the standard deviation of the low volcanic activity reference period (850–1150 C.E.) only in the GISSG, GISSC, and CCSM4 models. The significant ($>1 \sigma$) expansion of sea ice in these models lasts up to a few decades in GISSG and GISSC, and up to 80 years in CCSM4, but never reaches a continuous centennial long expansion. Analysis of SSTs (not shown) in a subset of the North Atlantic (50°W – 20°W and 50°N – 65°N , per *Zhong et al.* [2010]) shows that none of the models produce a cumulative cooling after the 1257 Samalas and the subsequent closely spaced eruptions. This was a key step in the mechanism for sustaining sea ice in the volcanically perturbed thirteenth century [*Miller et al.*, 2012; *Zhong et al.*, 2010]. As a result, we infer that the rate of basal sea ice melt in the Arctic Ocean was not reduced, and thus, sea ice did not remain in an expanded state for more than 100 years.

3.4 Model Elevation

We suspect that model resolution plays a factor in properly representing the mean climate over Baffin Island, whose highest peak in reality, Mount Odin, reaches over 2 km above sea level. Figure 3.6a shows the model representation and actual Baffin Island topography, along with the number of grid cells (n) comprising the Baffin Island region. Actual elevations are derived from the U.S. Geological Survey GTOPO30 product, available from <http://earthexplorer.usgs.gov/>. This digital elevation model has a resolution of 30 arcseconds, which roughly equates to 1×1 km grids at the equator that get smaller toward the poles. The representation of elevations above 400 m is deficient in

most models compared to the GTOPO30 data (Figure 3.6a). None of the models represents elevations above 750 m, while in reality, more than 500 km² of the region resides at higher elevations. The lack of representation of these high elevations in the models would not only have impacts on snow and ice, but also on atmospheric circulation. We examine the relationship between maximum model elevation and mean summer (JJA) surface temperature in Figure 3.6b. Models with higher peak elevations on Baffin Island tend to have colder mean summer climates. The two models with the coldest climate in the Baffin Island region, CCSM4, and GISS, also represent the high plateaus (400–700m) [Andrews *et al.*, 1972], elevations critical in fostering and sustaining large snow area change [Berdahl and Robock, 2013a].

3.5 Model Response to Volcanic Eruptions in the Last Millennium

The results of our SEA analysis for temperature, sea ice, and snow cover with the top 10 eruptions in the last millennium are described below.

3.5.1 Temperature

We analyze the response of the mean NH JJA and annual temperatures as well as those over Baffin Island land only (Figure 3.7). In all cases, the GISSG model shows the strongest average peak response exceeding 1 K NH annual average cooling and becomes even greater in the summer months reaching roughly 1.5 K. All models show a post-eruption cooling, MIROC being the most muted in the NH.

The temperature response on Baffin Island is again strongest in the GISSG simulation, in both annual and summer averages. Summertime average responses mainly govern the minimum snow cover extent on the island. Baffin Island summer temperatures cool by over 2 K in the GISSG model, followed by GISSC and CCSM4. The MIROC and BCC models show mild and slightly delayed post-eruption temperature decreases compared to that of the GISS and CCSM4 models. The GISSG model shows the slowest recovery in the first 5 post-eruption years, although the Max Planck Institute (MPI) model shows similar cooling in the decades following the eruption even though it does not reach such extreme cooling in year 1.

The integrated temperature response per unit forcing from year 0 to year 10 is shown in Table 3.3 for NH and Baffin Island annual and JJA average responses for the top 10 eruptions. The models with the largest integrated NH annual and JJA temperature response are MPI, Hadley Coupled Model (HadCM3), and the GISS model. On Baffin Island, the integrated annual temperature response is strongest in MPI and the GISS models, whereas in the summer, the GISS, IPSL, and CCSM4 show the strongest net cooling in the 10 years following the eruptions. Thus, the model temperature responses do not rank consistently from region to region or season to season, and their impact on the cryosphere is not only dependent on the temperature anomalies but also on the mean state of the background climate.

3.5.2 Sea Ice

The SEA analysis for September sea ice area in the NH and the NA regions (Figure 3.8) follows that of temperature. In the NH, GISSG shows a significantly larger response than any of the other models, more than twice the area anomaly than any other

model. All models subside to pre-eruption conditions by 10 years after the eruption. In the NA, GISSG shows the largest peak in sea ice area anomaly after the eruptions, although it is followed closely by CCSM4, GISSC, and BCC. Again, the anomalies subside within roughly a 10 year lag of the eruption.

Integrated sea ice area expansion per unit forcing for 10 years following the eruptions is shown for the NH and NA in Table 3. In the NH, sea ice expansion is largest per unit forcing in the GISS models and HadCM3. In the North Atlantic, the GISS models and CCSM4 produce the greatest integrated sea ice expansion in the 10 years following the eruptions. Again, over Baffin Island, the coldest models are CCSM4 and GISS, so it follows that they would produce the most sea ice in this region.

3.5.3 Snow

The SEA analysis for snow is shown for the Baffin region and the NH, expressed as a percentage of land covered in snow at the annual minimum of monthly mean extent (typically August) and as a snow area anomaly with respect to the mean of 5 years prior to the eruptions (Figure 3.9). The minimum annual percent of snow cover on land in the NH varies across the models with CCSM4 differing from MIROC NH snow cover by 3% (more than 150% change). In other words, the mean minimum annual snow extent in the MIROC model covers about $3.0 \times 10^6 \text{ km}^2$ less in area than that of the CCSM4 model. As discussed earlier, this is probably in part a function of model resolution since higher-resolution models can capture higher elevations that are colder and sustain snow cover. The post-eruption snow extent anomaly in the NH is strongest and very similar in the GISSG and the CCSM4 models. This response tapers off within a decade in

all models, earlier in most.

On Baffin Island, the story is similar. The MIROC model shows minimal snow retention at the peak of summer on the island and no significant post-eruption anomaly even after the eruptions in this region. The BCC and MPI models produce a similar result, although their minimum snow extent tends to be higher. The CCSM4, GISSG, and GISSC models show significant responses to the eruptions on Baffin Island, both in terms of percentage and area anomaly. The CCSM4 and GISSG models show the same maximum area anomaly over Baffin Island, roughly twice the magnitude of that seen in GISSC. Similar to the NH, the post-eruption snow expansion is short-lived, decaying back to pre-eruption snow extents within 10 years.

Table 3 shows the NH and Baffin Island snow area anomalies following the top 10 eruptions integrated over lag years 0 to 10. In both cases, the snow expansion is largest in the GISS and CCSM4 models. Over Baffin Island, the largest integrated response is generated by the CCSM4 and the GISSG model. Again, these are the coldest models in this particular region, although these models rank only third and fourth in their summer temperature response to the eruptions over Baffin Island. This emphasizes that both the background summer climate and the strength of the response to volcanic eruptions simulated by the models dictate the behavior of the cryosphere. This is in agreement with the general conclusions of *Zanchettin et al.* [2013].

3.5.4 Model Sensitivity

Next, we assess the SEA temperature and snow responses together, by plotting the temperature and snow SEA time series against each other (Figure 3.10a). We truncate

the time series to include only lag year 1 to lag year 10 since we are interested in post-eruption response. From this we can fit least-squares regression fits to each model and find the sensitivity of the snow response to temperature change for each model (units of km^2/K). Plotting these sensitivities against the mean JJA climate in each model over Baffin Island, we show that the models' ability to produce a snow response is strongly a function of the mean climate (Figure 3.10b). There is a sudden transition between models exhibiting a widespread change in snow cover and those with virtually no change in snow. Above about 2.5°C mean summer climate, the models become incapable of reaching the freezing point and forming snow, let alone sustaining extra amounts of snow on Baffin Island. Below roughly 2.5°C , the models show widespread snow expansion. The temperature response after the eruption is also a function of the volcanic reconstruction used, which is evident in the GISS models, whose primary difference is the choice of volcanic forcing reconstruction. This result highlights the necessity for models to not just correctly reproduce eruption response as anomalies, but equally important, they must be able to capture the absolute temperature. This has particularly critical consequences around the freezing mark, as the presence of snow and ice triggers the ice-albedo feedback, one of the most important climate feedbacks on the globe.

3.6 Discussion

We can summarize our main findings as follows. Comparison of NH, Arctic, and Baffin Island temperature in the PMIP3 models shows a large spread in mean model background climate, the rank of which is not consistent across regions. Annual average NH mean climates span 3 K, Arctic average summer temperatures span 3 K, and Arctic

land-only summer climates range by more than 6 K. Over Baffin Island, summer temperatures dip below 0°C after major eruptions only in the GISSG, GISSC, and CCSM4 simulations, allowing snow to expand on the island only in these models despite other models having a greater integrated temperature response per unit forcing. Mean summer climate of Baffin Island is partly a function of the model resolution and grid cell elevations. Most models produce a Little Ice Age; however, the magnitude of associated cooling is much less than expected from reconstructions. The largest change noted was about 0.5 K cooling on Baffin Island, compared to the proxy data which suggests that at least several degrees of cooling occurred [Miller *et al.*, 2012]. The temperature response to volcanic eruptions is generally stronger in the PMIP3 models than in reconstructions, consistent with other studies [Landrum *et al.*, 2013; Brohan *et al.*, 2012; Meehl *et al.*, 2012]. This could be a result of, for example, inadequate aerosol representation [Timmreck *et al.*, 2010], model difficulty in capturing dynamic responses in the stratosphere [Shindell *et al.*, 2003], uncertainties in eruption location and time of year [Anchukaitis *et al.*, 2012; Toohey *et al.*, 2011], and potential errors in ice core interpretation when generating volcanic reconstructions [Schneider *et al.*, 2009]. Problems with the paleoclimate reconstructions are of course possible as well. It has been suggested that there is an underestimation of volcanic cooling in tree ring-based reconstructions of Northern Hemisphere temperature [Mann *et al.*, 2012], although this has been vehemently rebutted by others [Anchukaitis *et al.*, 2012].

Sea ice extent tends to be underestimated in most of the models compared to the Kinnard *et al.* [2011] reconstruction. CCSM4 and BCC do well in their sea ice extent representation, falling within the range of uncertainty of the reconstruction. Compared to

the period 850–1150 C.E. which is characterized by low volcanic activity, 40 year low-pass filtered sea ice area in the NA shows decadal-scale expansion occasionally after the mid-thirteenth century in the GISSG, GISSC, and CCSM4 models, but does not show centennial-scale expansion in the LM simulations. The key event in the *Miller et al.* [2012] modeling was volcanic activity in the late thirteenth century. At that time, eruptions were closely spaced enough that the North Atlantic surface waters never recovered to their pre-eruption temperature between eruptions, so that there was a cumulative temperature lowering larger than for any single volcanic event. Our analysis of SSTs in the PMIP3 models (not shown) in a subdomain of the North Atlantic (50°W–20°W and 50°N–65°N, per *Zhong et al.* [2010]) do not produce a sustained cooling beyond about a decade after the 1257 Samalas eruption. The relatively warm SST conditions in the PMIP3 simulations likely contribute to limiting the sea ice expansion during the thirteenth century.

The SEA analysis reveals the temperature response to strong volcanic eruptions (SVEs) in the NH is strongest in the GISSG model, with more than 1 K maximum annual average cooling and up to 1.5 K maximum summer average cooling. MIROC and BCC show less than 0.5 K maximum cooling for both annual and summer cooling. Cooling is much stronger over Baffin Island land, particularly in the summer, when GISSG exceeds 2 K cooling, and greater than 1 K cooling is produced in all other models except BCC and MIROC. Minimum annual sea ice area expands most in GISSG, and this behavior is especially outstanding from the other models in the NH compared to the NA. On average, CCSM4 produces the most expansive minimum annual NH snow cover, followed by the BCC, GISS, MPI, and MIROC models. The only models that show a

response in the SEA snow analysis in the NH and over Baffin Island are GISSG, CCSM4, and GISSC models. Over Baffin Island, the largest integrated response in snow area from year lag 0 to 10 is in CCSM4 and GISSG. Again, these are the coldest models in this region, although these models rank only third and fourth in their integrated summer temperature response to the eruptions over Baffin Island. Thus, a combination of appropriate background climate and response to volcanic eruptions is necessary to generate a response in the cryosphere, in agreement with the findings in *Zanchettin et al.* [2013]. From the SEA snow and temperature analyses over Baffin Island, we find that the only models that manifest a snow expansion in response to a temperature drop after SVEs are the models whose mean summer climates are near enough to 0°C, such that a perturbation brings temperatures below freezing. There is a sharp transition between the degree of snow expansion in models with a mean climate below and above about 2.5°C. *Zhong et al.* [2010] and *Miller et al.* [2012] used CCSM3, CCSM4's predecessor, to produce a centennial-scale climate change from decadal paced SVEs. Here we show that the coldest model in the Baffin Island region is CCSM4, so it is likely that CCSM3 also produces near-zero temperatures in this region. It is possible, then, that they may not have found significant and sustained sea ice and snow expansion if they had used a climate model which happened to model a warmer mean state in this region. Ultimately, we show that it is critical to accurately model the absolute temperature in regions near the freezing point where snow and ice form and melt. Crossing this threshold could potentially induce feedback that support further sea ice expansion, colder SSTs, and consequently colder and snowier conditions on land.

3.7 Conclusions

We assessed the PMIP3 LM simulations in terms of absolute temperatures and the temperature, snow, and ice response to volcanic eruptions with a focus on the North Atlantic and eastern Canadian Arctic regions in order to determine if current state-of-the-art models produce sudden and persistent cold conditions after SVEs. We have shown that the PMIP3 models are generally colder than reconstructions over Arctic land but at the same time have too little sea ice in the Arctic compared to reconstructions. Most models produce significantly cooler temperatures in the Arctic and in the North Atlantic region during the LIA; however, the magnitude of cooling is much less than expected from proxy records. Only two of the models produce decadal sea ice expansion, but none produce centennial-scale expansion. Snow cover over Baffin Island shows large-scale expansion in only two of the five available models, although it is not sustained beyond a decade. The PMIP3 models' lack of sustained cooling response could be due to their inability to capture changes in ocean circulation, which other studies have shown can lead to centennial-scale cooling in the North Atlantic.

Spread in the models' mean climate states in the NH, Arctic, and over Baffin Island is evident. Model resolution, and consequently topography, plays a strong role in determining mean climate over Baffin Island. Critical plateau elevations of 400–700 m, necessary for fostering and sustaining large snow area change [*Berdahl and Robock, 2013a*], are only represented in the CCSM4 and GISS models. In more than half of the models, warm summer climates over Baffin Island stunt snow expansion after volcanic eruptions completely. Thus, it is crucial to properly represent absolute temperatures particularly in areas such as the Arctic where small temperature changes dictate phase

changes of water. This is especially important, since snow and ice presence can further induce feedback, such as ice albedo, which may influence global climate but cannot be triggered from volcanic forcing in models that are too warm.

CHAPTER 4: ARCTIC CRYOSPHERE RESPONSE TO GEOENGINEERING

In this Chapter, we ask how much the Arctic would cool in the G3 and G4 scenarios, and whether geoengineering in a high CO₂ world would prevent the demise of multi-year sea ice. We also examine the effects of geoengineering on the already decreasing Arctic spring snow cover on land. Furthermore, we examine the post-geoengineering period (after 2070) to see how the Arctic cryosphere rebounds after the cessation of aerosol injection, deemed the “Termination Effect” [e.g., Wigley, 2006; Jones *et al.*, 2013]. Section 4.1 describes the methods and datasets used, Section 4.2 describes our results, Section 4.3 presents a summary and Section 4.4 some discussion and conclusions. The work presented in Chapter 4 has been accepted to *Journal of Geophysical Research – Atmospheres* as part of the GeoMIP Special Edition³.

4.1 Methods

Modeling groups that participated in each experiment (G3 and G4) and that are reported in this paper are summarized in Table 4.1. The MIROC-ESM and MIROC-ESM-CHEM models are treated separately since they branch from unique control runs and include different processes. MIROC-ESM-CHEM includes an online chemistry module that predicts atmospheric ozone and other major chemical species. The GISS-E2-R and HadGEM2-ES modeling groups ran three ensemble members, and all results

³ Berdahl, M. et al. (2014), Arctic cryosphere response in the Geoengineering Model Intercomparison Project (GeoMIP) G3 and G4 scenarios, *J. Geophys. Res. Atmos.*, accepted.

reported here show their ensemble mean. The other models generated one ensemble member.

The observational data we use for comparison to global and Arctic near surface temperatures are the 2 m gridded temperatures from the latest ECMWF Reanalysis, ERA-Interim [Dee *et al.*, 2011], available from 1979 to present. The data were obtained from the ECMWF Data Server. ERA-Interim is considered to have more accurate estimates of surface temperature in the polar regions [Jones and Harpham, 2013] than its predecessor, ERA-40 [Uppala *et al.*, 2005].

Monthly mean Arctic sea ice extents, generated from passive microwave satellite data, were downloaded from the National Snow and Ice Data Center (NSIDC) [Fetterer *et al.*, 2009]. The data are available from 1979 to present and use a 15% monthly mean concentration threshold for determining ice extent [Serreze *et al.*, 2007].

Snow cover data were obtained from the Rutgers University Global Snow Lab (accessible from <http://snowcover.org>). We used monthly Northern Hemisphere snow extent values from 1967 to 2012. The grid cells are considered fully snow-covered if they have at least 50% fractional snow cover; otherwise they are considered snow-free.

In our analyses we computed area-weighted averages of the Arctic (60-90°N unless otherwise noted) temperature, sea ice, and snow. Sea ice extent is defined as grid cells containing $\geq 15\%$ concentration, as is standard per NSIDC data. We define grid cells as snow-covered if they have at least 50% fractional snow cover, as per standard practice at NSIDC and the Rutgers Snow Lab. In the snow calculations for the GISS-E2-R model, we add to the CMIP5 RCP4.5 curve the anomaly of the geoengineering experiments with respect to the GeoMIP RCP4.5 run due to incongruities between

RCP4.5 runs produced for CMIP5 and GeoMIP. Throughout the analyses, differences in MIROC and MIROC-CHEM can be attributed both to differences in initial conditions, since they branch from different control runs, and to the inclusion of the chemistry module. Throughout this paper, we treat them as distinct models even though they are based on the same framework.

4.2 Results

4.2.1 Temperature

We first compute the global annual average temperature for the RCP4.5 (Control Run) from 1850-2100, G3 and G4 runs from 2020 onwards, and the available ERA-Interim 2 m temperature from 1979-present (Figure 4.1). The rate of warming in RCP4.5 from 2020-2070 averaged over all five models is 0.03 K/a. With the exception of BNU-ESM G3, global temperatures in G3 and G4 are unable to plateau despite sulfate aerosol injections from 2020-2070; instead they show an average increasing trend of 0.01 K/a (G3) and 0.02 K/a (G4) although some individual models still reach rates up to 0.03 K/a. The cooling response to G4 is initially strong, but by 2030 temperatures begin to increase again as the offset from the RCP4.5 run stabilizes with the formation of a stable stratospheric cloud, and allows for the slower ocean responses to occur. G3 shows more modest initial cooling, and generally less absolute decrease in temperature than G4 compared to RCP4.5.

We next analyze the near surface June-July-August (JJA) Arctic average temperatures, as ice and snow melt are closely related to summer temperatures [*Moore et al.*, 2013] (Figure 4.2). In the historical period, differences in preferred temperature state

between the models are evident; BNU-ESM temperature is roughly 3.5°C colder than the rest of the models pre-2020. As *Berdahl and Robock* [2013b] discussed, this has important implications for regions where temperature is near the freezing point, where the change of state of water can induce important climate feedbacks. In subsequent sections we will show that this impacts the amount of snow and ice produced in the models. In the G3 and G4 experiments, all models show a decrease in temperature relative to the Control Run beginning in 2020. In general, the geoengineering runs parallel the warming in the RCP4.5 cases for 2020-2070, albeit at a lower absolute temperature. The average 2020-2070 rate of warming for RCP4.5 is 0.04 K/a, while it is 0.03 K/a and 0.01 K/a for G4 and G3 respectively. The termination effect is visible after 2070, where temperatures rebound toward RCP4.5 temperatures. Differences in G3 and G4 are evident throughout the experiment. For example, G4 tends to produce a larger temperature decrease (by design), although in the BNU-ESM model, G3 sustains the largest negative temperature anomalies.

To assess the degree of Arctic amplification, we compute the ratio of Arctic to global warming trends from 2020-2070, shown in Table 4.2, for annual and relevant seasonal (JJA and SON) averages. Ratios greater than 1 imply the Arctic is warming at a faster rate than the global average, i.e., Arctic amplification. In all cases except BNU-ESM G3, there is an amplified warming in the Arctic. In the BNU-ESM G3 cases, denoted with an asterisk in Table 4.2, there is amplified cooling. The ratio in the BNU-ESM G3 annual average case is very large (5.8) since the global mean trend is very near zero so even small differences in the slope produce a large ratio. Results from this analysis suggest Arctic amplification is a persistent feature in all of the models and

experiments, an effect that is stronger in SON than in JJA. The stronger effect in fall than summer is consistent with the expectation of less sea ice, more open water, and the consequent warming of the lower Arctic troposphere, and with our previous understanding of winter Arctic amplification due to sea ice – thermal inertia feedbacks [Robock, 1983]. This also shows that in these geoengineering experiments, the Arctic warms faster than the global average, consistent with previous geoengineering studies [Lunt *et al.*, 2008; Govindasamy and Caldeira, 2000; Matthews and Caldeira, 2007; Kravitz *et al.*, 2013].

Figures 4.3 and 4.4 show the spatial distribution of temperature trends from 2030 to 2070 (beginning in 2030 so that we do not include immediate cooling from sudden implementation of sulfate loading) and 2070-2090, the period of rebound after geoengineering ceases, for each model. The rates of warming in both periods show large spatial variability, particularly in the geoengineering experiments. The BNU-ESM and HadGEM2-ES models show a weaker warming in the G3 experiment than the G4 experiment for 2030-2070. All three G3 models show very slight midlatitude warming, likely contributing to the global average temperature increases despite geoengineering. After the SRM forcing has ceased, the strong rebound toward warmer temperatures from 2070 to 2090, which reach up to 0.2 K/a in some locations, is evident in Figure 4.4, although again the rates are highly spatially variable.

4.2.2 Sea Ice

Figures 4.5-4.9 analyze the response of the Arctic sea ice extent to the G3 and G4 experiments. Figure 4.5 shows the sea ice extent over time for March (maximum annual

extent) and September (minimum annual extent). The BNU-ESM model simulates the highest sea ice extents on average, consistent with it being the coldest model in Arctic summers.

March sea ice extent is increased compared to the control run during the geoengineering runs, although when the sulfate injection is discontinued the ice extent falls back to RCP4.5 levels within 10 years. All-model average rates of March sea ice loss from 2020-2070 in RCP4.5 are 4×10^4 km²/a, whereas they are 3×10^4 km²/a and 1×10^4 km²/a for G4 and G3 respectively. September sea ice extent increases under G3 and G4, although there is still a negative trend overall. All-model average rates of September sea ice loss for 2020-2070 in RCP4.5 are 5×10^4 km²/a, whereas for G4 and G3 they are 4×10^4 km²/a and 1×10^4 km²/a respectively. These September rates do not include MIROC-ESM or MIROC-ESM-CHEM since those two models reach zero sea ice extent by 2060. In the case of the MIROC-ESM and MIROC-ESM-CHEM models, total loss of minimum annual ice occurs before 2060 despite geoengineering efforts. In all cases the minimum extents fall back to RCP4.5 levels within about ten years after sulfate loading ceases in 2070, leaving minimal, if any, September ice extent by 2090.

The differences between RCP4.5 and the geoengineering experiments are shown in Figure 4.6 for March and September. These show clear changes to sea ice extent as a result of geoengineering. In all models, an increase in sea ice extent compared to the control run is visible from 2020 to 2070 for both March and September. The changes in March extent are not as strong, partly because the aerosols will have more effect during summer when the sun is shining in the Arctic. Changes to circulation, meridional heat flux and clouds could also play a part in the differences in response between March and

September. Despite the apparent increases in ice extent as a result of geoengineering compared to the control run, ice extents still decrease overall during geoengineering (Figure 4.5). Figure 4.6 also emphasizes the strong termination effect, as ice extents fall to RCP4.5 levels often in less than a decade after 2070 as sulfate aerosol concentrations decay and high CO₂ concentrations begin to dominate the radiative balance.

Figure 4.7 shows maps of the average September sea ice extent boundaries, both from RCP4.5 for the period before geoengineering (2010-2019), and the last 10 years of geoengineering (2060-2069) for the RCP4.5, G4, and G3 experiments. The ability of G3 and G4 to maintain an expanded minimum sea ice state is evident in the BNU-ESM and GISS-E2-R models. In BNU-ESM, the G3 simulation sustains more ice than the G4, whereas the opposite is true for GISS-E2-R and HadGEM2-ES. Neither MIROC-ESM nor MIROC-ESM-CHEM retain significant amounts of ice in any of the experiments for the 2060-2070 period. Table 4.3 outlines how much September sea ice loss was prevented by the geoengineering experiments on average for 2060-2069 as compared to the control run average for 2010-2019. During the last decade of geoengineering (2060-2069), BNU-ESM-G3 and GISS-E2-R G4 prevented the loss of more than 50% of the sea ice as compared to their respective RCP4.5 runs. For all other models and scenarios the values were below 14%, suggesting weak efficacy of preventing sea ice loss. We suspect that part of the inter-model variation in the success of September ice loss prevention is related to the absolute JJA Arctic temperatures (Figure 4.2). That is, warmer models like the MIROC models lose sea ice completely regardless of geoengineering, whereas colder models such as GISS-E2-R and BNU-ESM tend to be more successful at retaining September sea ice extents.

We also analyzed decadal changes of sea ice extent (Figure 4.8). All models show a steady decrease in ice extent across all months for the entire experimental period, despite cooling efforts in both G3 and G4. In MIROC-ESM and MIROC-ESM-CHEM, it is clear that summer ice effectively disappears midway through the 21st Century. Another noteworthy feature of Figure 4.8 is the lengthening of the melt season with time. In the geoengineering simulations, as the decades progress, ice begins to melt faster and earlier and requires more time to rebuild into the fall and winter. Very similar results are found for sea ice volume, shown in Figure 4.9. MIROC-ESM and MIROC-ESM-CHEM sea ice volume is underestimated at the beginning of the 21st century and decreases rapidly, likely contributing to the weakness of the sea ice response to G4 forcing.

4.2.3 Snow Response

We analyze the historical and projected spring (April-June) Northern Hemisphere snow cover extent. Snow is typically limited to the Arctic during these months [*Derksen and Brown, 2012*]. The HadGEM2-ES model unfortunately did not output the fractional snow cover variable, so our analyses of snow cover are limited to the remaining four models.

Figure 4.10 shows the April, May and June snow extent, based on a 50% fractional cover threshold. Similar to the results for sea ice, the relatively cold BNU-ESM model generates the greatest snow cover area of all models available. Snow extents decrease beginning around the turn of the 21st Century and are projected to continue decreasing through to 2100 in the RCP4.5 simulations. This qualitative pattern is consistent among models and among all spring months. The G3 and G4 experiments generally show an increase in snow cover compared to the control run during the 2020-

2070 period in April, May and June, although the results show interannual variability. The models range in their responsiveness to sulfate aerosol injection. MIROC-ESM and MIROC-ESM-CHEM show the least response of snow cover in all months, while the BNU-ESM model tends to respond with the largest snow cover changes of all the models. The GISS-E2-R model shows very little response in the G3 experiment in terms of snow expansion. Similar to the sea ice and temperature results, after sulfate aerosol injection is halted, snow extents decrease back to RCP4.5 levels in less than a decade.

Table 4.4 shows the rates of change of snow extent cover for 2020-2070 in all simulations for April, May and June. In the RCP4.5 runs, snow loss rates are generally highest in April, followed by May and June. In all geoengineering cases, the rate of snow loss is slowed compared to the RCP4.5 run. All G4 and G3 simulations still show a decreasing snow extent trend, except for BNU-ESM G3 which effectively levels off or increases snow extents over time. MIROC-ESM and MIROC-ESM-CHEM models show few effects on reducing snow loss, similar to their performance with sea ice.

4.3 Summary

We find positive temperature trends during the geoengineering period from 2020 to 2070. The mean rate of warming in RCP4.5 from 2020-2070 is 0.03 K/a, while it is 0.02 K/a for G4 and 0.01 K/a in G3. Cooling is strong and immediate in G4 at 2020, but by 2030 temperatures begins to increase again as CO₂ levels dominate the 5 Tg sulfate aerosol/a inputs. G3 shows more modest initial cooling, and generally less absolute decrease in temperature than G4 compared to RCP4.5.

Arctic summer temperatures track the patterns of global annual averages. In general, the JJA temperatures show the same warming trend as the RCP4.5 cases from 2020 to 2070, but are offset relative to the RCP4.5 cases by a roughly constant negative value. We find there is still a persistent warming trend underlying the 50-year period of active geoengineering. The average 2020-2070 rate of warming for RCP4.5 is 0.04 K/a, whereas it is 0.03 K/a and 0.01 K/a for G4 and G3 respectively. Rates of warming are spatially and temporally variable, and as a consequence we suggest that actual stratospheric injection of SO₂ in the real world would produce variable outcomes. Further, the rebound to RCP4.5 temperatures after geoengineering is abruptly discontinued produces extreme rates of warming in certain regions, up to 0.2 K/a. We find statistically significant Arctic amplification in both the RCP4.5 and geoengineering experiments, predominantly in the form of amplified warming, but in the case of BNU-ESM G3, amplified Arctic cooling.

The G3 and G4 GeoMIP simulations indicate disagreement between the models regarding the response of Arctic sea ice to sulfate geoengineering. In two of the five models, the complete disappearance of September sea ice is not avoided by sulfate aerosol injection in the G4 experiment. In the models that do retain sea ice, G3 and G4 produce differing outcomes for different models; neither experiment is obviously more effective at retaining ice. Sea ice extents follow a negative trend through the geoengineering period despite sulfate aerosol injection: -5×10^4 km²/a for RCP4.5, -4×10^4 km²/a for G4 and -1×10^4 km²/a for G3. The percentage of sea ice loss that was prevented by the geoengineering experiments during the last decade of sulfate aerosol loading (2060-2069) as compared to the control run average for 2010-2019 reached

above 50% in the BNU-ESM G3 and GISS-E2-R G4 scenarios, but in all other scenarios the values were below 14% (Table 4.3). Models with warmer summer Arctic temperatures (MIROC-ESM and MIROC-ESM-CHEM) do not maintain September sea ice, while colder models (BNU-ESM and GISS-E2-R) are most successful at keeping September ice. No models are capable of retaining 2020 September sea ice extents throughout the entire geoengineering period. Generally, there is a decrease in ice extent in all months and a lengthening of the melt season in G3 and G4.

Post-2070 ice extents collapse back to RCP4.5 levels within roughly 10 years. Results from snow cover are commensurate with the ice and temperature responses. Except for BNU-ESM G3, spring snow cover areas are temporarily increased during the geoengineering years, again superimposed on a negative trend, followed by a quick decrease toward RCP4.5 values after 2070.

Despite some cooling, and the general ability of the models to retain greater areas of snow and ice than the RCP4.5 run, the degree of these effects are variable from year to year, model to model and experiment to experiment. Even then, ice and snow continue to melt, and temperatures continue to rise globally, with amplification in the Arctic. Given the termination effect, if warming is inevitable, slow rates are preferable to quick rates since drastic changes will have much more devastating impacts [*Parry et al.*, 2007]. Beyond the physical consequences of global warming such as ice and snow loss are the implications as a result of these changes, such as global sea level rise, ice sheet mass balance, water resources, wildlife habitat loss, and human activities in the Arctic.

4.4 Discussion and Conclusions

We show that SRM in the form of sulfate aerosol loading in the G3 and G4 experiments is successful at producing some global annual average temperature cooling. With the exception of BNU-ESM G3, the global average temperatures in G3 do not remain at the level of 2020 values. This is in contrast to the results found for G1 [*Kravitz et al.*, 2013; *Moore et al.*, 2013] and G2 [*Jones et al.*, 2013], where global average temperatures and sea ice are generally kept constant by SRM efforts. The difference between G1 and G2 on the one hand, and G3 on the other, is that G1 and G2 are very artificial, starting with a balanced control run. G3 branches from a realistic global warming simulation, so even though TOA net radiation is kept at 2020 values, global warming still occurs. The lag in ocean response to the initial forcing produces a small, but non-negligible, continued warming. With Arctic amplification, this continued warming is felt even more strongly in the regions with snow and sea ice.

This means that, if the goal of a geoengineering implementation were to stop global warming, or to stop snow and sea ice melting and keep them at the levels that existed at the time of the initiation of geoengineering, a global average negative net radiative forcing would be necessary. If the goal were to restore snow and sea ice to their values in a previous year, an even larger negative forcing would have to be imposed, such as in G4, but it would have to increase over time in the absence of mitigation. This would impose an even larger termination effect than shown here, should society lose the will or means to continue stratospheric aerosol injection.

CHAPTER 5: SUMMARY AND DISCUSSION

5.1 Summary

The work presented in this dissertation examined the effects of natural (past) and anthropogenic (future) sulfate aerosols on the Arctic cryosphere. Chapters 2 and 3 were motivated by proxy evidence suggesting successive volcanic eruptions suppressed summer temperatures enough to cause expanded snow cover and sea ice in the Eastern Canadian Arctic beginning in the late 13th century [Zhong *et al.*, 2010; Miller *et al.*, 2012]. Chapter 4 is motivated by the potential sulfate aerosol injections into the lower stratosphere for the purpose of geoengineering in the future.

In Chapter 2, I used a high-resolution regional climate model (WRF) to examine the effect that post-eruption conditions – namely, a sudden suppression of temperatures, reduction of incoming solar radiation, and expansion of sea ice – might have on snow cover after only one summer season on Baffin Island. The results showed that expanded sea ice has the strong potential to reduce inland temperatures, particularly in the fall months when an otherwise warm open ocean is covered in ice so that turbulent heat flux to the atmosphere is suppressed. The WRF model showed excellent correspondence between snow expansion patterns and where past demarcations indicate the LIA snowline to have been [Williams, 1978a]. I found that the region responding with most sensitivity to a summer temperature reduction was the northern Baffin Island plateau between 400 and 700 m elevation. Here, with a summer temperature reduction of -3.9 ± 1.1 K from the Control Run, the snowline lowered by 350 m, similar to the reconstructed LIA snowline of Williams [1978a]. I showed that a temperature decrease from current conditions of

roughly 1.2–2.4 K would be necessary to reproduce the observations by *Miller et al.* [2012]. Arctic averaged decadal summer temperature anomaly estimates based on a composite of proxy records shows about 1.5 K difference between the LIA and current values [*Kaufman et al.*, 2009]. Thus, if Baffin regional temperatures during the LIA were roughly 2 K lower than present (which is reasonable, given the proxy records), and there was a more extensive sea ice cover, this together would have been enough to perpetuate an ice sheet on Baffin Island throughout the LIA.

In Chapter 3 I assessed the PMIP3 Last Millennium (LM) simulations in terms of temperature, snow, and ice response to large volcanic eruptions. I focused on the North Atlantic and eastern Canadian Arctic regions in order to determine if current state-of-the-art models produce sudden and persistent cold conditions after strong volcanic eruptions. Most models produced significantly cooler temperatures in the Arctic and in the North Atlantic region during the LIA; however, the magnitude of cooling was much less than expected from proxy records. None of the models produced centennial-scale sea ice expansion as was seen in *Miller et al.* [2012]. Snow cover over Baffin Island showed large-scale expansion in less than half of the available models, never sustained beyond a decade. The PMIP3 models' lack of sustained cooling response could be due to their inability to capture changes in ocean circulation, which other studies have shown can lead to centennial-scale cooling in the North Atlantic. Additionally the lack of sustained cooling could have been due to biased mean regional climates in the models. I found that there was a large spread in the models' background climates in the NH, Arctic, and over Baffin Island. In more than half of the models, warm summer climates over Baffin Island stunted snow expansion after volcanic eruptions completely. Thus, I argue that it is

crucial to properly represent absolute temperatures, particularly in areas such as the Arctic where small fluctuations in temperature can cause water to change phases. This is especially important, since snow and ice presence can further induce feedbacks, such as ice albedo, which may influence global climate but cannot be triggered from volcanic forcing in models whose background climates are too warm.

In Chapter 4 I examined the potential effects of future sulfate aerosol geoengineering on the Arctic cryosphere. I showed that SRM in the form of sulfate aerosol loading in the G3 and G4 experiments of GeoMIP is successful at producing some global annual average temperature cooling. However, since global average temperatures still increased over the experiment period, sea ice and snow extents still decreased. With Arctic amplification, this continued warming was felt even more strongly in the regions with snow and sea ice. After geoengineering ceased, model temperatures rebounded quickly – the termination effect – and sea ice and snow showed high rates of decline.

Possible implications of these results depend on the goal of geoengineering. If the purpose of a geoengineering implementation was to stop global warming or to stop snow and sea ice melting and keep them at the levels that existed at the time of the initiation of geoengineering, a global average negative net radiative forcing would be necessary. If the goal was to restore snow and sea ice to their values in a previous year, an even larger negative forcing would have to be imposed, and in the absence of mitigation it would have to increase over time. Should society lose the will or means to continue stratospheric aerosol injection, this would produce an even larger termination effect than shown in our analysis.

5.2 Discussion

Changes in the Arctic cryosphere have global implications. The loss of Arctic land ice is already contributing significantly to global sea level rise and is projected to continue to make substantial contributions in the coming century [Meier *et al.*, 2007]. Greenland ice melt has the potential to change global ocean circulation – and thus continental scale climate - since the addition of freshwater to the North Atlantic can influence deepwater formation [Hu *et al.*, 2011]. Further, the loss of sea ice influences mid-latitude dynamics in addition to the obvious implications for the traditional lifestyles of native communities and the natural ecosystems that depend on ice presence. These global implications of Arctic cryosphere changes, compounded with the phenomenon of Arctic Amplification, deem it essential to understand how this region has and will change as a result of changes in climate forcing.

All in all, the studies presented in this thesis provide new insights into how the Arctic climate system responds to large injections of sulfate aerosols. Whether by natural or anthropogenic means, Arctic temperature – and consequently snow and sea ice cover - is notably more sensitive to sudden reductions in incoming solar radiation than the global average. Both proxy records and models show that the cooling response to the large volcanic eruptions in the 13th century was highly variable spatially. To assess these types of issues regarding regional climate change, we can derive value both from high-resolution regional climate models, and global climate models. Global climate models usually couple atmosphere, ocean and land surface models so that a whole and consistent representation of large scale circulation and climate variability is produced. Yet, while GCMs are quickly improving in resolution, regional climate models can still better

resolve complex topography in more focused regions. They account for sub-GCM grid scale forcings and enhance the simulations of atmospheric circulations at fine spatial scales.

In this dissertation, both regional and global climate models provided valuable insights to Arctic climate change, but were of course imperfect. The regional climate model I used was able to resolve the complex topography of Baffin Island which had critical implications for snow and ice persistence during the descent into the Little Ice Age. The model accurately predicted the regions into which snow would prefer to expand under colder conditions. Unfortunately, it had issues producing enough cloud cover; too few clouds caused exaggerated diurnal temperature cycles which further impacted snow melt rates.

Meanwhile, global climate models in the PMIP3 and the GeoMIP simulations showed significant spread in Arctic background climate, which had impacts on ice and snow when temperatures were near the freezing point. The PMIP3 models varied in the strength of their response to strong volcanic eruptions. Thus, getting the wrong background climate in addition to the wrong magnitude of response to a volcanic eruption has important ramifications in regions where the temperature is near the freezing point and water forms as a solid or liquid. The phase of water in the environment has strong impacts on climate. For example, snow presence dramatically increases albedo and sea ice decouples the ocean and atmosphere. Similar to the PMIP3 models, the warmest GeoMIP models were unable to retain sea ice and snow despite geoengineering. Again, this emphasizes how crucial it is to accurately model regional mean climate as absolute temperatures.

Further work focusing more on Greenland would be interesting to pursue, especially in terms of the response to geoengineering in the G3 and G4 scenarios. How much would sea level rise be mitigated under these scenarios? Would melting along the margins of the ice sheet be slowed? If so, how much? How much would this change the contributions to sea level rise in the coming century? How much sulfate injection would be necessary to cease Greenland Ice Sheet decay? Further, it would be also interesting to look more closely at the ecological impacts of the termination effect in more detail. Organisms may adapt to climate change by either shifting their range or by adapting to different conditions. Because both of these are gradual processes, the rate of environmental change is important, not just the end points. Therefore, the use and termination of geoengineering may pose a greater extinction risk than a more gradual, non-mitigated scenario.

REFERENCES

- Ahmed, M., et al. (2013), Continental-scale temperature variability during the past two millennia, *Nature Geoscience*, 6, 339-346, doi: 10.1038/NGE01797.
- Anchukaitis, K. J., et al. (2012), Tree rings and volcanic cooling, *Nat. Geosci.*, 5(12), 836–837.
- Anderson, R., G. Miller, J. Briner, N. Lifton, and S. DeVogel (2008), A millennial perspective on arctic warming from 14C in quartz and plants emerging from beneath ice caps, *Geophys. Res. Lett.*, 35(1), L01502,doi:10.1029/2007GL032057.
- Andrews, J. T., R. G. Barry, R. S. Bradley, G. H. Miller, and L. D. Williams (1972), Past and present glaciological responses to climate in eastern Baffin Island, *Quat. Res.*, 2(3), 303–314.
- Bao, Q., et al. (2013), The flexible global ocean-atmosphere-land system model, spectral version 2: FGOALS-s2, *Adv. Atmos. Sci.*, 30, 561–576.
- Barlage, M., F. Chen, M. Tewari, K. Ikeda, D. Gochis, J. Dudhia, R. Rasmussen, B. Livneh, M. Ek, and K. Mitchell (2010), Noah land surface model modifications to improve snowpack prediction in the Colorado Rocky Mountains, *J. Geophys. Res.*, 115, D22101, doi:10.1029/2009JD013470.
- Barnes, J. E. and D. J. Hoffman (1997), Lidar measurements of stratospheric aerosol over Mauna Loa Observatory, *Geophys. Res. Lett.*, 24(15), 1923-1926.
- Berdahl, M., and A. Robock (2013a), Baffin Island snow extent sensitivity: Insights from a regional climate model, *J. Geophys. Res. Atmos.*, 118, 3506–3519, doi:10.1029/jgrd.50249.
- Berdahl, M., and A. Robock (2013b), Northern Hemispheric cryosphere response to volcanic eruptions in the Paleoclimate Modeling Intercomparison Project 3 last millennium simulations, *J. Geophys. Res. Atmos.*, 118, 12,359-12,370, doi:10.1002/2013JD019914.
- Berdahl, M. et al. (2014), Arctic cryosphere response in the Geoengineering Model Intercomparison Project (GeoMIP) G3 and G4 scenarios, *J. Geophys. Res. Atmos.*, in press.
- Bluth, G. J. S., S. D. Doiron, S. C. Schnetzler, A. J. Krueger, and L. S. Walter (1992), Global tracking of the SO₂ clouds from the June, 1991 Mount Pinatubo eruptions, *Geophys. Res. Lett.*, 19, 151 – 154, doi:10.1029/91GL02792.

- Brown, R. D. and D. A. Robinson (2011), Northern Hemisphere spring snow cover variability and change over 1922-2010 including an assessment of uncertainty, *Cryosphere*, 5, 219–229, doi:10.5194/tc-5-219-2011.
- Bradley, B.S., and P. D. Jones (1993), ‘Little Ice Age’ summer temperature variations: Their nature and relevance to recent global warming trends, *Holocene*, 3(4), 367–376.
- Briffa, K. R., P. D. Jones, F. H. Schweingruber, and T. J. Osborn (1998), Influence of volcanic eruptions on Northern Hemisphere summer temperature over the past 600 years, *Nature*, 393, 450–455, doi:10.1038/30943.
- Briffa, K. R., T.J. Osborn, F.H. Schweingruber, I.C. Harris, P.D. Jones, S.G. Shiyatov, E.A. Vaganov (2001), Low-frequency temperature variations from a northern tree ring density network, *J. Geophys. Res.*, 106 (D3), 2929–2941, doi:10.1029/2000JD900617.
- Brohan, P., R. Allan, E. Freeman, D. Wheeler, C. Wilkinson, and F. Williamson (2012), Constraining the temperature history of the past millennium using early instrumental observations, *Clim. Past*, 8, 1551–1563, doi:10.5194/cp-8-1551-2012.
- Brown, R., C. Derksen, and L. Wang (2007), Assessment of spring snow cover duration variability over northern Canada from satellite datasets, *Remote Sens. Environ.*, 111(2–3), 367–381.
- Brown, R., C. Derksen, and L. Wang (2010), A multi-data set analysis of variability and change in Arctic spring snow cover extent, 1967–2008, *J. Geophys. Res.*, 115(D16), D16111, doi:10.1029/2010JD013975.
- Callaghan, T. V., et al. (2011), The changing face of Arctic snow cover: A synthesis of observed and projected changes, *AMBIO*, 40, 17–31, doi:10.1007/s13280-011-0212-y.
- Cassano, J. J., M. E. Higgins, and M. W. Seefeldt (2011), Performance of the Weather Research and Forecasting (WRF) model for month-long pan-Arctic simulations, *Mon. Wea. Rev.*, 139, 3469–3488, doi:10.1175/MWR-D-10-05065.1.
- Catchpole, A. J. W., and I. Hanuta (1989), Severe summer ice in Hudson Strait and Hudson Bay following major volcanic eruptions, 1751 to 1889 A.D., *Climatic Change*, 14, 61–79.
- Chen, F., and J. Dudhia (2001), Coupling an advanced land surface hydrology model with the Penn State-NCAR MM5 modeling system. Part I: Model implementation and sensitivity, *Mon. Wea. Rev.*, 129(4), 569–585.
- Chou, M.-D., and M. Suarez (1994), An efficient thermal infrared radiation parameterization for use in general circulation models, *NASA Tech. Memo.*, 104606, 85 pp.

- Collins, W. J., et al. (2011), Development and evaluation of an Earth-System model - HadGEM2, *Geosci. Model Dev.*, *4*, 1051-1075, doi:10.5194/gmd-4-1051-2011.
- Collins, M., S. F. B. Tett, and C. Cooper (2001), The internal climate variability of HadCM3, a version of the Hadley Centre Coupled Model without flux adjustments, *Clim. Dyn.*, *17*(1), 61–81.
- Crowley, T. J., G. Zielinski, B. Vinther, R. Udisti, K. Kreutzs, J. Cole-Dai, and E. Castellano (2008), Volcanism and the Little Ice Age, *PAGES Newsllett.*, *16*, 22–23.
- Crutzen, P. J. (2006), Albedo enhancements by stratospheric sulfur injections: A contribution to resolve a policy dilemma? An Editorial Essay, *Clim. Change*, *77*, 211–219.
- Dai, Y., et al. (2003), The Common Land Model (CLM), *Bull. Am. Met. Soc.*, *84*, 1013-1023, doi:10.1175/BAMS-84-8-1013.
- Dai, Y., R. E. Dickinson, and Y.-P. Wang (2004), A two-big-leaf model for canopy temperature, photosynthesis, and stomatal conductance, *J. Clim.*, *17*, 2281-2299, doi:10.1175/1520-0442(2004)017<2281:ATMFCT>2.0.CO;2.
- Dee, D. P., et al. (2011), The ERA-Interim reanalysis: configuration and performance of the data assimilation system, *Q.J.R. Meteorol. Soc.*, *137*, 553-597, doi:10.1002/qj.828.
- Delaygue, G., and E. Bard (2011), An Antarctic view of Beryllium-10 and solar activity for the past millennium, *Clim. Dyn.*, *36*, 2201–2218, doi:10.1007/s00382-010-0795-1.
- Derksen, C., and R. Brown (2012), Spring snow cover extent reductions in the 2008–2012 period exceeding climate model projections, *Geophys. Res. Lett.*, *39*, L19504, doi:10.1029/2012GL053387.
- Fetterer, F., K. Knowles, W. Meier, and M. Savoie. 2002, updated 2009. *Sea Ice Index*. [Sea Ice Extent]. Boulder, Colorado USA: National Snow and Ice Data Center. <http://dx.doi.org/10.7265/N5QJ7F7W>.
- Fogt, R. L., and D. H. Bromwich (2008), Atmospheric moisture and cloud cover characteristics forecast by AMPS, *Weather Forecast.*, *23*, 914–930, doi:10.1175/2008WAF2006100.1.
- Francis, J. A. and S. J. Vavrus (2012), Evidence linking Arctic amplification to extreme weather in mid-latitudes, *Geophys. Res. Lett.* *39*, L06801, doi:10.1029/2012GL051000.
- Frank, D. C., J. Esper, C. C. Raible, U. Buentgen, V. Trouet, B. Stocker, and F. Joos (2010), Ensemble reconstruction constraints on the global carbon cycle sensitivity to climate, *Nature*, *463*, 527–530, doi:10.1038/nature08769.

- Gao, C., A. Robock, and C. Ammann (2008), Volcanic forcing of climate over the past 1500 years: An improved ice core-based index for climate models, *J. Geophys. Res.*, *113*, D23111, doi:10.1029/2008JD010239.
- Gardner, A. S., M. J. Sharp, R. M. Koerner, C. Labine, S. Boon, S. J. Marshall, D. O. Burgess, D. Lewis (2009), Near-surface temperature lapse rates over Arctic glaciers and their implications for temperature downscaling, *J. Clim.*, *22*, 4281–4298, doi:10.1175/2009JCLI2845.1
- Geirsdóttir, Á., G. H. Miller, T. Thordarson, and K. Ólafsdóttir (2009), A 2000 year record of climate variations reconstructed from Haukadalsvatn, west Iceland, *J. Paleolimnol.*, *41*(1), 95–115, doi:10.1007/s10933-008-9253-z.
- Gent, P. R., et al. (2011), The Community Climate System Model version 4, *J. Clim.*, *24*, 4973–4991, doi:10.1175/2011JCLI4083.1.
- Govindasamy, B., and K. Caldeira (2000), Geoengineering Earth's radiation balance to mitigate CO₂-induced climate change, *Geophys. Res. Lett.*, *27*, 2141–2144.
- Greuell, W., and R. Böhm (1998), 2m temperatures along melting midlatitude glaciers, and implications for the sensitivity of the mass balance to variations in temperature, *J. Glaciol.*, *44*, 9–20.
- Hall, D. K., G. A. Riggs, J. L. Foster and S. V. Kumar (2010), Development and evaluation of cloud-gap-filled MODIS daily snow-cover product, *Remote Sens. Environ.*, *114*(3), 496–503, doi:10.1016/j.rse.2009.10.007.
- Hegerl, G. C., T. Crowley, M. Allen, W. T. Hyde, H. Pollack, J. Smerdon and E. Zorita (2007), Detection of human influence on a new 1500 yr climate reconstruction, *J. Climate*, *20*, 650–666.
- Hines, K. M., D. H. Bromwich, L.-S. Bai, M. Barlage, and A. G. Slater (2011), Development and testing of Polar WRF. Part III. Arctic land. *J. Clim.*, *24*, 26–48, doi:10.1175/2010JCLI3460.1.
- Hines, K. M. and D. H. Bromwich, (2008), Development and testing of Polar Weather Research and Forecasting (WRF) model. Part I: Greenland ice sheet meteorology, *Mon. Wea. Rev.*, *136*, 1971–1989, doi:10.1175/2007MWR2112.1.
- Hong, S., J. Dudhia, and S. Chen (2004), A revised approach to ice microphysical processes for the bulk parameterization of clouds and precipitation, *Mon. Wea. Rev.*, *132*, 103–120.
- Hong, S., Y. Noh, and J. Dudhia (2006), A new vertical diffusion package with an explicit treatment of entrainment processes, *Mon. Wea. Rev.*, *134*(9), 2318–2341, doi:10.1175/MWR3199.1.

- Hu, A., Meehl, G.A., Han, W. and J. Yin (2011), Effect of the potential melting of the Greenland Ice Sheet on the Meridional Overturning Circulation and global climate in the future, *Deep-Sea Research II*, 58, 1914-1926.
- Ikeda, K., et al. (2010), Simulation of seasonal snowfall over Colorado, *Atmos. Res.*, 97(4), 462–477, doi:10.1016/j.atmosres.2010.04.010.
- Irvine, P.J., D.J. Lunt, E.J. Stone, and A. Ridgwell (2009), *Environ. Res. Lett.*, 4, doi:10.1088/1748-9326/4/4/045109.
- Ives, J. D., (1962), Indications of recent extensive glacierization in north central Baffin Island, N.W.T., *J. Glaciol.*, 4, 197–205.
- Jansen, E., et al. (2007), Palaeoclimate, in *Climate Change 2007: The Physical Science Basis—Contribution of Working Group I to the Fourth Assessment Report of the Intergovernmental Panel on Climate Change*, edited by S. Solomon et al., pp. 463–497, Cambridge Univ. Press, Cambridge, U.K.
- Jones, P. D., K. R. Briffa, T. P. Barnett and T. S.B. Tett (1998), High-resolution palaeoclimatic records for the last millennium: interpretation, integration and comparison with General Circulation Model control-run temperatures. *Holocene*, 8, 455e471.
- Jones, P. D., M. New, D. E. Parker, S. Martin, and I. G. Rigor (1999), Surface air temperature and its change over the past 150 years, *Rev. Geophys.*, 37, 173–199.
- Jones, A., et al. (2010), Geoengineering by stratospheric SO₂ injection: results from the Met Office HadGEM2 climate model and comparison with the Goddard Institute for Space Studies ModelE, *Atmos. Chem. Phys.*, 10, 5999-6006, doi: 10.5194/acp-10-5999-2010.
- Jones, A., et al. (2013), The impact of abrupt suspension of solar radiation management (termination effect) in experiment G2 of the Geoengineering Model Intercomparison Project (GeoMIP), *J. Geophys. Res. Atmos.*, 118, 9743-9752, doi:10.1002/jgrd.50762.
- Kain, J. (2010), The Kain-Fritsch convective parameterization: An update, *J. Appl. Meteor.*, 43(1), 170–181, doi:10.1175/1520-450(2004)043<0170:TKCPAU>2.0.CO;2.
- Kaufman, D. S., et al. (2009), Recent warming reverses long-term Arctic cooling, *Science*, 325(5945), 1236–1239.
- Kinnard, C., C. M. Zdanowicz, D. A. Fisher, E. Isaksson, A. de Vernal, and L. G. Thompson (2011), Reconstructed changes in Arctic sea ice over the past 1,450 years, *Nature*, 479(7374), 509–512.

- Koerner, R. M. (2005), Mass balance of glaciers in the Queen Elizabeth Islands, Nunavut, Canada, *Ann. Glaciol.*, 42, 417–423.
- Kravitz, B., et al. (2013), Climate model response from the Geoengineering Model Intercomparison Project (GeoMIP), *J. Geophys. Res. Atmos.*, 118, 8320–8332, doi:10.1002/jgrd.50646.
- Kravitz, B., et al. (2011a), The Geoengineering Model Intercomparison Project (GeoMIP), *Atmos. Sci. Lett.*, 12, 162–167, doi: 10.1002/asl.316.
- Kravitz, B., et al. (2011b), Specifications for GeoMIP experiments G1 through G4. Available online at http://climate.envsci.rutgers.edu/GeoMIP/docs/specificationsG1_G4_v1.0.pdf [accessed June 12, 2013].
- Landrum, L., B. L. Otto-Bliesner, E. R. Wahl, A. Conley, P. J. Lawrence, N. Rosenbloom, and H. Teng (2013), Last millennium climate and its variability in CCSM4, *J. Clim.*, 26, 1085–1111, doi:10.1175/JCLI-D-11-00326.1.
- Lane, L., K. Caldeira, R. Chatfield, and S. Langhoff (Eds.) (2007), Workshop report on managing solar radiation, *NASA/CP-20070214558*, 31 pp.
- Langway, C. C., Jr., K. Osada, H. B. Clausen, C. U. Hammer, and H. Shoji (1988), An inter-hemispheric volcanic time-marker in ice cores from Greenland and Antarctica, *Ann. Glaciol.*, 10, 102–108.
- Lauder, B., and J. M. T. Thompson (Eds.) (2009), *Geo-Engineering Climate Change: Environmental Necessity or Pandora's Box?*, Cambridge University Press, Cambridge, UK.
- Lavigne, F., et al. (2013), Source of the great A.D. 1257 mystery eruption unveiled, Samalas volcano, Rinjani Volcanic Complex, Indonesia, *Proc. Natl. Acad. Sci. U. S. A.*, doi:10.1073/pnas.1307520110, in press.
- Lenton, T. M., and N. E. Vaughan (2009), The radiative forcing potential of difference climate geoengineering options, *Atm. Chem. Phys.*, 9, 5539–5561.
- Lucas-Picher, P., M. Wulff-Nielsen, J. Christensen, G. Aalgeirsdóttir, R. Mottram, and S. Simonsen (2012), Very high resolution regional climate model simulations over Greenland: Identifying added value, *J. Geophys. Res.*, 117(D2), D02108, doi:10.1029/2011JD016267.
- Lunt, D. J., A. Ridgwell, P. J. Valdes, and A. Seale (2008), ‘Sunshade World’: a fully coupled GCM evaluation of the climatic impacts of geoengineering, *Geophys. Res. Lett.*, 35, L12710.
- Mann, M. E., Z. Zhihua, M. K. Hughes, R. S. Bradley, S. K. Miller, S. Rutherford, and F. Ni (2008), Proxy-based reconstructions of hemispheric and global surface

- temperature variations over the past two millennia, *Proc. Natl. Acad. Sci. U.S.A.*, *105*(36), 13,252–13,257, doi:10.1073/pnas.0805721105.
- Mann, M. E., Z. Zhang, S. Rutherford, R. S. Bradley, M. K. Hughes, D. Shindell, C. Ammann, G. Faluvegi, and F. Ni (2009), Global signatures and dynamical origins of the Little Ice Age and Medieval Climate Anomaly, *Science*, *326*(5957), 1256–1260.
- Mann, M. E., J. D. Fuentes, and S. Rutherford (2012), Underestimation of volcanic cooling in tree-ring-based reconstructions of hemispheric temperatures, *Nat. Geosci.*, *5*, 202–205, doi:10.1038/NGEO1394.
- Marsland, S. J., H. Haak, J. H. Jungclaus, M. Latif, and F. Roeske (2003), The Max-Planck-Institute global ocean/sea ice model with orthogonal curvilinear coordinates, *Ocean Modell.*, *5*, 91–127.
- Marti, O., et al. (2010), Key features of the IPSL ocean atmosphere model and its sensitivity to atmospheric resolution, *Clim. Dyn.*, *34*, 1–26.
- Matthews, H. D., and K. Caldeira (2007), Transient climate-carbon simulations of planetary geoengineering, *Proc. Nat. Acad. Sci.*, *104*, 9949–9954.
- McCormick, M., L. Thomason, and C. Trepte (1995), Atmospheric effects of the Mt. Pinatubo eruption, *Nature*, *373*(6513), 399–404, doi:10.1038/373399a0.
- Meehl, G. A., et al. (2012), Climate system response to external forcings and climate change projections in CCSM4, *J. Climate*, *25*, 3661–3683, doi:10.1175/JCLI-D-11-00240.1.
- Meier, M. F., et al. (2007), Glaciers dominate eustatic sea-level rise in the 21st Century, *Science*, *317*, 1064–1067, doi:10.1126/science.1143906.
- Mignot, J., M. Khodri, C. Frankignoul, and J. Servonnat (2011), Volcanic impact on the Atlantic Ocean over the last millennium, *Clim. Past*, *7*, 1439–1455, doi:10.5194/cp-7-1439-2011.
- Miguez-Macho, G., G. Stenchikov, and A. Robock (2004), Spectral nudging to eliminate the effects of domain position and geometry in regional climate model simulations, *J. Geophys. Res.*, *109*, D13104, doi:10.1029/2003JD004495.
- Miller, G. H. (1973), Late quaternary glacial and climatic history of northern Cumberland Peninsula, Baffin Island, N.W.T., Canada, *Quaternary Res.*, *3*, 561–583.
- Miller, G. H., et al. (2010), Temperature and precipitation history of the Arctic, *Quat. Sci. Rev.*, *29*(15–16), 1679–1715, doi:10.1016/j.quascirev.2010.03.001.
- Miller, G. H., et al. (2012), Abrupt onset of the Little Ice Age triggered by volcanism and sustained by sea-ice/ocean feedbacks, *Geophys. Res. Lett.*, *39*, L02708, doi:10.1029/2011GL050168.

- Miller, G. H., et al. (2013) Unprecedented recent summer warmth in Arctic Canada, *Geophys. Res. Lett.*, *40*, doi:10.1002/2013GL057188.
- Mlawer, E., S. Taubman, P. Brown, M. Iacono, and S. Clough (1997), Radiative transfer for inhomogeneous atmospheres: RRTM, a validated correlated-k model for the longwave, *J. Geophys. Res.*, *102*(D14), 16, 663–16, doi:10.1029/97JD00237.
- Moore, J. C., et al. (2013), Arctic sea ice and atmospheric circulation under the GeoMIP G1 scenario, submitted to *J. Geophys. Res.*
- Moss, R. H., et al. (2010), The next generation of scenarios for climate change research and assessment, *Nature*, *463*, 747–756, doi:10.1038/nature08823.
- National Ice Center (2008), IMS daily Northern Hemisphere snow and ice analysis at 4 km and 24 km resolution. (National Snow and Ice Data Center Boulder, CO). Digital media. http://nsidc.org/data/docs/noaa/g02156_ims_snow_ice_analysis.
- Niemeier, U., H. Schmidt, and C. Timmreck (2011), The dependency of geoengineered sulfate aerosol on the emission strategy. *Atmos. Sci. Lett.*, *12*, 189–194. doi:10.1002/asl.304
- NSIDC (2012), Arctic sea ice news and news analysis. Available online at <http://nsidc.org/arcticseaicenews/2012/09/arctic-sea-ice-extent-settles-at-record-seasonal-minimum/> [accessed June 23, 2013].
- Otterå, O. H., M. Bentsen, H. Drange, and L. Suo (2010), External forcing as a metronome for Atlantic multidecadal variability, *Nat. Geosci.*, *3*, 688–694.
- Overpeck, J. et al. (1997), Arctic environmental change of the last four centuries, *Science*, *278*, 1251–1256, doi:10.1126/science.278.5341.1251.
- Parry, M. L., O. F. Canziani, J. P. Palutikof and Co-authors (eds.) (2007), *Technical Summary. Climate Change 2007: Impacts, Adaptation and Vulnerability. Contribution of Working Group II to the Fourth Assessment Report of the Intergovernmental Panel on Climate Change*, Cambridge University Press, Cambridge, UK, 23–78.
- Phipps, S. J. (2010), The CSIRO Mk3L climate system model v1.2, Technical Report No. 4, Antarctic Climate & Ecosystems CRC, Hobart, Tasmania, Australia, 122 pp., ISBN 978-1-921197-04-8.
- Raddatz, T. J., C. H. Reick, W. Knorr, J. Kattge, E. Roeckner, R. Schnur, K. G. Schnitzler, P. Wetzler, and J. Jungclaus (2007), Will the tropical land biosphere dominate the climate-carbon cycle feedback during the twenty-first century?, *Clim. Dyn.*, *29*, 565–574, doi:10.1007/s00382-007-0247-8.

- Rasch, P. J., et al. (2008), An overview of geoengineering of climate using stratospheric sulfate aerosols, *Phil. Trans. R. Soc. A*, 366, 4007-4037, doi: 10.1098/rsta.2008.0131.
- Robock, A. (1983), Ice and snow feedbacks and the latitudinal and seasonal distribution of climate sensitivity, *J. Atmos. Sci.*, 40, 986-997.
- Robock, A. (2000), Volcanic eruptions and climate, *Rev. Geophys.*, 28, 191-219.
- Robock, A., L. Oman, and G. L. Stenchikov (2008), Regional climate responses to geoengineering with tropical and Arctic SO₂ injections, *J. Geophys. Res.*, 113, D16101, doi:10.1029/2008JD010050.
- Robock, A., A. B. Marquardt, B. Kravitz, and G. Stenchikov (2009), The benefits, risks and costs of stratospheric geoengineering, *Geophys. Res. Lett.*, 36, L19703, doi:10.1029/2009GL039209.
- Robock, A. (2000), Volcanic eruptions and climate, *Rev. Geophys.*, 38, 191-219.
- Schleussner, C. F., and G. Feulner (2013), A volcanically triggered regime shift in the subpolar North Atlantic Ocean as a possible origin of the Little Ice Age, *Clim. Past*, 9, 1321-1330, doi:10.5194/cp-9-1321-2013.
- Schmidt, G. A., et al. (2006), Present-day atmospheric simulations using GISS ModelE: Comparison to in situ, satellite and reanalysis data, *J. Clim.*, 19, 153-192, doi:10.1175/JCLI3612.1.
- Schmidt, G. A., et al. (2011), Climate forcing reconstructions for use in PMIP simulations of the last millennium (v1.0), *Geosci. Model Dev.*, 4, 33-45, doi:10.5194/gmd-4-33-2011.
- Schneider, D. P., C. M. Ammann, B. L. Otto-Bliesner, and D. S. Kaufman (2009), Climate response to large, high-latitude and low-latitude volcanic eruptions in the Community Climate System Model, *J. Geophys. Res.*, 114, D15101, doi:10.1029/2008jd011222.
- Schaefer, K., T. Zhang, L. Bruhwiler and A.P. Barrett (2011), Amount and timing of permafrost carbon release in response to climate warming. *Tellus 63B*, 165-180, doi: 10.1111/j.1600-0889.2011.00527.x.
- Screen, J., and I. Simmonds (2010), The central role of diminishing sea ice in recent Arctic temperature amplification, *Nature*, 464, 1334-1337, doi: 10.1038/nature09051.
- Serreze, M. C., and J. A. Francis (2006), The Arctic amplification debate, *Clim. Change* 76, 241-264.

- Serreze, M. C., M. M. Holland, and J. Stroeve (2007), Perspectives on the Arctic's shrinking ice cover. *Science*, *315*, 1533-1536.
- Serreze, M. C., et al. (2009), The emergence of surface-based Arctic amplification. *Cryosphere*, *3*, 11-19.
- Shepherd, J., et al. (2009), *Geoengineering the climate: Science, governance and uncertainty*, Royal Society Policy document 10/09. (Royal Society, London), 82 pp.
- Shindell, D. T., G. A. Schmidt, R. L. Miller, and M. E. Mann (2003), Volcanic and solar forcing of climate change during the preindustrial era, *J. Clim.*, *16*, 4094–4107.
- Skamarock, W., et al. (2008) A description of the advanced research WRF version 3, NCAR Tech. Note NCAR/TN-475+ STR.
- Solomon, S., et al., (eds.) (2007), *Climate Change 2007: The Physical Science Basis*, Cambridge Univ. Press.
- Steinhilber, F., J. Beer, and C. Frohlich (2009), Total solar irradiance during the Holocene, *Geophys. Res. Lett.*, *36*, L19704, doi:10.1029/2009GL040142.
- Stroeve, J. C., V. Kattsov, A. Barrett, M. Serreze, T. Pavlova, M. Holland and W.N. Meier (2012), Trends in Arctic sea ice extent from CMIP5, CMIP3 and observations. *Geophys. Res. Lett.* *39*, L19502, doi: 10.1029/2012GL052676.
- Tilmes, S., R. Muller, and R. Salawitch (2008), The sensitivity of polar ozone depletion to proposed geoengineering schemes, *Science*, *320*, 1201-1204, doi:10.1126/science.1153966.
- Timmreck, C., S. J. Lorenz, T. J. Crowley, S. Kinne, T. J. Raddatz, M. A. Thomas, and J. H. Jungclaus (2009), Limited temperature response to the very large AD 1258 volcanic eruption, *Geophys. Res. Lett.*, *36*, L21708, doi:10.1029/2009GL040083.
- Timmreck, C., H.-F. Graf, S. J. Lorenz, U. Niemeier, D. Zanchettin, D. Matei, J. H. Jungclaus, and T. J. Crowley (2010), Aerosol size confines climate response to volcanic super-eruptions, *Geophys. Res. Lett.*, *37*, L24705, doi:10.1029/2010GL045464.
- Tingley, M. P., and P. Huybers (2013), Recent temperature extremes at high northern latitudes unprecedented in the past 600 years, *Nature*, *496*, 201-205, doi:10.1038/nature11969.
- Toohey, M., K. Kruger, U. Niemeier, and C. Timmreck (2011), The influence of eruption season on the global aerosol evolution and radiative impact of tropical volcanic eruptions, *Atmos. Chem. Phys.*, *11*, 12,351–12,367, doi:10.5194/acp-11-12351-2011.
- Uppala, S. M., et al. (2005), The ERA-40 reanalysis, *Q. J. R. Meteorol. Soc.*, *131*, 2961-3012, doi:10.1256/qj.04.176.

- Vieira, L. E. A., and S. Solanki (2010), Evolution of the solar magnetic flux on time scales of years to millenia, *Astron. Astrophys.*, 509, doi:10.1051/0004-6361/200913276.
- Wang, L., M. Sharp, R. Brown, C. Derksen, and B. Rivard (2005a), Evaluation of spring snow covered area depletion in the Canadian arctic from NOAA snow charts, *Remote Sens. Environ.*, 95(4), 453–463, doi:10.1016/j.rse.2005.01.006.
- Wang, L., M. Sharp, B. Rivard, S. J. Marshall, and D. Burgess (2005b), Melt season duration on Canadian Arctic ice caps, 2000–2004, *Geophys. Res. Lett.*, 32(19), L19502, doi:10.1029/2005GL023962.
- Wang, Y. M., J. L. Lean, and N. R. Sheeley Jr. (2005c), Modeling the Sun's magnetic field and irradiance since 1713, *Astrophys. J.*, 625, 522–538.
- Wang, M., and J. E. Overland (2012), A sea ice free summer Arctic within 30 years – and update from the CMIP5 models, *Geophys. Res. Lett.*, 39, L18501, doi:10.1029/2012GL052868.
- Watanabe, S., et al. (2011), MIROC-ESM 2010: Model description and basic results of CMIP5-20c3m experiments, *Geosci. Mod. Dev.*, 4, 845-872, doi:10.5194/gmd-4-845-2011.
- Wigley, T. M. L. (2006), A combined mitigation/geoengineering approach to climate stabilization, *Science*, 314, 452-454, doi:10.1126/science.1131728.
- Williams, L. D. (1978a), The Little Ice Age glaciation level on Baffin Island, Arctic Canada, *Palaeogeogr. Palaeoclim.*, 25, 199–207.
- Williams, L. D. (1978b), Ice-sheet initiation and climatic influences of expanded snow cover in Arctic Canada, *Quaternary Res.*, 10(2), 141–149.
- Wilson, A., D. Bromwich, and K. Hines (2011), Evaluation of Polar WRF forecasts on the arctic system reanalysis domain: Surface and upper air analysis, *J. Geophys. Res.*, 116, D11112, doi:10.1029/2010JD015013.
- Wilson, A., D. Bromwich, and K. Hines (2012), Evaluation of Polar WRF forecasts on the Arctic System Reanalysis domain: 2. Atmospheric hydrologic cycle, *J. Geophys. Res.*, 117, D04107, doi:10.1029/2011JD016765.
- Wu, T., et al. (2013), Global carbon budgets simulated by the Beijing Climate Center Climate System Model for the last century, *J. Geophys. Res. Atmos.*, 118, 4326–4347, doi:10.1002/jgrd.50320.
- Zanchettin, D., O. Bothe, H. F. Graf, S. J. Lorenz, J. Luterbacher, C. Timmreck, and J. H. Jungclaus (2013), Background conditions influence the decadal climate response to strong volcanic eruptions, *J. Geophys. Atmos.*, 118, 4090–4106, doi:10.1002/jgrd.50299.

- Zhang, J. and D. A. Rothrock (2003), Modeling global sea ice with a thickness and enthalpy distribution model in generalized curvilinear coordinates, *Mon. Wea. Rev.*, *131*, 845-861, doi:10.1175/1520-0493(2003)131<0845:MGSIWA> 2.0.CO;2.
- Zhong, Y., G. H. Miller, B. Otto-Bliesner, M. Holland, D. Bailey, D. Schneider, and A. Geirsdottir (2010), Centennial-scale climate change from decadal paced explosive volcanism: A coupled sea ice-ocean mechanism, *Clim. Dyn.*, *37*, 1–15, doi:10.1007/s00382-010-0967-z.

TABLES

Table 2.1. Environment Canada AWS stations, April-September 2005.

Station	Latitude (°N)	Longitude (°W)	Elevation (m)	Frequency
Chesterfield Inlet	63.35	90.73	9.8	Daily
Clyde River	70.48	68.52	26.5	Daily
Coral harbor	64.19	83.36	62.2	Hourly and Daily
Cape Dorset	64.23	76.53	48.2	Daily
Cape Hooper	68.47	66.82	390.1	Hourly
Dewar Lakes	68.65	71.17	526.7	Hourly
Gjoa Haven	68.64	95.85	46.9	Daily
Hall Beach	68.78	81.24	9.1	Hourly and Daily
Iqaluit	63.75	68.55	33.5	Hourly and Daily
Kugaaruk	68.54	89.80	15.5	Daily
Nanisivik	72.98	84.62	641.9	Daily
Pangnirtung	66.15	65.71	24.1	Daily
Pond Inlet	72.69	77.97	61.6	Daily
Qikiqtarjuaq	67.55	64.03	5.5	Daily
Repulse Bay	66.52	86.22	22.9	Daily
Resolute	74.72	94.98	30.0	Hourly and Daily
Taloyoak	69.55	93.58	27.4	Daily

Table 2.2. Correlation coefficient, r , between WRF Control Run 2 m temperature and station temperature with and without the seasonal cycle removed. To compute r , hourly data are sampled every 6 hours to match the 6 hourly WRF output. Stations that report hourly also report daily averages, so for these locations r is calculated for both. All correlations are highly significant, with p values of < 0.01 (Student's t -test).

Station	Frequency of Record	Correlation coefficient, r	Correlation coefficient, r , after removing seasonal cycle
Chesterfield Inlet	Daily	0.96	0.68
Clyde River	Daily	0.93	0.60
Coral Harbor	Hourly	0.94	0.69
Coral Harbor	Daily	0.96	0.67
Cape Dorset	Daily	0.93	0.59
Cape Hooper	Hourly	0.90	0.42
Cape Hooper	Daily	0.93	0.63
Dewar Lakes	Hourly	0.92	0.51
Dewar Lakes	Daily	0.95	0.64
Gjoa Haven	Daily	0.95	0.61
Hall Beach	Hourly	0.93	0.52
Hall Beach	Daily	0.94	0.43
Iqaluit	Hourly	0.87	0.52
Iqaluit	Daily	0.90	0.53
Kugaaruk	Daily	0.95	0.56
Nanisivik	Daily	0.94	0.40
Pangnirtung	Daily	0.94	0.59
Pond Inlet	Daily	0.95	0.41
Qikiqtarjuaq	Daily	0.93	0.56
Repulse Bay	Daily	0.97	0.66
Resolute	Hourly	0.93	0.57
Resolute	Daily	0.95	0.65
Taloyoak	Daily	0.97	0.61

Table 2.3. Minimum snow cover percent of inner domain for each WRF run.

WRF Run	Minimum Snow Cover (%)
-6 K	17.0
-4.5 K	10.1
-3 K	9.4
-1.5 K	9.2
Control	9.2
95 Solcon	9.2
FixedSI	9.2
-3 K & FixedSI	9.4

Table 3.1. Last Millennium Simulations modeling groups and model acronyms and volcanic and solar forcing, adapted from *Brohan et al.* [2012].

Acronym	Modeling Group	Volcanic/Solar Forcing
BCC	Beijing Climate Center, China Meteorological Administration [<i>Wu et al.</i> , 2012]	<i>Gao et al.</i> [2008] / <i>Vieira et al.</i> , [2010]
GISSG	NASA Goddard Institute for Space Studies [<i>Schmidt et al.</i> , 2006]	<i>Gao et al.</i> [2008] / <i>Vieira et al.</i> , [2010]
GISSC	NASA Goddard Institute for Space Studies [<i>Schmidt et al.</i> , 2006]	<i>Crowley et al.</i> [2008] / <i>Vieira et al.</i> , [2010]
FGOALS	LASG, Institute of Atmospheric Physics, Chinese Academy of Sciences [<i>Bao et al.</i> , 2013; <i>Man and Zhou</i> , 2013]	<i>Gao et al.</i> [2008] / <i>Vieira et al.</i> , [2010]
MIROC	Japan Agency for Marine-Earth Science and Technology, Atmosphere and Ocean Research Institute (The University of Tokyo), and National Institute for Environmental Studies [<i>Watanabe et al.</i> , 2010]	<i>Crowley.</i> [2008] / Delaygue and Bard [2011] and Wang et al. [2005c]
MPI	Max Planck Institute for Meteorology [<i>Raddatz et al.</i> , 2007; <i>Marsland et al.</i> , 2003]	<i>Crowley et al.</i> [2008] / <i>Vieira et al.</i> , [2010] and Wang et al. [2005c]
CCSM4	National Center for Atmospheric Research [<i>Gent et al.</i> , 2011]	<i>Gao et al.</i> [2008] / <i>Vieira et al.</i> , [2010]
IPSL	Institut Pierre-Simon Laplace [<i>Marti et al.</i> , 2010]	<i>Gao et al.</i> [2008] / <i>Vieira et al.</i> , [2010] and Wang et al. [2005c]
CSIRO	The Commonwealth Scientific and Industrial Research Organization [<i>Phipps</i> , 2010]	<i>Crowley et al.</i> [2008]/ <i>Steinhilber et al.</i> , [2009]
HadCM3	Hadley Center [<i>Collins et al.</i> , 2001]	<i>Crowley et al.</i> , [2008]/ <i>Steinhilber et al.</i> , [2009]

Table 3.2. Top 10 eruptions for the *Gao et al.* [2008] and *Crowley et al.* [2008] datasets based on aerosol optical depth (AOD).

Intensity Rank	<i>Gao et al.</i> [2008]		<i>Crowley et al.</i> [2008]	
	Year	AOD	Year	AOD
1	1258	0.97	1258	0.66
2	1783	0.62	1816	0.40
3	1227	0.39	1809	0.29
4	1815	0.39	1641	0.28
5	1600	0.31	1600	0.26
6	1176	0.31	1228	0.18
7	1452	0.30	1460	0.15
8	1641	0.23	1668	0.15
9	939	0.21	1585	0.14
10	1719	0.21	1024	0.14

Table 3.3. Temperature, sea ice and snow anomaly responses per unit forcing (UF) integrated from year 0 to year 10 lag after the eruption. Average forcing for the top 10 eruptions in terms of aerosol optical depth (Table 3.2) is used to compute response per UF. Anomalies are calculated from the 5 year pre-eruption climatology. A 10 year pre-eruption climatology was tested as well but made minimal difference to the results.

Model	NH Ann. Temp (K/UF)	NH JJA Temp (K/UF)	Baffin Ann. Temp (K/UF)	Baffin JJA Temp (K/UF)	NH Sea Ice Area ($\times 10^6$ km²/UF)	NA Sea Ice Area ($\times 10^6$ km²/UF)	NH Snow Area ($\times 10^6$ km²/UF)	Baffin Snow Area ($\times 10^6$ km²/UF)
BCC	-3.5	-2.6	-8.4	-12.4	16.0	3.4	2.0	0.1
GISSG	-10.4	-10.2	-25.1	-40.9	24.1	5.3	9.8	3.0
GISSC	-10.2	-9.6	-57.6	-48.4	20.8	4.8	5.5	1.9
CCSM4	-8.4	-8.2	-35.1	-18.4	7.1	3.5	9.5	3.1
MIROC	-5.0	-4.1	-3.8	-7.6	13.5	1.8	3.3	0.0
MPI	-11.9	-10.9	-1.5	-49.9	14.8	1.8	0.2	0.0
IPSL	-6.4	-6.2	-51.1	-28.1				
CSIRO	-7.2	-6.3	-9.6	-10.9	10.5	2.1		
FGOALS	-6.4	-5.7	-15.5	-6.0				
HadCM3	-10.7	-10.2	-20.9	-20	16.8	2.6		

Table 4.1. Models participating in GeoMIP that have thus far run the G3 and G4 experiments, and number of ensemble members simulated for each group.

Models in G3	Models in G4	Ensemble Members
BNU-ESM	BNU-ESM	1
<i>Dai et al. [2003, 2004]</i>	<i>Dai et al. [2003, 2004]</i>	
GISS-E2-R	GISS-E2-R	3
<i>Schmidt et al. [2006]</i>	<i>Schmidt et al. [2006]</i>	
HadGEM2-ES	HadGEM2-ES	3
<i>Collins et al. [2011]</i>	<i>Collins et al. [2011]</i>	
	MIROC-ESM	1
	<i>Watanabe et al. [2011]</i>	
	MIROC-ESM-CHEM	1
	<i>Watanabe et al. [2011]</i>	

Table 4.2. Ratio of Arctic (60-90°N) to global average temperature trends for the annual average, June-July-August (JJA) and September-October-November (SON) from 2020 to 2070. Values equal to 1 indicate identical rates of warming, and values greater than 1 indicate Arctic amplification. Asterisks in BNU-ESM G3 denote negative temperature trends in the Arctic and global average temperatures. Results for MIROC-ESM and MIROC-ESM-CHEM in the G3 experiments are unavailable as of this publication. All cases of Arctic amplification are statistically significant.

MODEL	Annual Average			JJA Average			SON Average		
	RCP4.5	G4	G3	RCP4.5	G4	G3	RCP4.5	G4	G3
BNU-ESM	2.5	2.2		1.5	1.5		3.1	3.3	
			5.8*			3.0*			4.3*
GISS-E2-R	1.3	1.1	1.2	0.9	0.8	0.6	1.7	1.6	1.7
HadGEM2-ES	2.5	2.9	3.0	1.3	1.4	1.5	2.7	3.2	3.2
MIROC-ESM	2.3	2.3	n/a	1.6	1.5	n/a	2.3	2.7	n/a
MIROC-ESM-CHEM	2.2	2.5	n/a	1.5	1.6	n/a	2.3	2.7	n/a
Average	2.2	2.2	3.4	1.4	1.4	1.7	2.4	2.7	3.1

Table 4.3. Percent of September sea ice loss that was prevented by the geoengineering experiments during the last decade of sulfate aerosol loading (2060-2069) as compared to the control run average from 2010-2019. These are computed as $(G_f - C_f)/(C_i - C_f)$ where the subscripts f and i denote the final (2060-2069) and initial (2010-2019) period respectively and G and C refer to the Geoengineering and Control runs.

Model	G4 Experiment	G3 Experiment
BNU-ESM	7.7 %	60.8 %
GISS-E2-R	54.7 %	3.5 %
HadGEM2-ES	13.4 %	4.9 %
MIROC-ESM	0.2 %	n/a
MIROC-ESM-CHEM	0.0 %	n/a

Table 4.4. Change of snow extent from 2020 to 2070. Units are thousands of square km ($\times 10^3 \text{ km}^2$).

MODEL	April			May			June		
	RCP4.5	G4	G3	RCP4.5	G4	G3	RCP4.5	G4	G3
BNU-ESM	-52	-47	6	-87	-52	25	-19	-15	14
GISS-E2-R	-49	-7	-41	-23	-17	-21	-19	-11	-12
MIROC- ESM	-114	-103	n/a	-81	-77	n/a	-39	-55	n/a
MIROC- ESM-CHEM	-126	-107	n/a	-88	-85	n/a	-43	-40	n/a
Average	-85	-66	-17	-70	-58	2	-30	-30	1

FIGURES

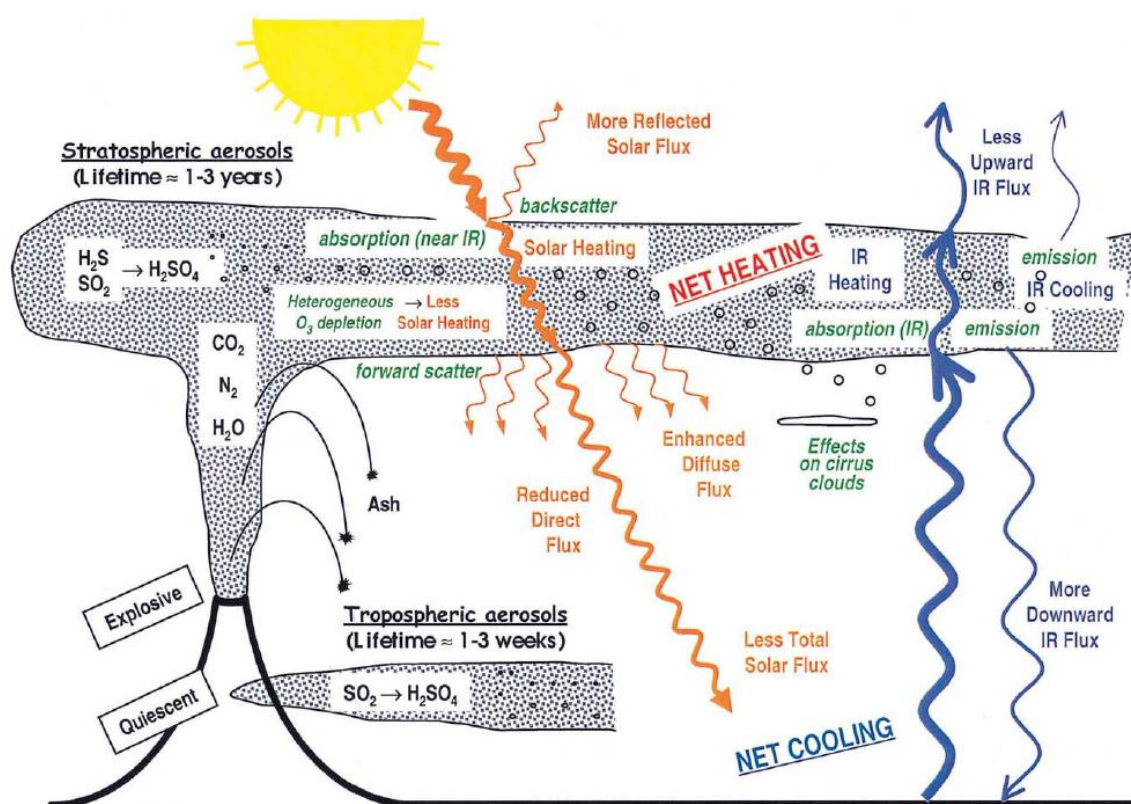


Figure 1.1 Schematic of volcanic inputs to the atmosphere and their effects. From Robock [2000].

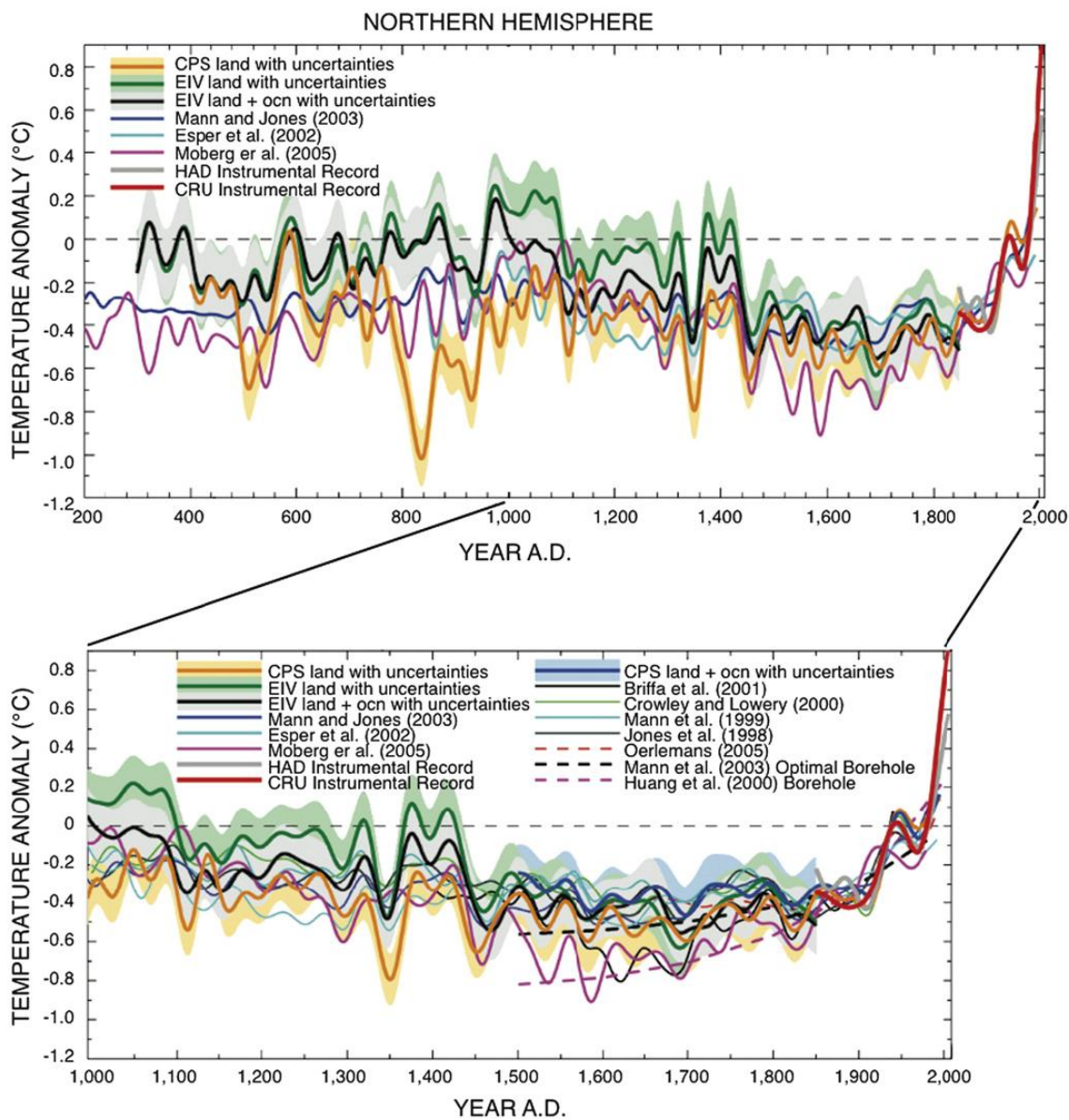


Figure 1.2 Composite proxy-data reconstruction of Northern Hemisphere temperatures for most of the last 2000 years, compared with other published reconstructions. Estimated confidence limits, 95%. All series have been smoothed with a 40 year low-pass filter. Generally the reconstructions show agreement in broad climate changes over the past 2 millennia. Taken from *Miller et al.* [2010].

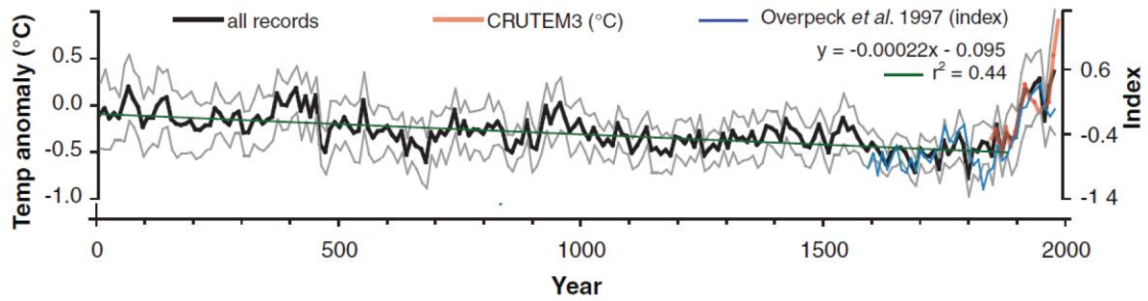


Figure 1.3 Mean of high-resolution proxy records transformed to Arctic summer temperature anomaly relative to the 1961-1990 reference period, with first order linear trend for all records through 1900 (green line), the 400-year-long Arctic-wide temperature index of *Overpeck et al.* [1997] (blue curve; 10-year means), and the 10-year-mean Arctic temperature through 2008 (red line). Gray lines encompass ± 2 standard errors of the proxy values as evaluated for each 10-year interval. Figure taken from *Kaufman et al.* [2009].

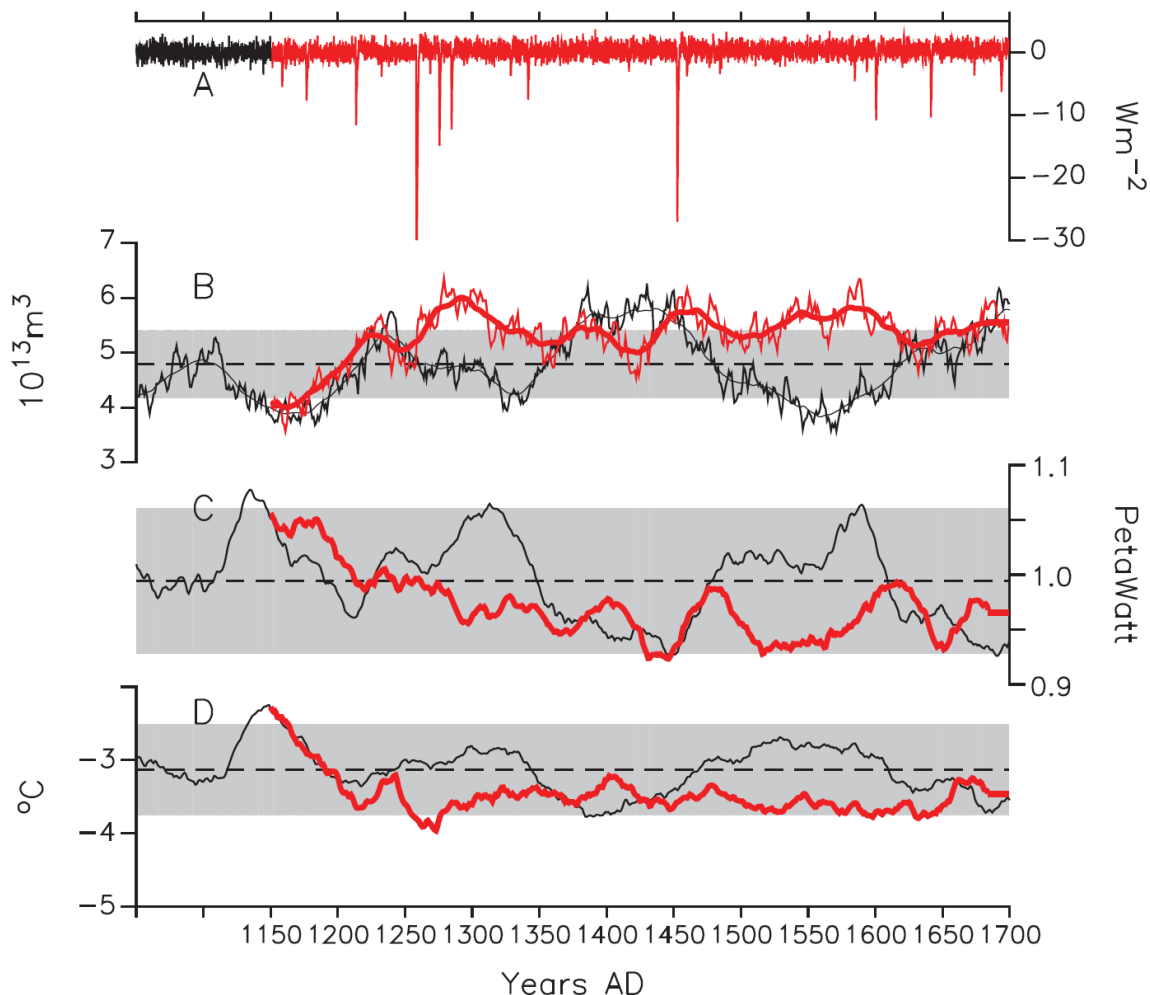


Figure 1.4 Climate model results for control run (black), and volcanically perturbed run beginning in 1150 CE (red). Black dashed lines and gray bars show mean and standard deviation of the control run. (a) Monthly global downwelling surface shortwave radiation anomalies forced by aerosol loadings [Gao *et al.*, 2008]. (b) Yearly and 30-year running mean of NH sea ice volume in September. (c) 30-year running mean of the northward heat transport in the North Atlantic at $26^{\circ}N$. (d) 30-year running mean of average summer (JJA) surface air temperature over North Atlantic Arctic land ($<60^{\circ}N$ and $90^{\circ}W$ to $30^{\circ}E$). Figure taken from Miller *et al.* [2012].

Average Monthly Arctic Sea Ice Extent September 1979 - 2013

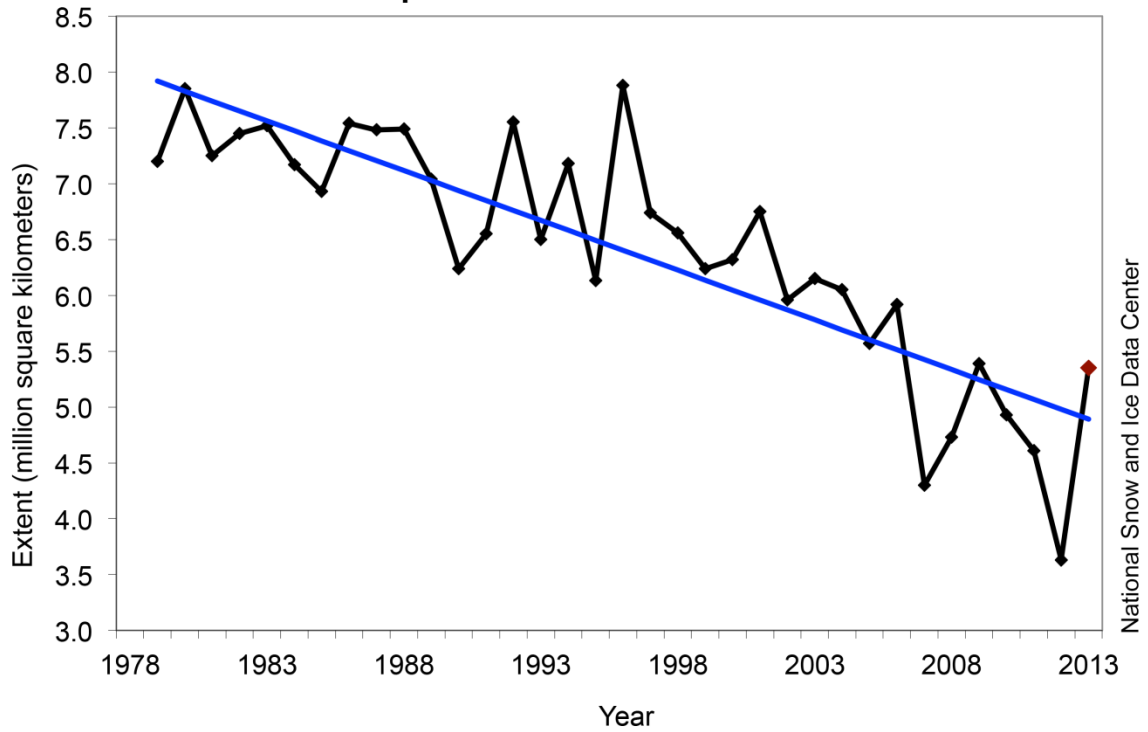


Figure 1.5 Average monthly Arctic sea ice extent (million square kilometers) during the satellite era. Figure courtesy NSIDC (<http://nsidc.org/arcticseaicenews/>).

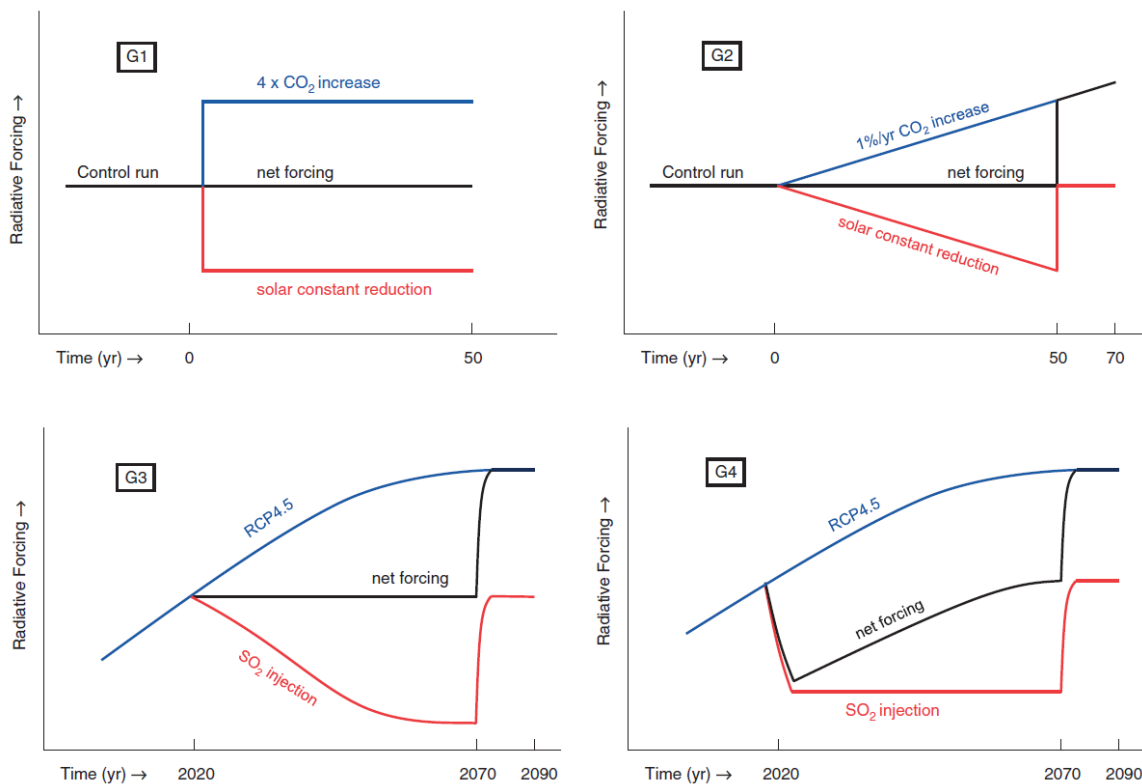


Figure 1.6 Schematic of experiments G1, G2, G3 and G4 of the GeoMIP project. G1 and G2 start with a pre-industrial control run and artificially balance artificial quadrupling and 1%/yr increases of CO₂ by a reduction in the solar constant until year 50. G3 and G4 use RCP4.5 as their control run. G3 approximately balances the TOA radiative forcing with injection of SO₂ into the tropical lower stratosphere from the year 2020-2070. G4 injects 5 Tg per year of SO₂ into the lower tropical stratosphere from 2020-2070. G3 and G4 are allowed to continue running for 20 years (2070-2090) without stratospheric geoengineering. Figures from *Kravitz et al.* [2011].

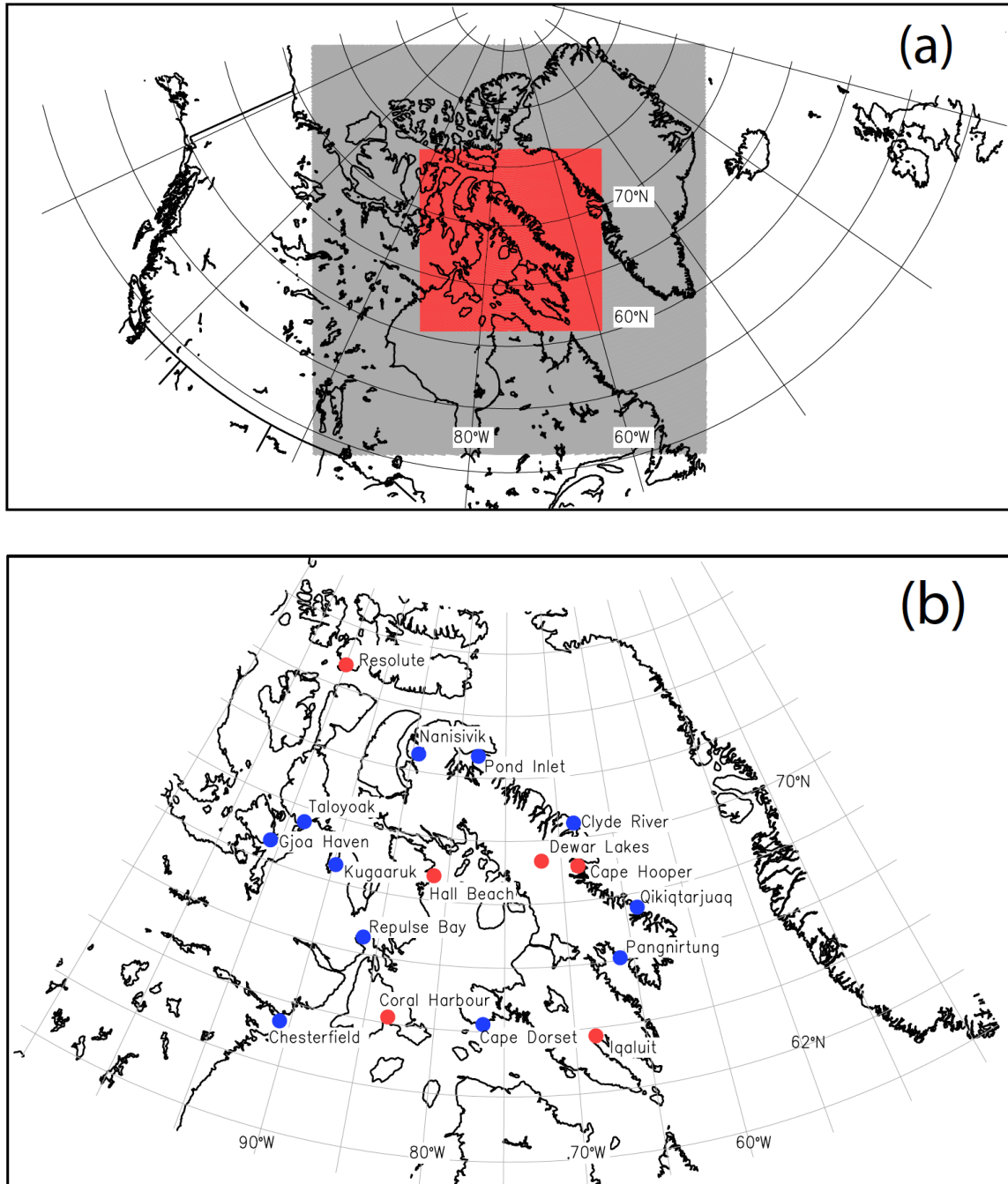


Figure 2.1 (a) Map of WRF domains, where parent domain (grey) has 30 km resolution and child domain (red) has 10 km resolution. (b) Automatic weather station locations, where red circles denote hourly data available and blue denote only daily average records available.

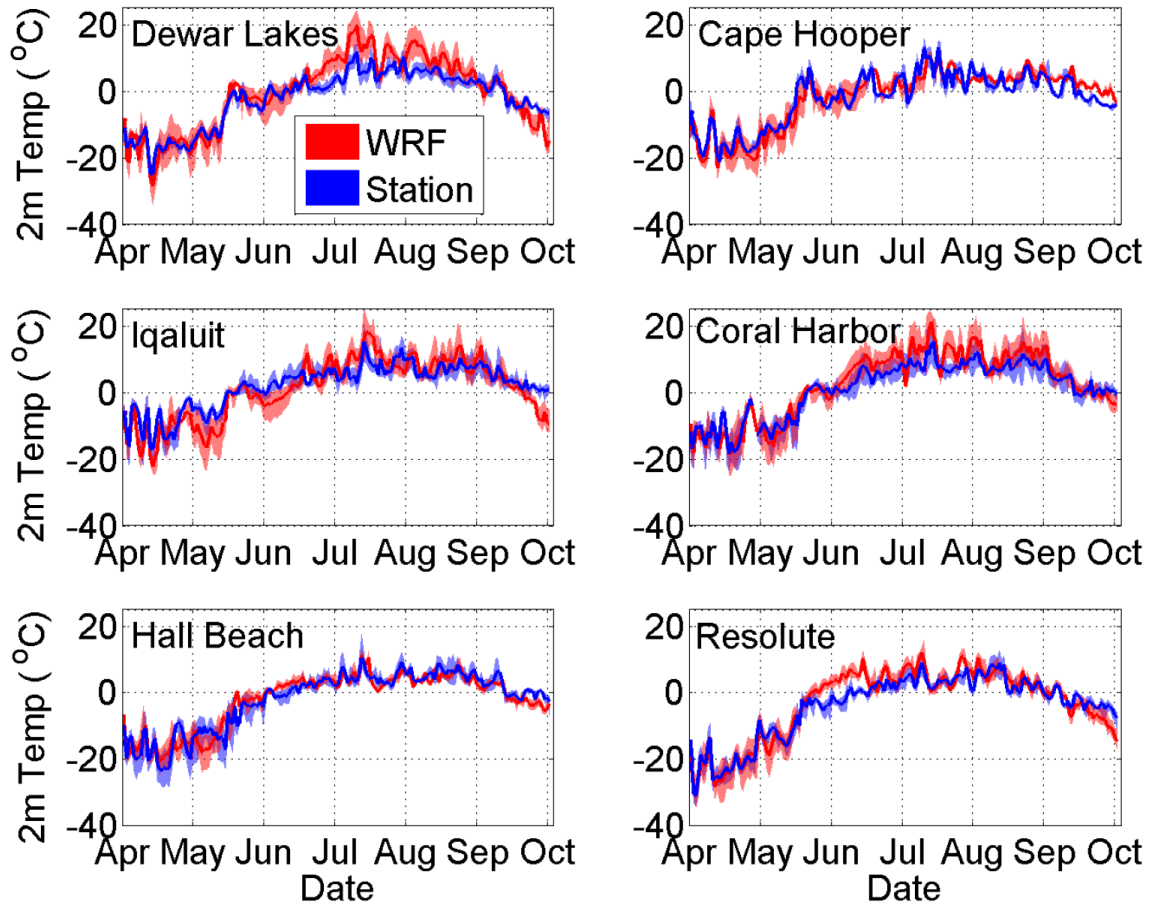


Figure 2.2. 2 m station (blue) and WRF Control Run (red) mean temperatures (bold lines) and maximum and minimum daily ranges (shaded blue and red). Dewar Lakes, the only inland station on Baffin Island, shows the poorest simulation by WRF.

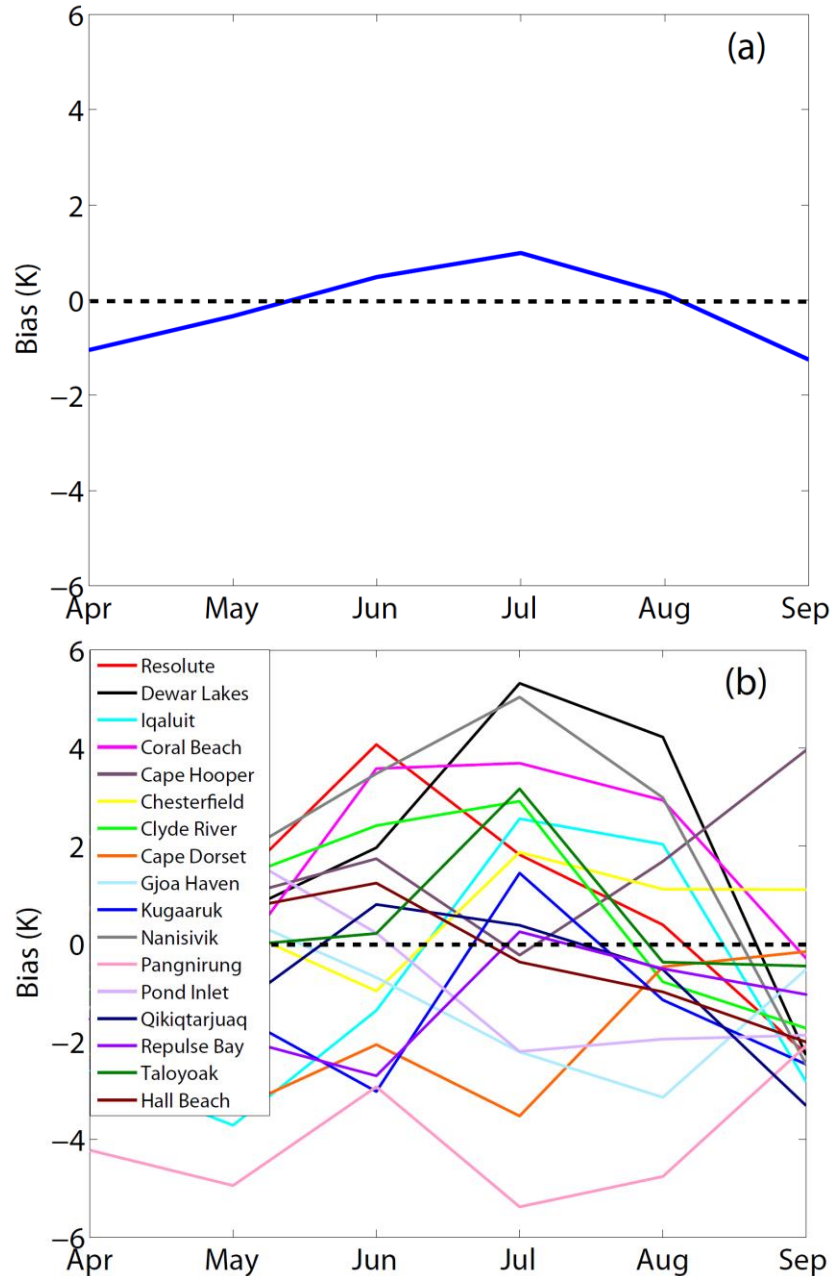


Figure 2.3. (a) Average monthly bias of WRF Control Run (WRF Control-Station) at all available station locations in the inner domain. (b) Monthly temperature difference between control run and observations for the 17 available station locations. When station curves are above the dotted line, WRF over-predicts the temperature on average for that month at that station.

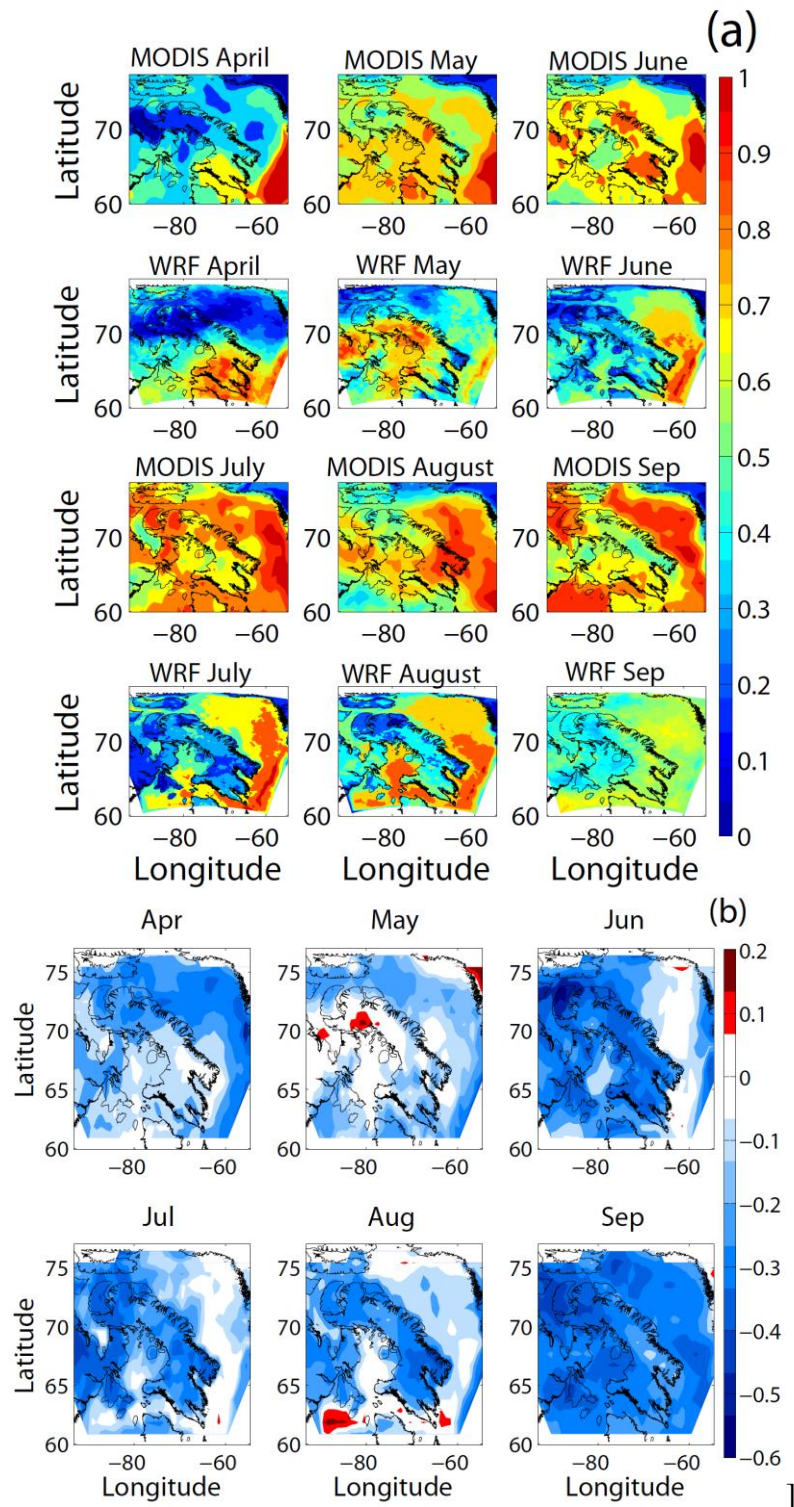


Figure 2.4. (a) Monthly average cloud fraction from MODIS Aqua observations and WRF Control Run output for 2005, and (b) monthly average cloud fraction difference between WRF and MODIS.

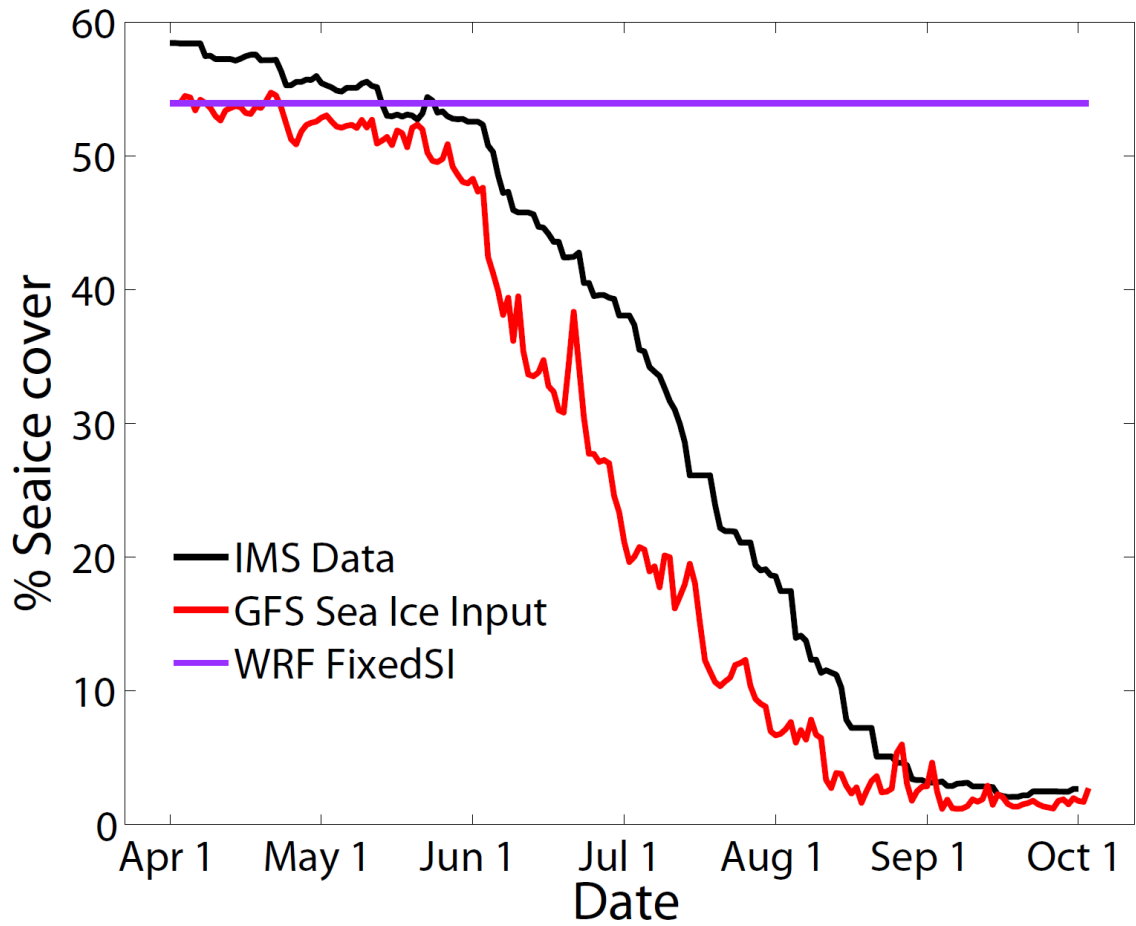


Figure 2.5. Percent of sea ice cover of the inner domain with time for IMS observations, GFS input to WRF, and the Fixed SI WRF experiment. GFS prescribes WRF's boundary conditions, including that of sea ice distribution, and they are updated every 6 h of model time.

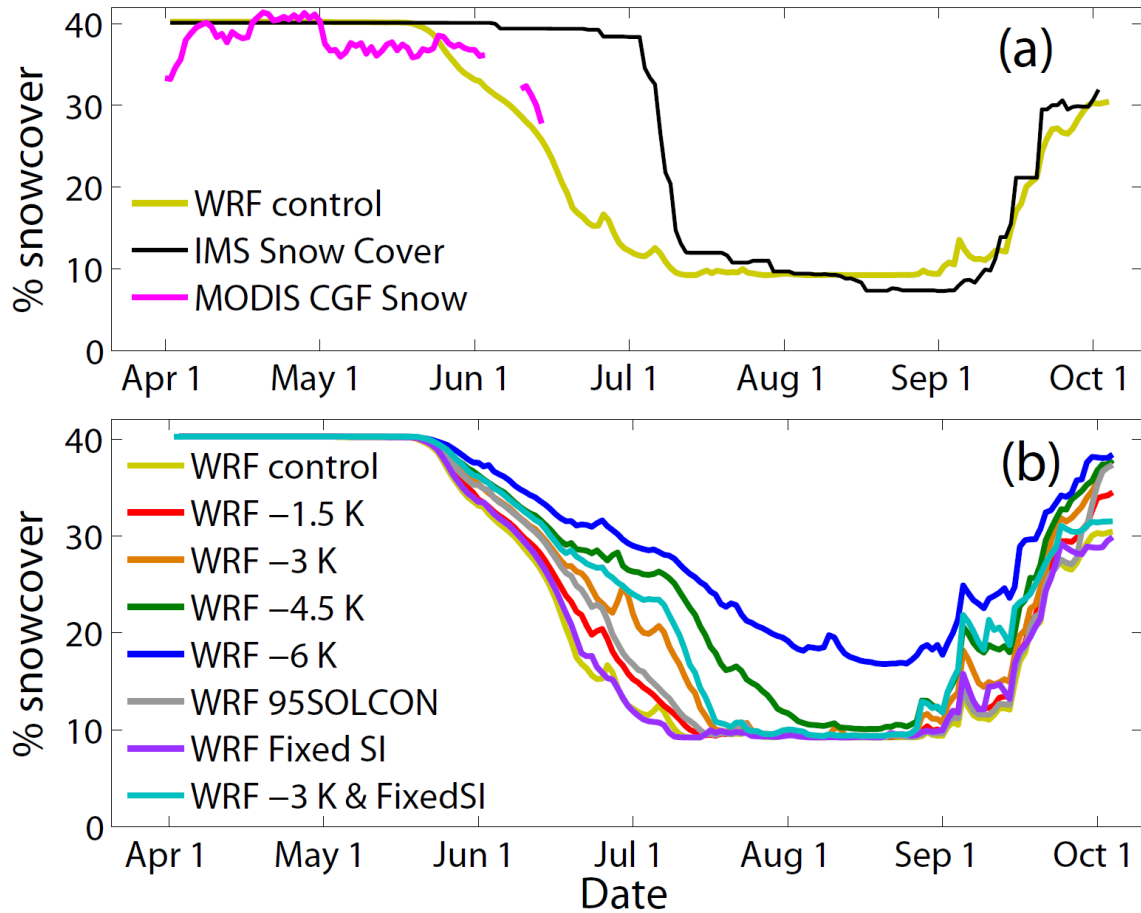


Figure 2.6. (a) Six month time series of IMS, MODIS CGF, and WRF-modeled snow cover extent expressed as a % of inner domain area. (b) Time series of snow cover % of the inner domain for WRF control run and WRF sensitivity tests.

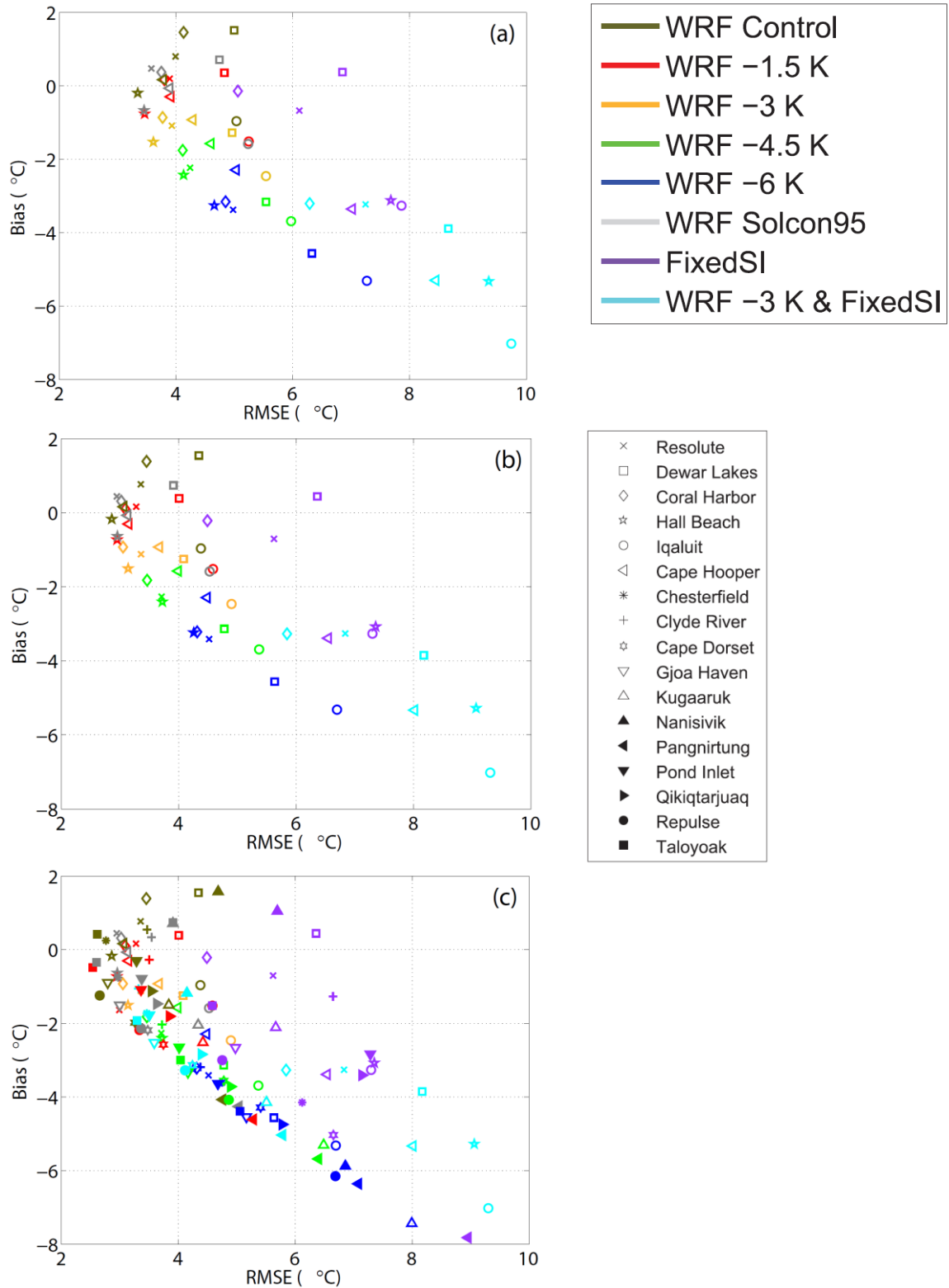


Figure 2.7. (a) Bias versus RMSE between station and WRF for 2m temperature (6 hourly) for April-September 2005, (b) daily average temperature for same stations, and (c) additional stations with daily average temperature records.

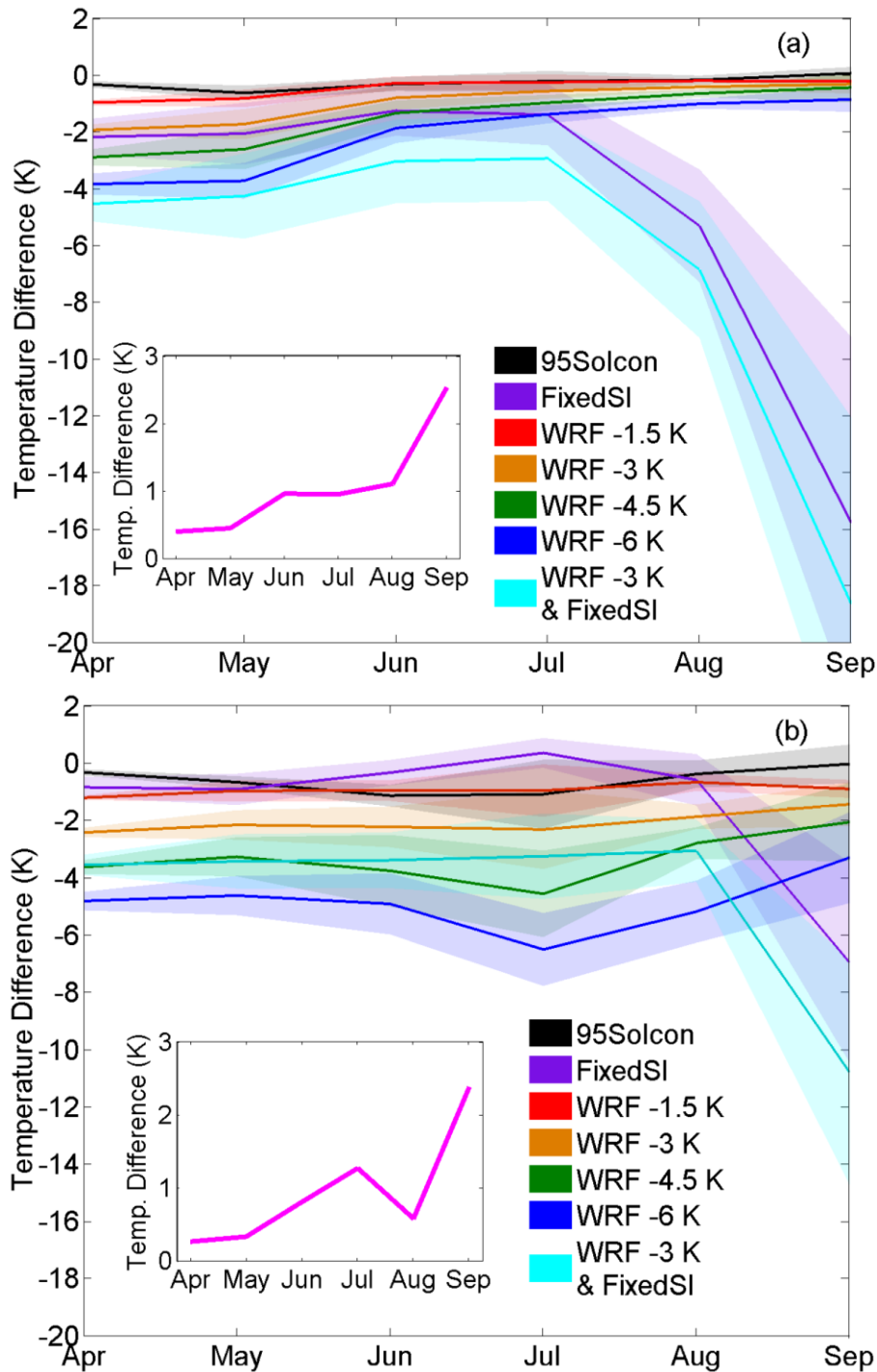


Figure 2.8. Monthly average temperature difference between WRF Control Run and sensitivity experiments for grid cells at elevations between (a) 0 and 0.5m (predominantly ocean grid points) and (b) 0.5m and 2900m (land only grid points). Insets have same axes as main plots, and show the difference between the sum of the WRF 3K run and FixedSI run ($[WRF_3\ K] + [FixedSI]$), and the WRF 3K and FixedSI run ($[WRF_3\ K]$ and $[FixedSI]$). Positive values indicate that the $[WRF_3K]$ and $[FixedSI]$ run has a greater cooling effect than the sum of the constituent parts run independently.

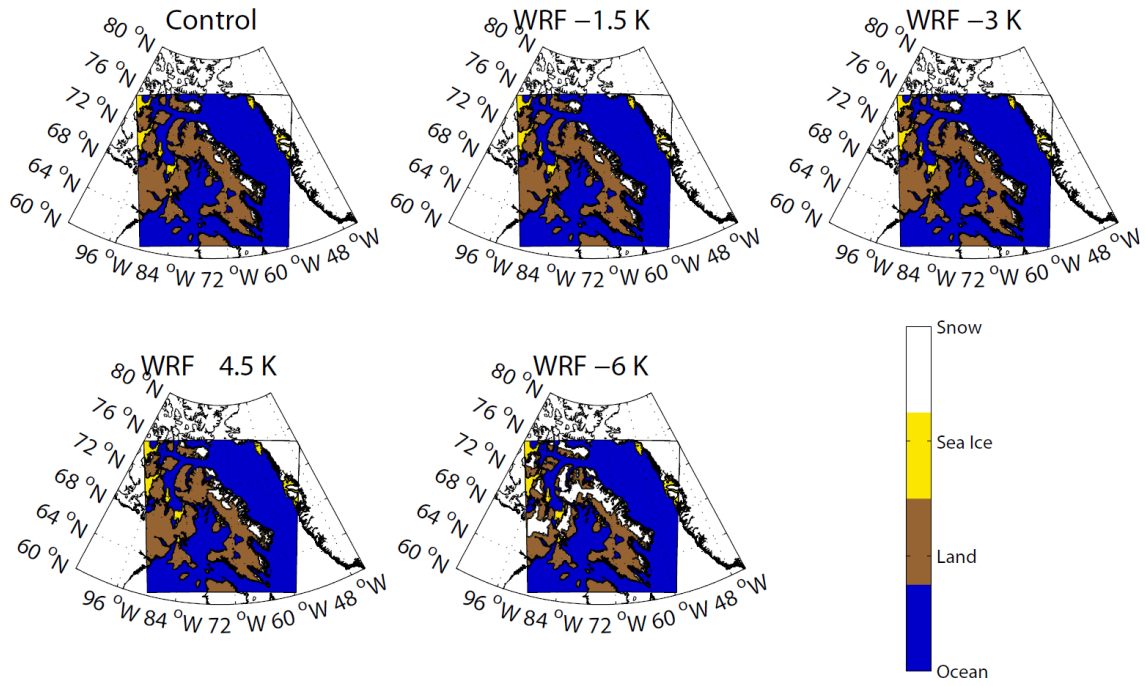


Figure 2. 9. Minimum snow extent reached for each cooling experiment.

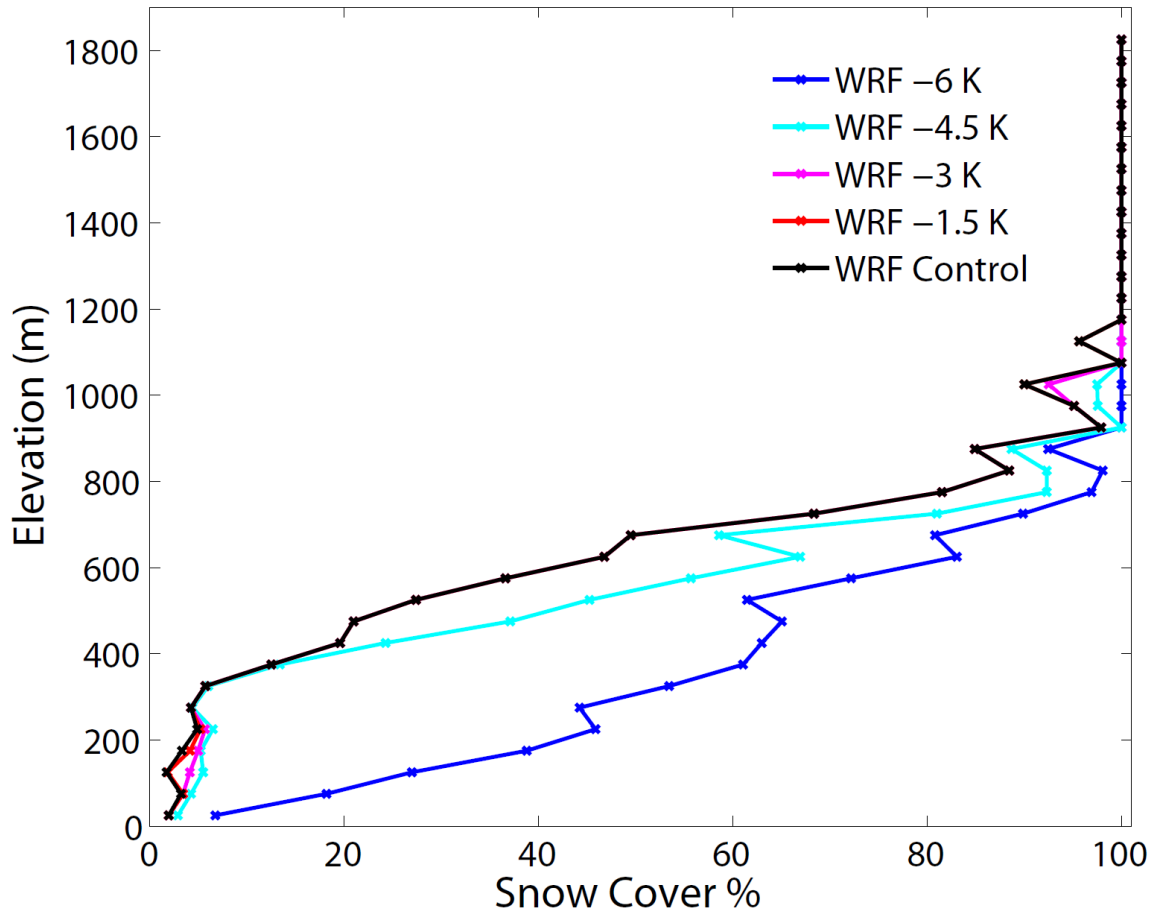


Figure 2.10. Fraction of snow-covered area (based on $\geq 50\%$ threshold for each grid cell snow cover) for elevation bands, in 50 m elevation intervals, on the minimum snow extent day, and excluding Greenland and latitudes south of 66°N .

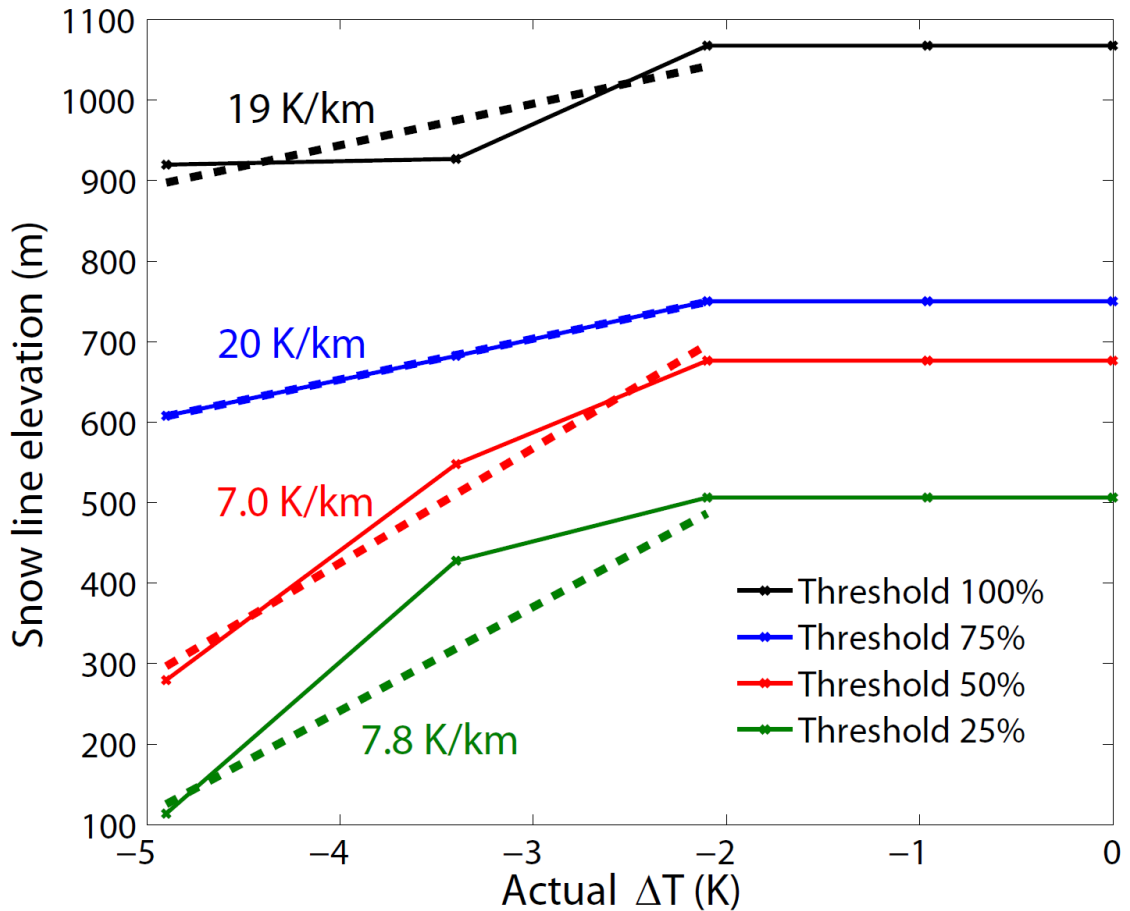


Figure 2.11. Minimum snow line elevation, as defined by the threshold of how much of each elevation band is covered in snow, as a function of average 6 month temperature difference between the Control Run and the given cooling experiment. The associated lapse rates found from the slope of the best fit line to the coldest three points are shown for each curve.

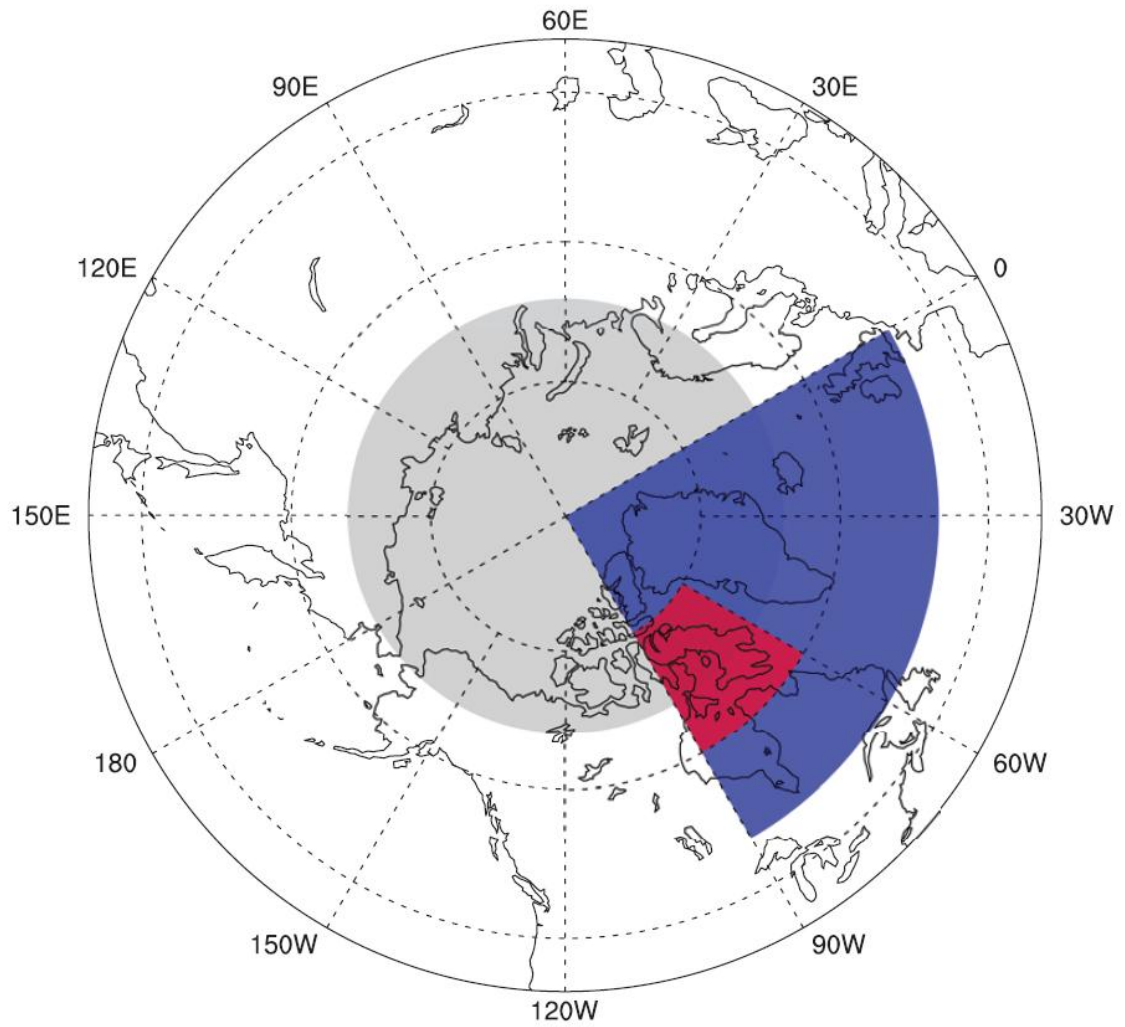


Figure 3.1. Map showing Arctic region (north of 66°N) in grey, North Atlantic (NA) region (270°W–360°W, 50°N–90°N) in blue, and the Baffin Island region (270°W–300°W, 60°N–75°N) in red.

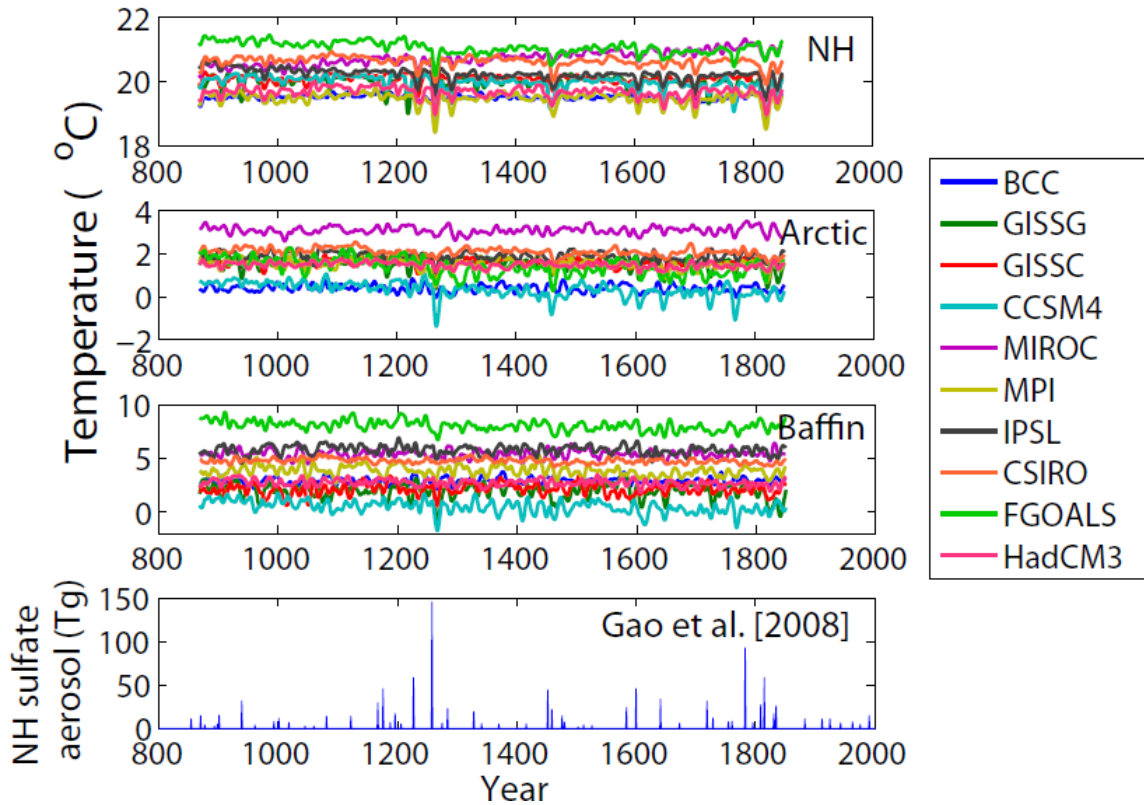


Figure 3.2. JJA temperature time series for each last millennium model simulation for the Northern Hemisphere, Arctic (north of 66°N) land and ocean, and Baffin Island (land only). Data are filtered with a third-order low-pass Butterworth filter with a cutoff frequency of 15 years. The bottom panel shows the total Northern Hemisphere stratospheric sulfate aerosol ejection (Tg) [Gao *et al.*, 2008]. GISS models have been corrected for drift in the first 500 years.

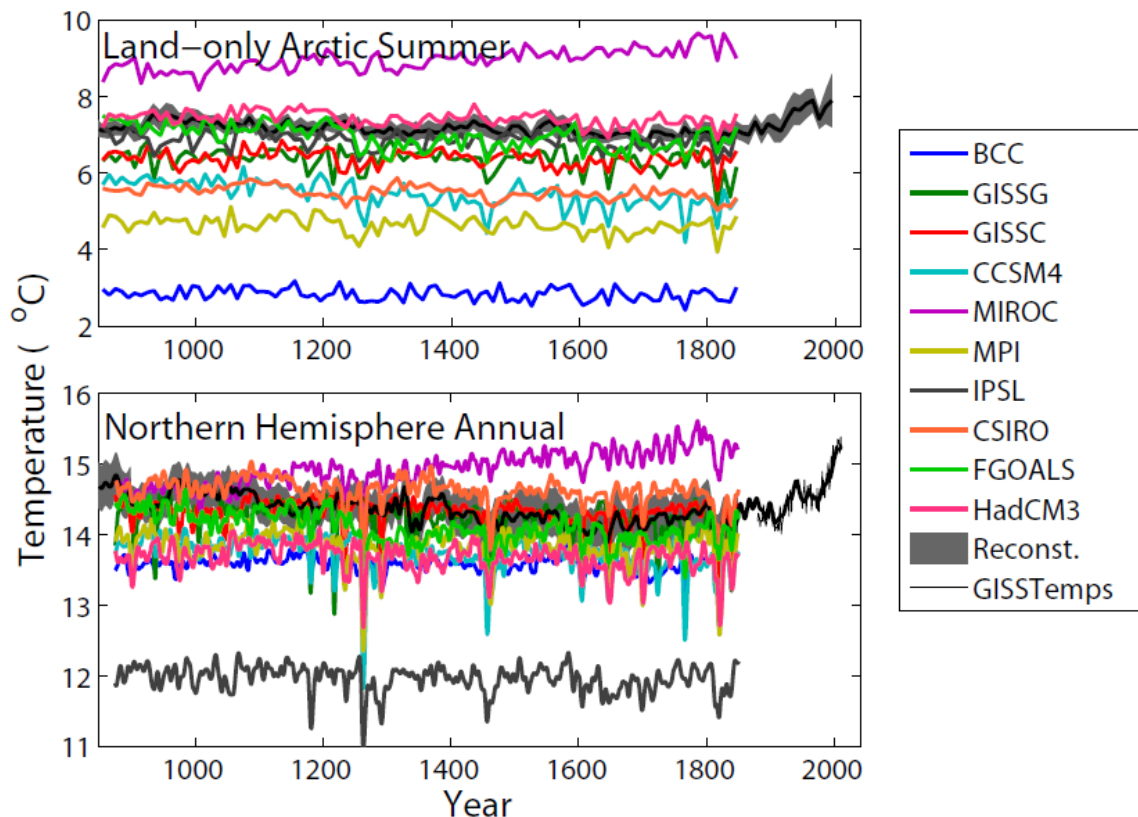


Figure 3.3. Comparison of paleoclimate temperature reconstructions to PMIP3 for the (top) Arctic summer (JJA) land-only north of 60°N and (bottom) NH annual temperature reconstruction. GISS models have been corrected for drift in the first 500 years. Arctic reconstruction is from *Kaufman et al.* [2009] and compared to PMIP3 decadal averages. NH reconstruction is from *Mann et al.* [2009] and compared to 10 year low-pass Butterworth filtered PMIP3 data. GISS temperatures are derived from land and ocean station temperature anomalies for the NH from <http://data.giss.nasa.gov/gistemp/>. They were then converted to absolute temperature with the Jones et al. [1999] 1961–1990 base period average (14.6°C).

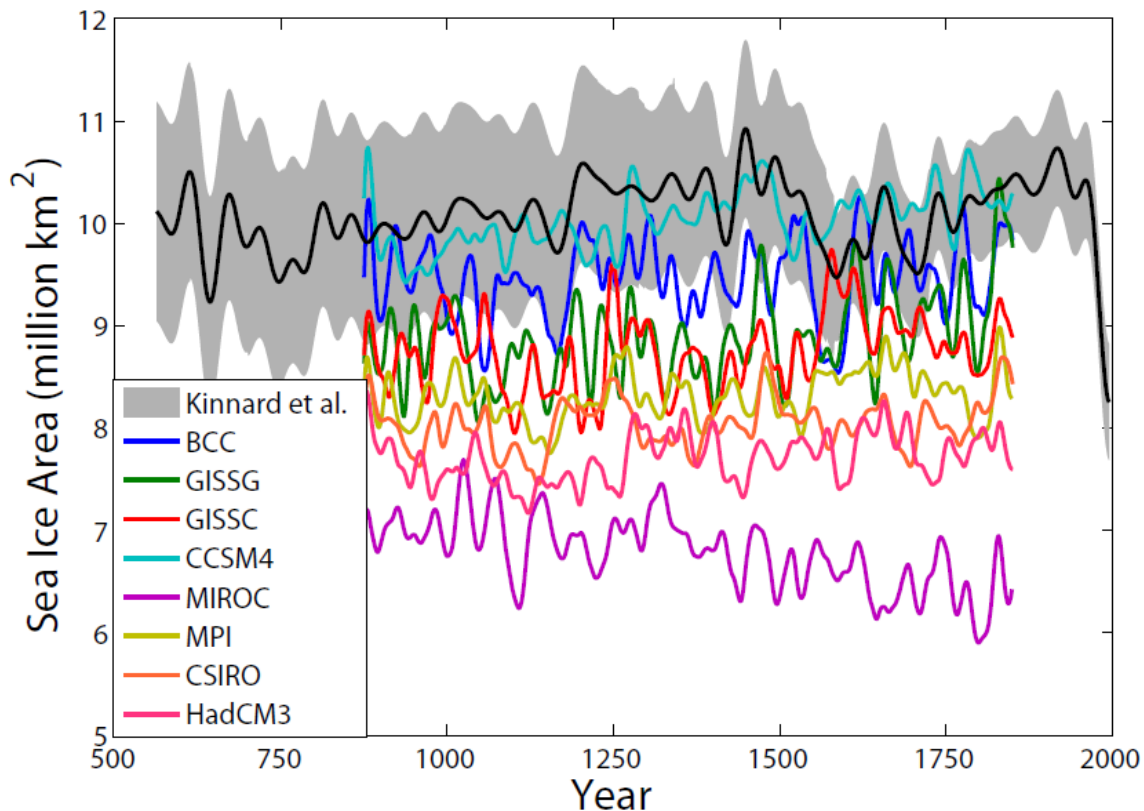


Figure 3.4. NH late summer (August) sea ice extent (millions km²) for PMIP3 simulations filtered with a third-order Butterworth 40 year low-pass filter compared to *Kinnard et al.* [2011] 40 year smoothed reconstruction of sea ice extent based on 69 proxy records. GISS models are corrected for first 500 years of drift. PMIP3 models calculated using 15% ice cover threshold (any cell $\geq 15\%$ ice cover is considered fully covered, whereas anything $< 15\%$ cover is considered open ocean).

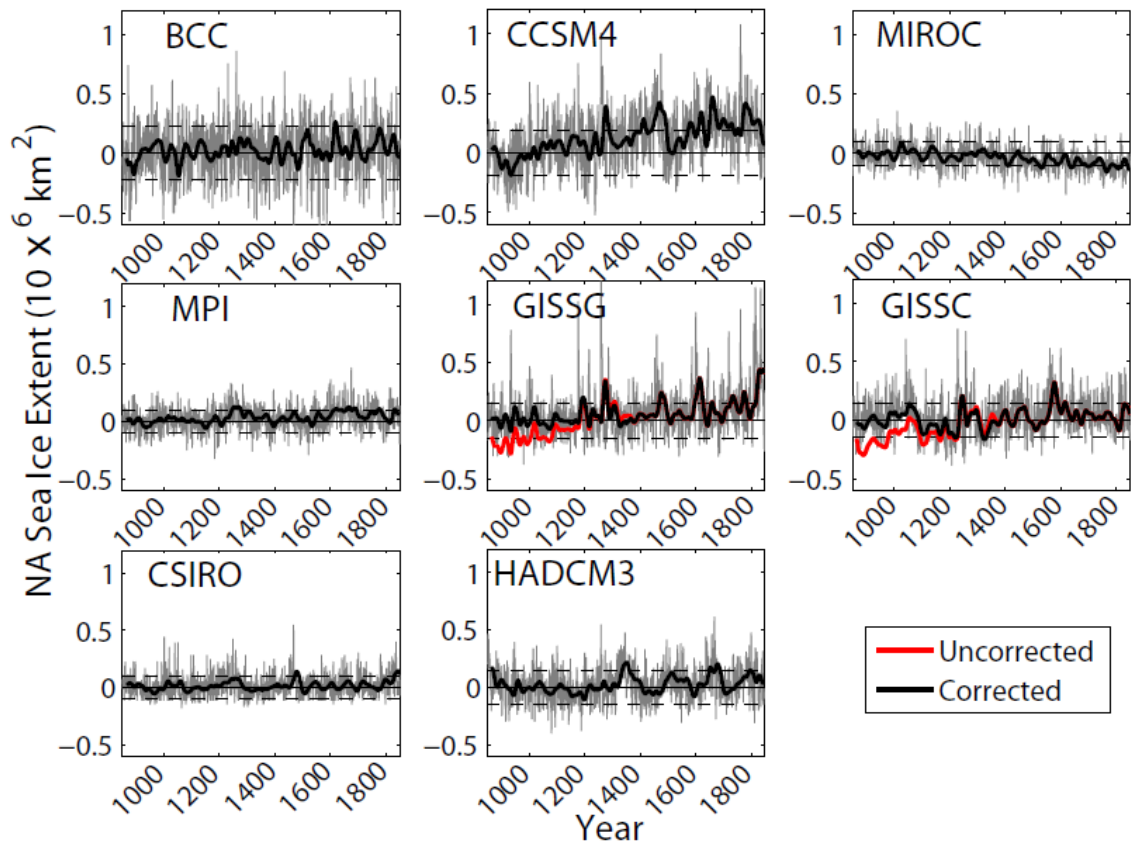


Figure 3.5. Anomaly of minimum annual North Atlantic sea ice extent (grey) overlain with 40 year low-pass filtered series (black) with respect to the reference period 850–1150 C.E. (a time with low volcanic activity). Dashed lines show standard deviation of sea ice extent of reference. Models do not show centennial-scale expanded sea ice in this region after multiple closely spaced eruptions in the late thirteenth century. Sea ice extent is calculated with a 15% grid cell coverage threshold for full ice cover versus open ocean, and the drift-corrected and uncorrected GISS curves are shown.

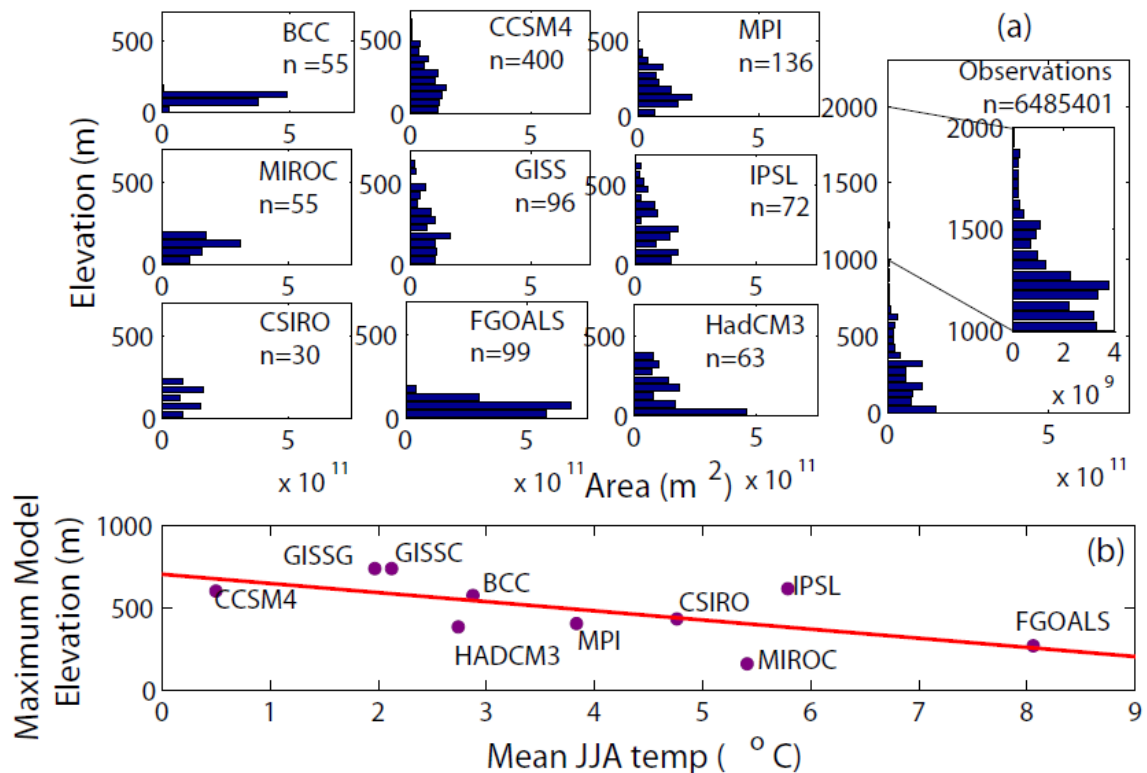


Figure 3.6. (a) Histograms of Baffin Island grid cell elevation distribution in terms of area represented for each model and the observed digital elevation retrievals from the GTOPO30 data set (<http://earthexplorer.usgs.gov/>). The GTOPO30 observations panel inset emphasizes the high elevations present in reality on Baffin Island. Number of grid cells in the Baffin Island region is denoted with n . Few models represent the Baffin Island plateau elevation range of 400–700 m, critical to snow expansion and persistence. (b) Maximum model elevation as a function of mean model summer (JJA) 2m temperature over Baffin Island land from 850–1850 C.E. The red curve shows the best fit linear regression. There is a relationship between maximum summer temperatures and the model topography of the island. GISS models have been corrected for drift in the first 500 years.

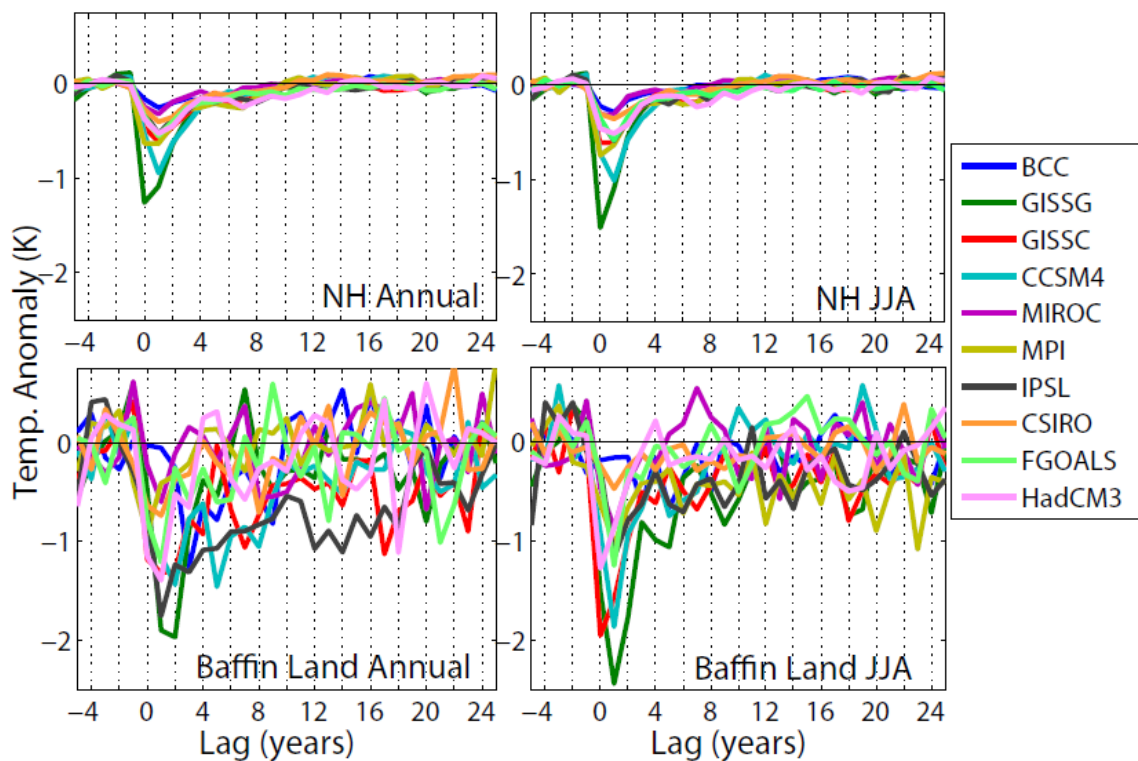


Figure 3.7. Superposed epoch analysis of NH annual, summer (JJA), Baffin Island (land only) annual, and JJA average temperature response to the top 10 eruptions in the last millennium. Anomaly is relative to the 5 year average before eruptions. GISS models have been corrected for drift in the first 500 years.

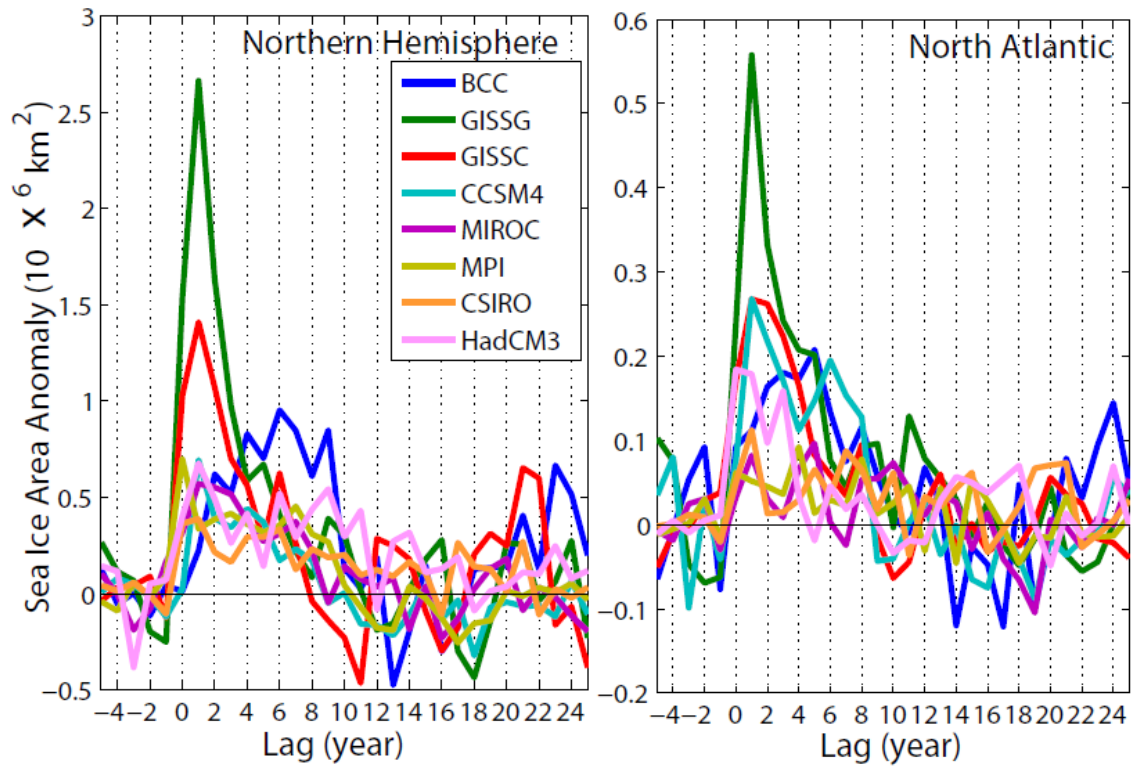


Figure 3.8. Superposed epoch analysis for top 10 eruptions in the last millennium (Table 3.2), showing Northern Hemisphere and North Atlantic September sea ice area. Anomaly is with respect to the mean of 5 years prior to the eruptions. Note on the different scales on the y axis. GISS models are corrected for the first 500 years of drift.

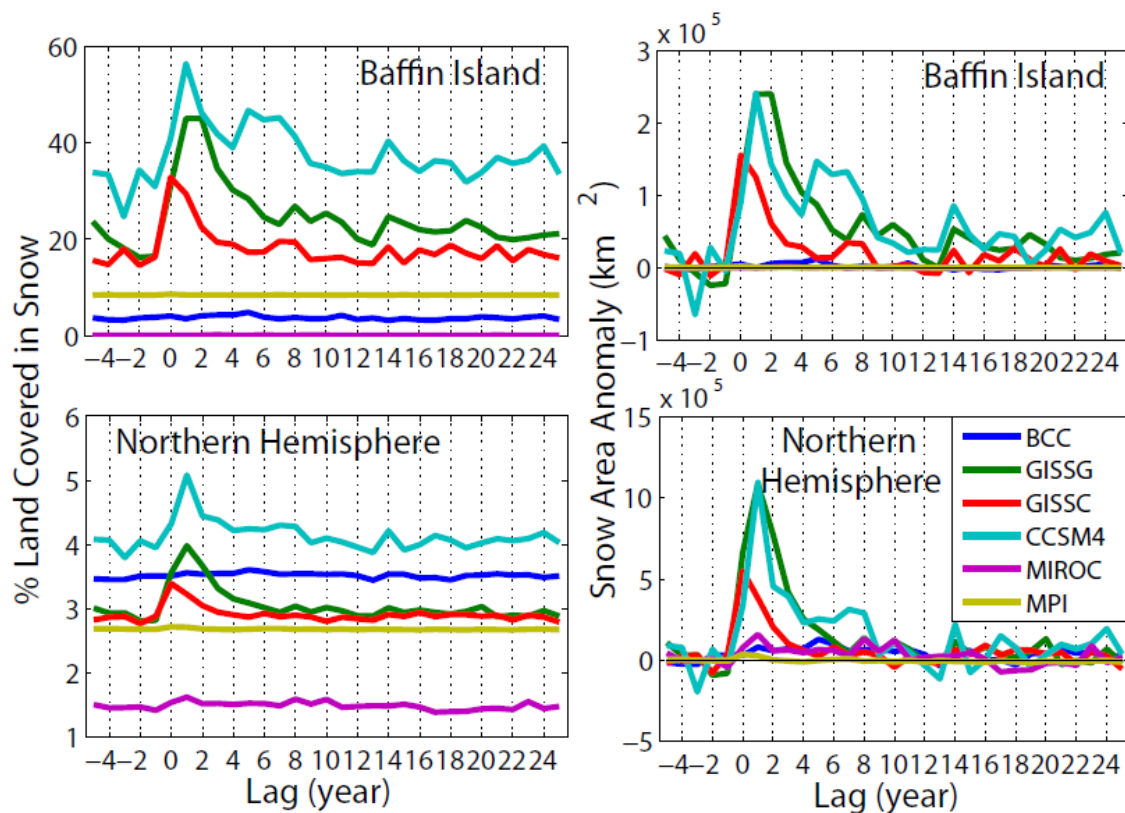


Figure 3.9. Superposed epoch analysis for the top 10 eruptions in the last millennium (Table 3.2). Panels show snow area coverage in the Baffin Region (270°W – 300°W , 60°N – 75°N) and for the Northern Hemisphere expressed as the percent of the total land area covered in snow at the minimum annual extent in the left panels. The right panels show the snow area anomaly with respect to the mean of the 5 years prior to the eruptions for the same regions. Lag of 0 represents the year of the eruption. Note on the different scales on the y axes. GISS models have been corrected for drift in the first 500 years.

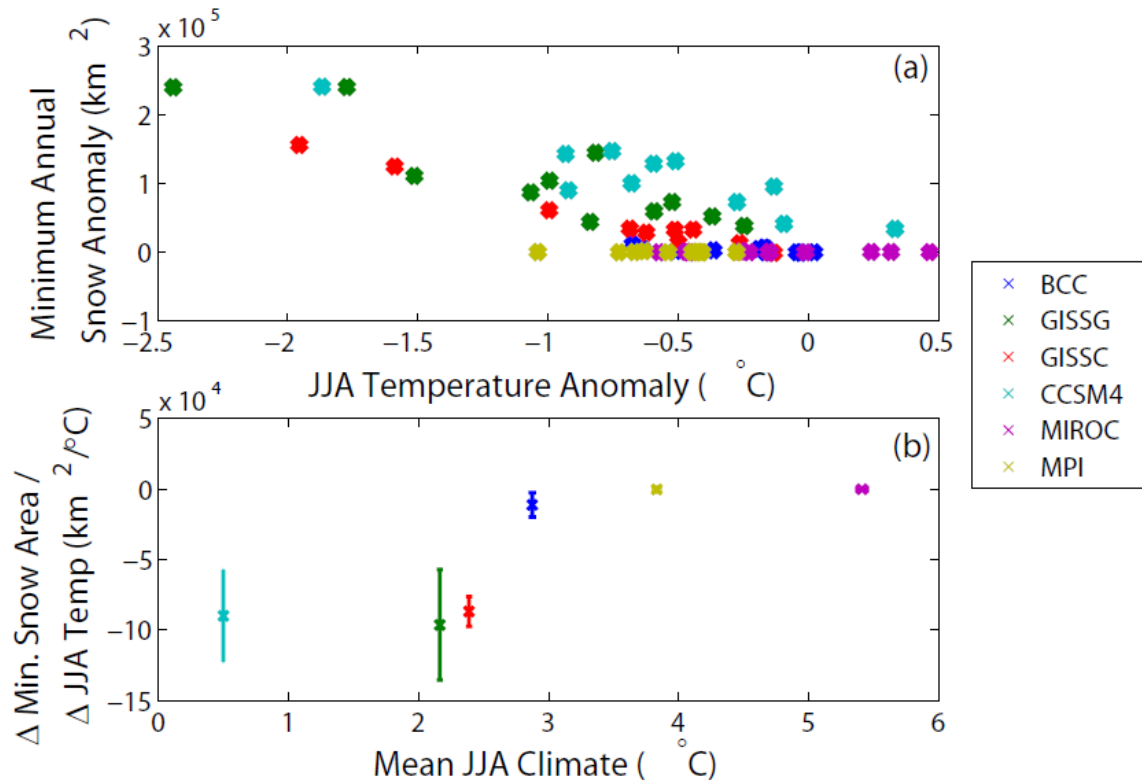


Figure 3.10. SEA minimum annual Baffin Island snow cover anomaly as a function of SEA JJA temperature anomaly for the 10 years following the top 10 eruptions (lag years 1–10 in Figures 3.9 and 3.7, respectively). Anomalies are with respect to the SEA values for the 5 years prior to the eruptions (lag years -5 to -1 in Figures 9 and 7). GISS models have been corrected for the first 500 years of drift. (a) Ordinate value is calculated as the slope for each model. (b) Magnitude of snow cover expansion on Baffin Island during summer cooling after the top 10 eruptions, plotted against the mean JJA Baffin Island climate for each model. Error bars show 95% confidence level. GISS models previously corrected for the first 500 years of drift.

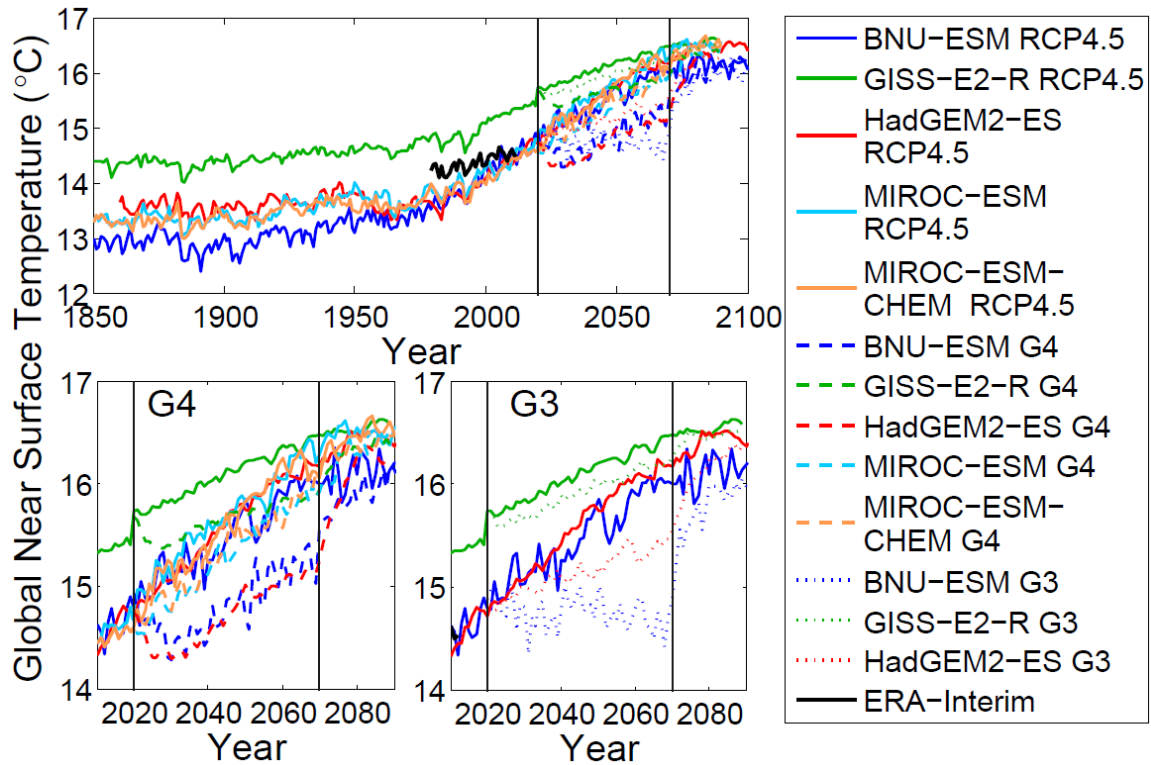


Figure 4.1. Global annual average temperatures, including land and ocean. GISS-E2-R and HadGEM2-ES curves show the ensemble mean. Bottom panels show G4 and G3 separately and zoomed in during the geoengineering period. Solid lines show the control run (RCP4.5), dashed lines the G4 experiments and dotted lines the G3 experiments. The solid black curve shows the global average ERA Interim 2 m temperature. Vertical lines indicate the start and finish of the geoengineering experiments at 2020 and 2070.

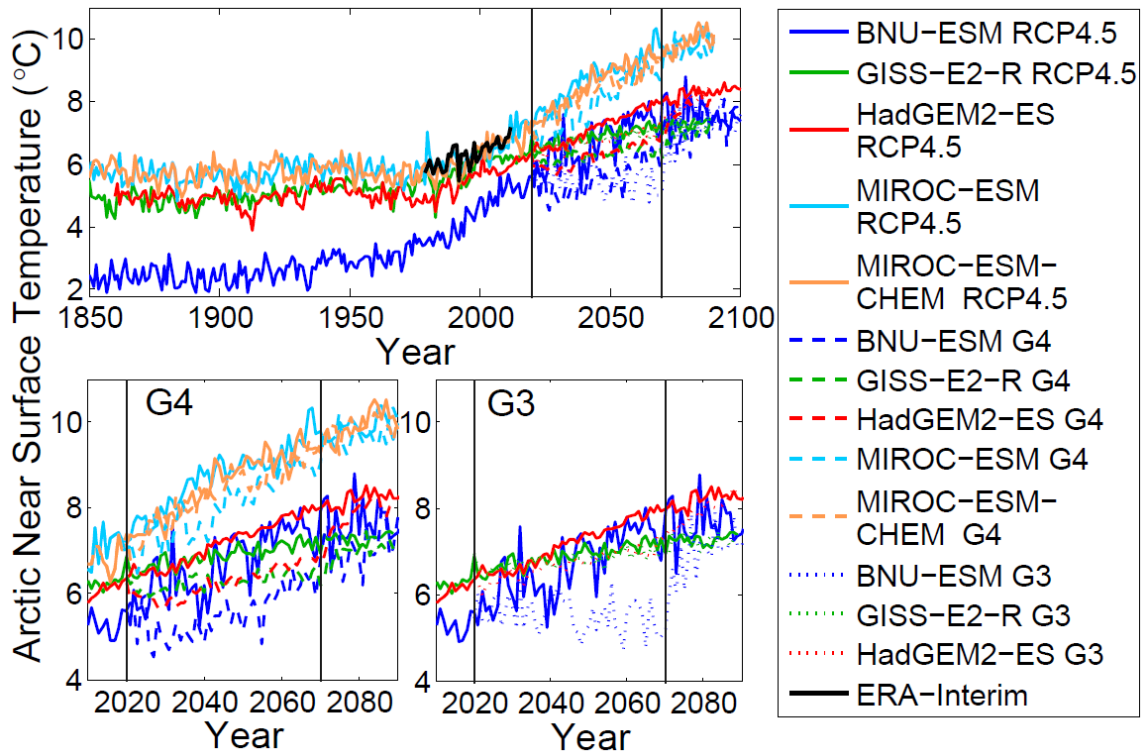


Figure 4.2. June-July-August (JJA) average temperature for Arctic (North of 60°N), including land and ocean. GISS-E2-R and HadGEM2-ES curves show the ensemble mean. Bottom panels show G4 and G3 separately and zoomed in during the geoengineering period. Solid lines show the control run (RCP4.5), dashed lines the G4 experiments and dotted lines the G3 experiments. The solid black curve shows the ERA Interim 2 m temperature result for the Arctic ($60\text{-}90^{\circ}\text{N}$). Vertical lines indicate the start and finish of the geoengineering experiments at 2020 and 2070.

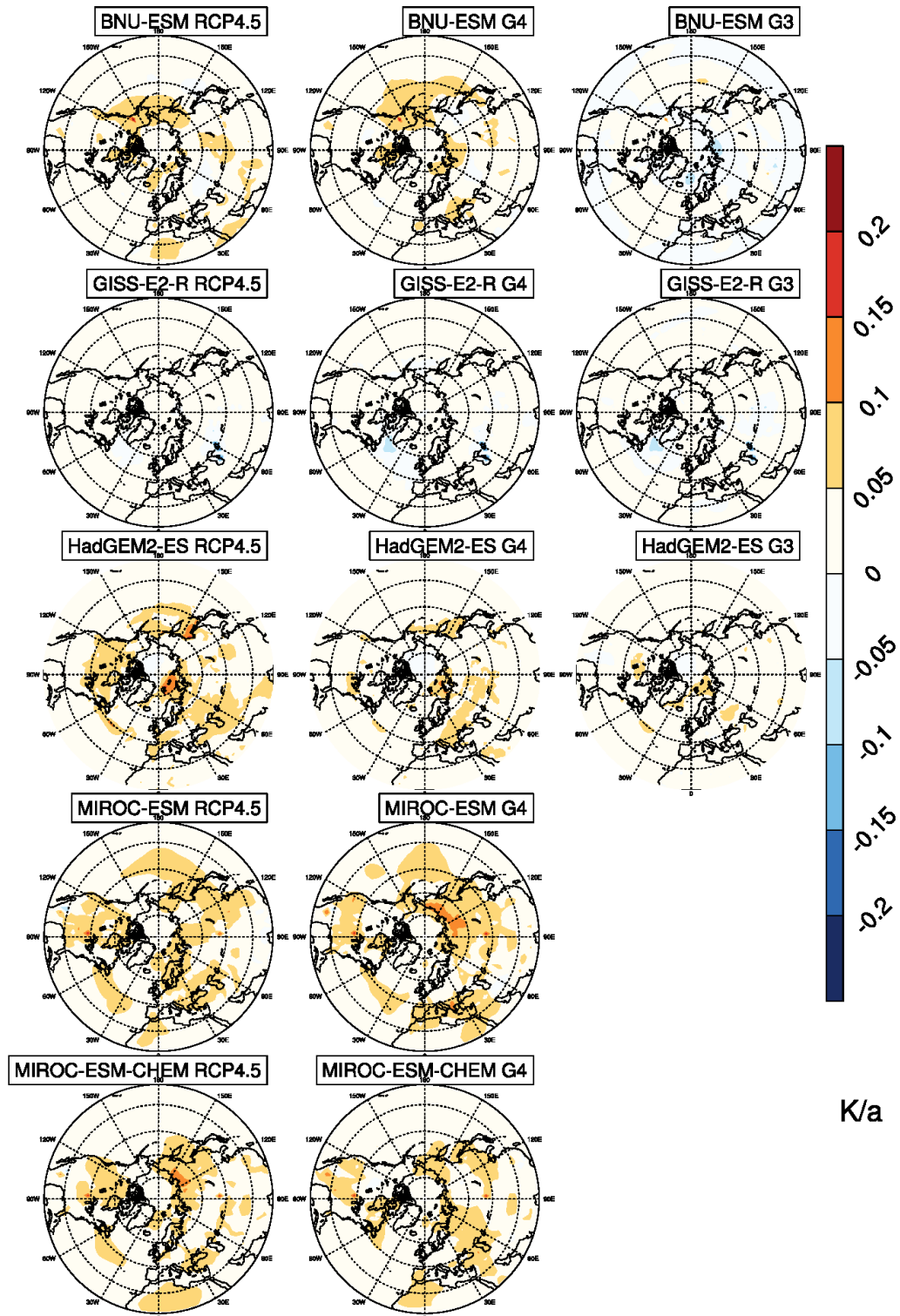


Figure 4.3. JJA temperature trend from 2030 to 2070 for RCP4.5, G3, and G4 simulations. The rate of warming is generally similar in the geoengineering runs to that in the Control runs, although the absolute temperatures are slightly cooler (Figure 4.2).

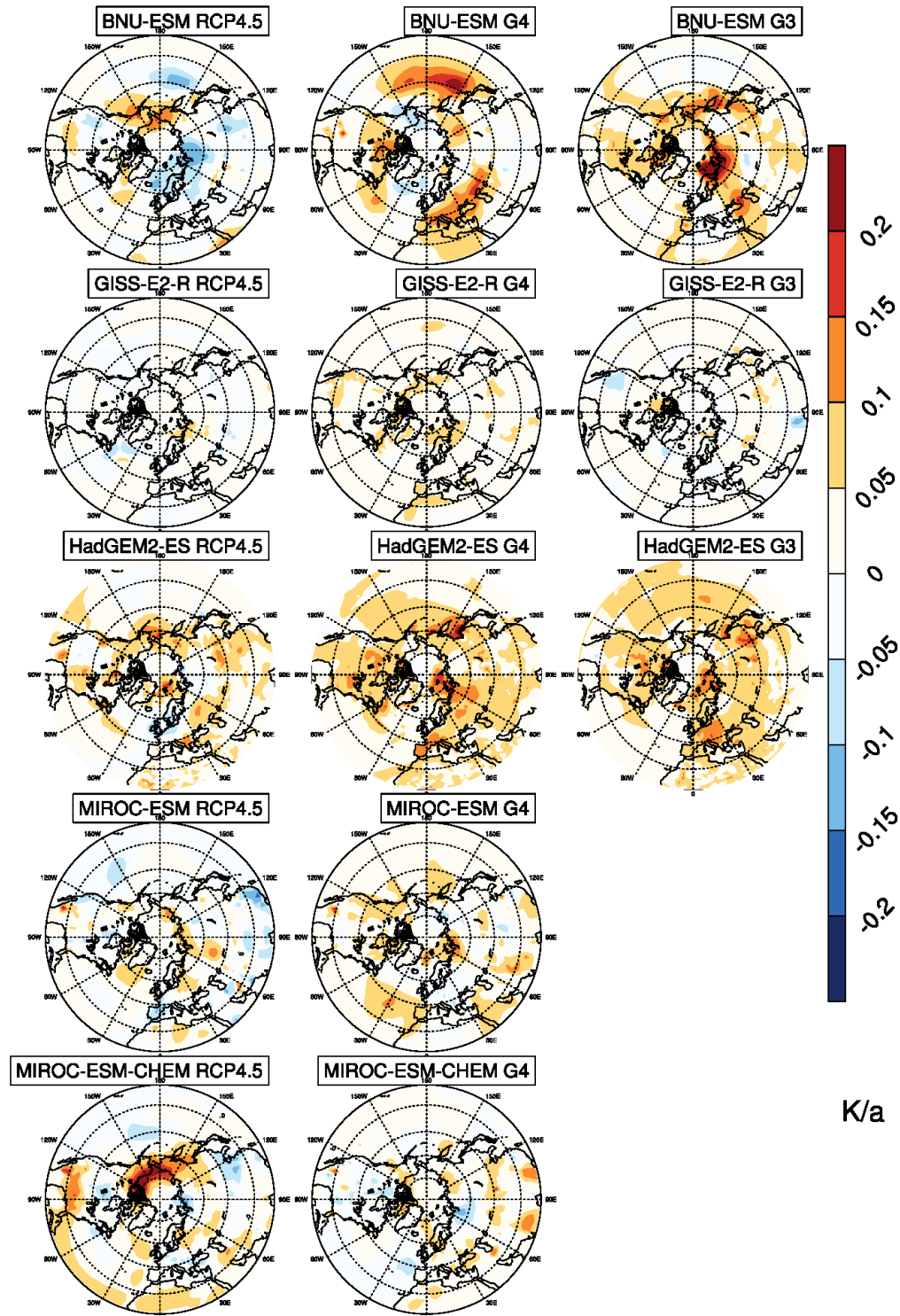


Figure 4.4 JJA temperature trend from 2070 to 2090 (two decades of recovery after geoengineering) for RCP4.5, G3 and G4 simulations. The rate of warming is generally faster in the geoengineering runs than it is in the Control run signifying a fast rebound of temperatures.

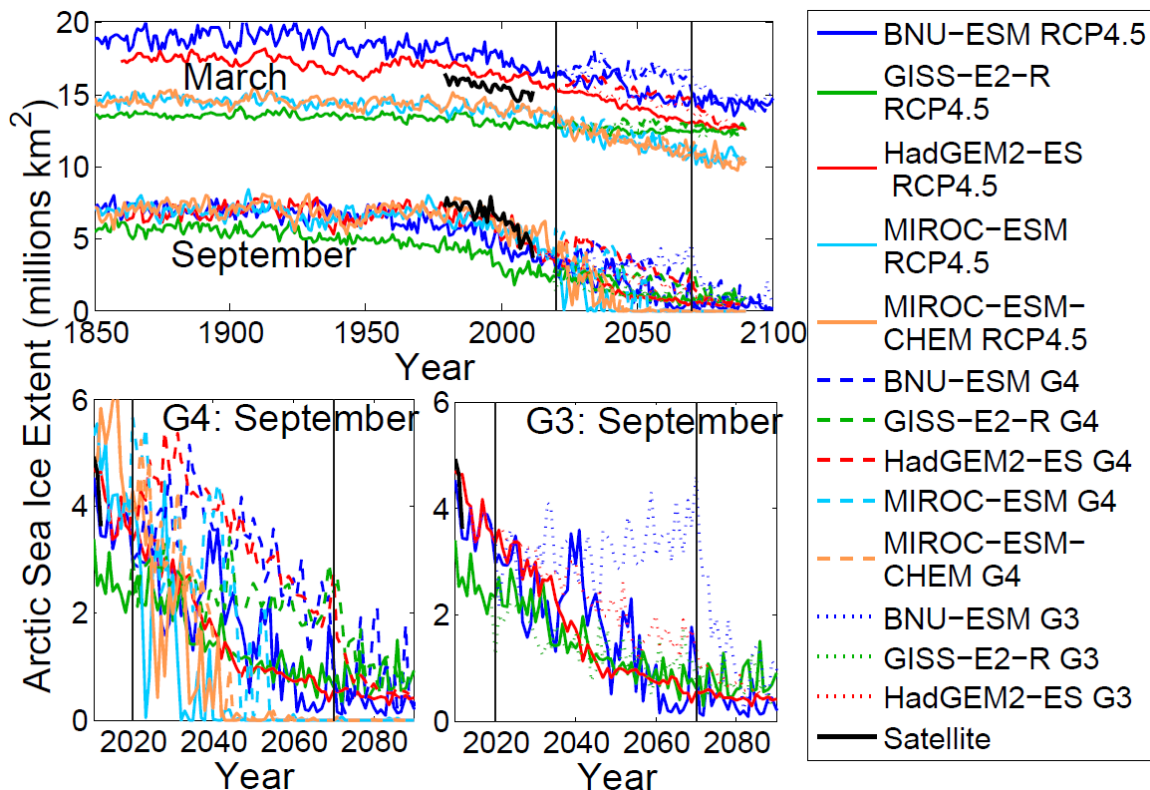


Figure 4.5. Historical and projected maximum (March) and minimum (September) annual sea ice extent for all available models of the G3 and G4 simulations and satellite observations from 1979-2012. Results for G3 and G4 are shown zoomed in for the period 2010 to 2090. Solid lines show the control RCP4.5 run, dashed lines the G4 runs, and dotted lines the G3 runs. MIROC-ESM and MIROC-ESM-CHEM models lose multi-year sea ice before 2050, and the other models approach total sea ice loss by the end of the 21st century, even with geoengineering implemented. Vertical lines denote the beginning and end of the geoengineering experiments (2020-2070).

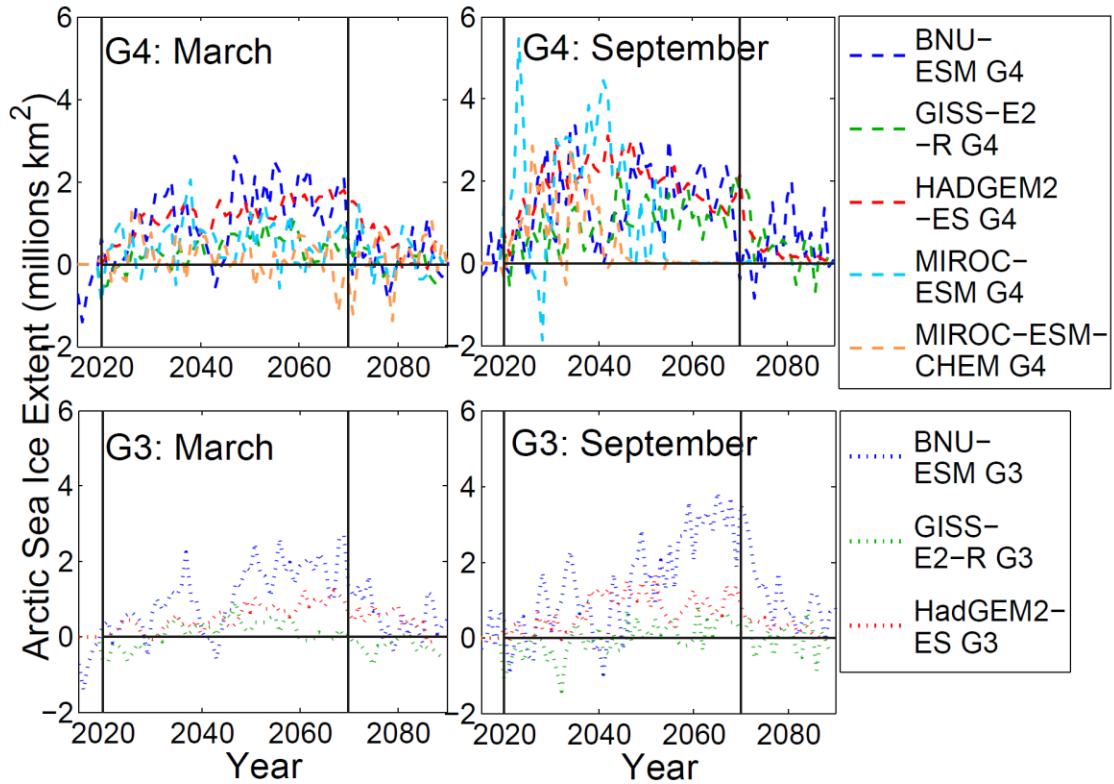


Figure 4.6. Difference of Arctic sea ice extent between experiment run and Control (RCP4.5) for maximum (March) and minimum (September). Dashed lines show G4 experiments; dotted show G3. Most models show that the G3 and G4 maintain more sea ice than the control run, but this quickly plummets back to control levels after geoengineering ceases at 2070.

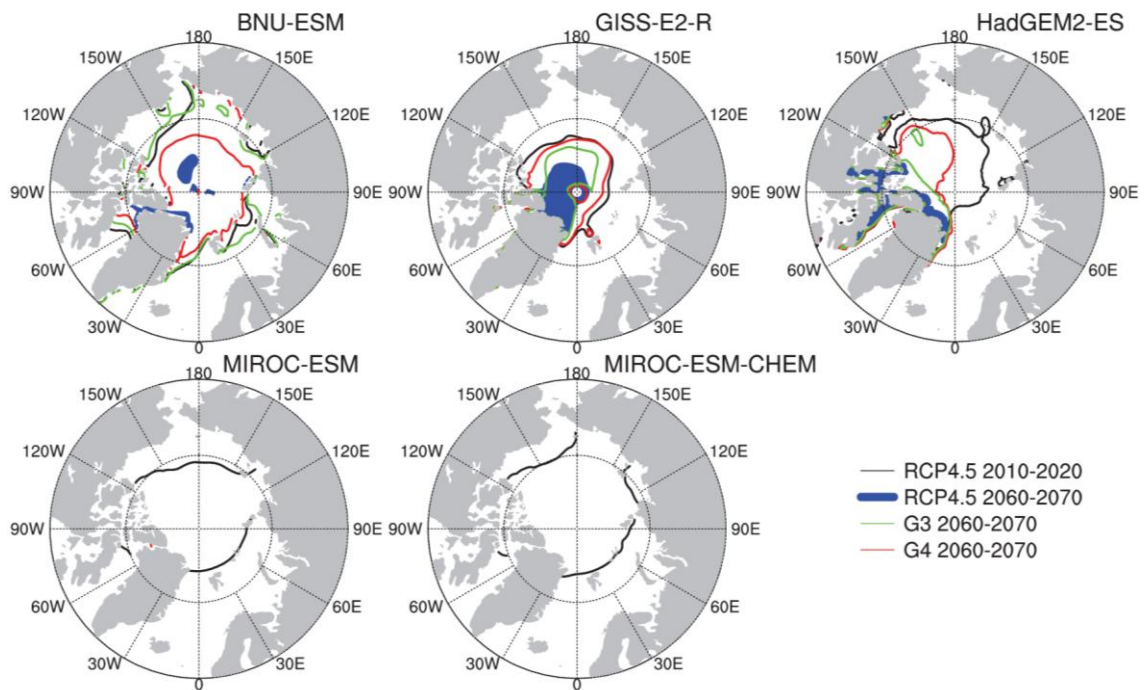


Figure 4.7. Mean September (minimum) sea ice extent in the RCP4.5 simulation before geoengineering begins (2010-2020, in black), and from 2060-2070 in the RCP4.5 (blue filled), G4 (red) and G3 (green) scenarios. MIROC-ESM and MIROC-ESM-CHEM melt virtually all ice by 2060-2070 regardless of the cooling by geoengineering.

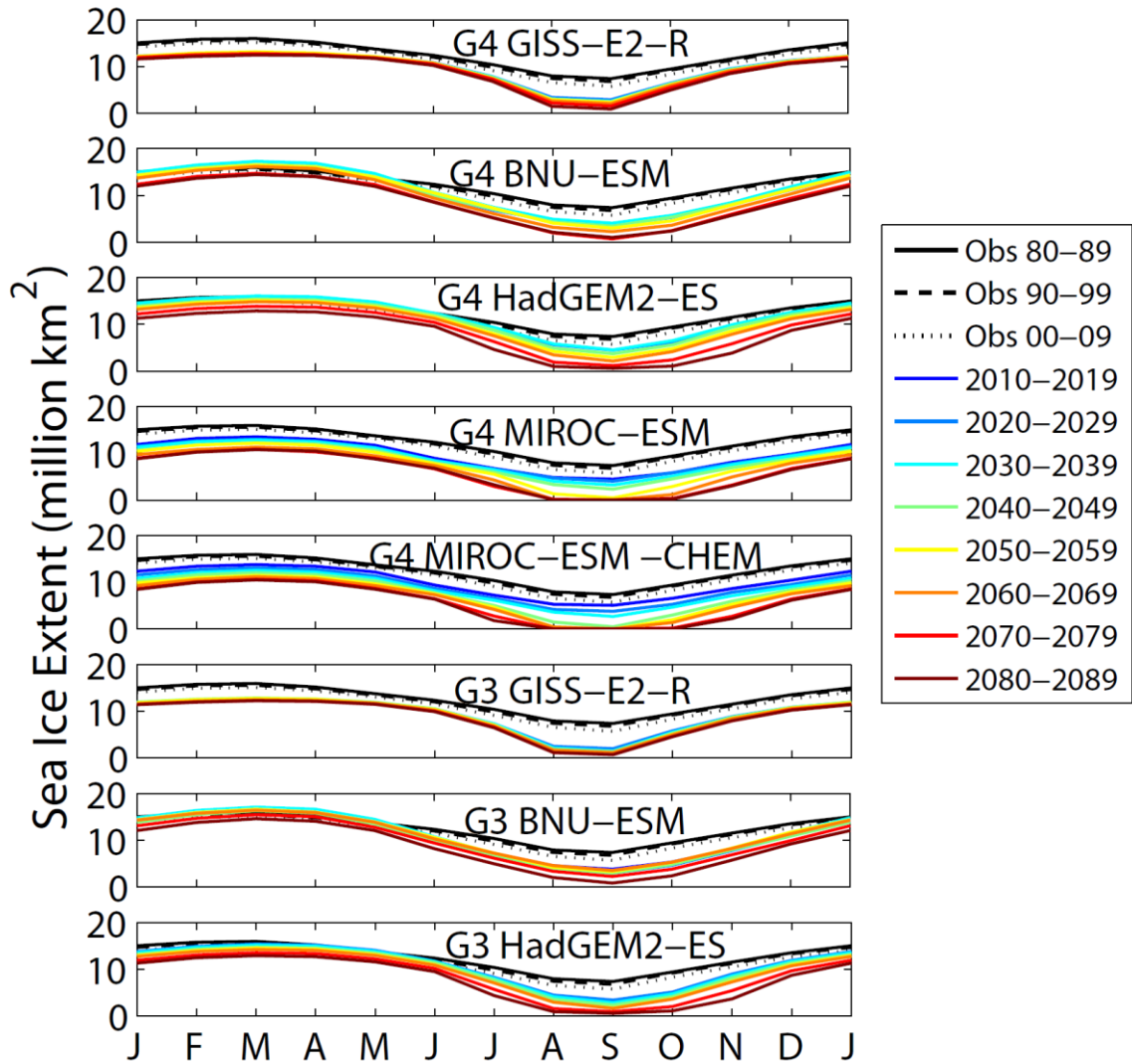


Figure 4.8. Sea ice extent for G4 and G3 simulations, for decadal intervals. The control run is not removed. Extent is defined as grid cells covered by more than 15% ice. Most models show progressively decreasing sea ice area from 2020 to 2090, and exhibit a lengthening of the melt season.

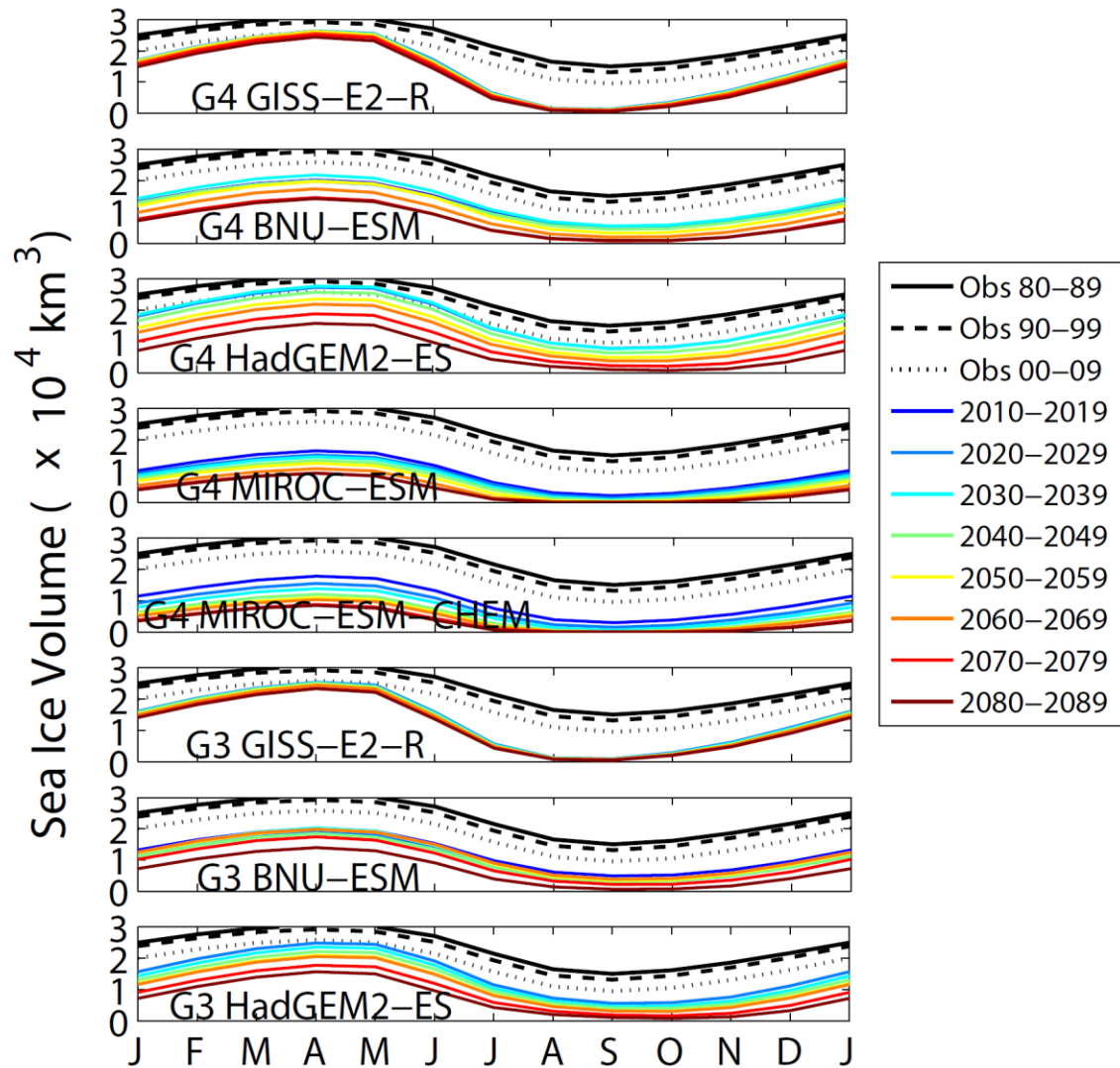


Figure 4.9. Decadally-averaged sea ice volume from 2010 to 2090. The control has not been removed. Melt seasons last longer, and ice volume approaches zero as the decades progress. Average 2005-2012 observed values are shown in the black curve. Sea ice volume observations are calculated using the Pan-Arctic Ice Ocean Modeling and Assimilation System [PIOMAS, Zhang and Rothrock, 2003] developed at Applied Physics Lab/Polar Science Center.

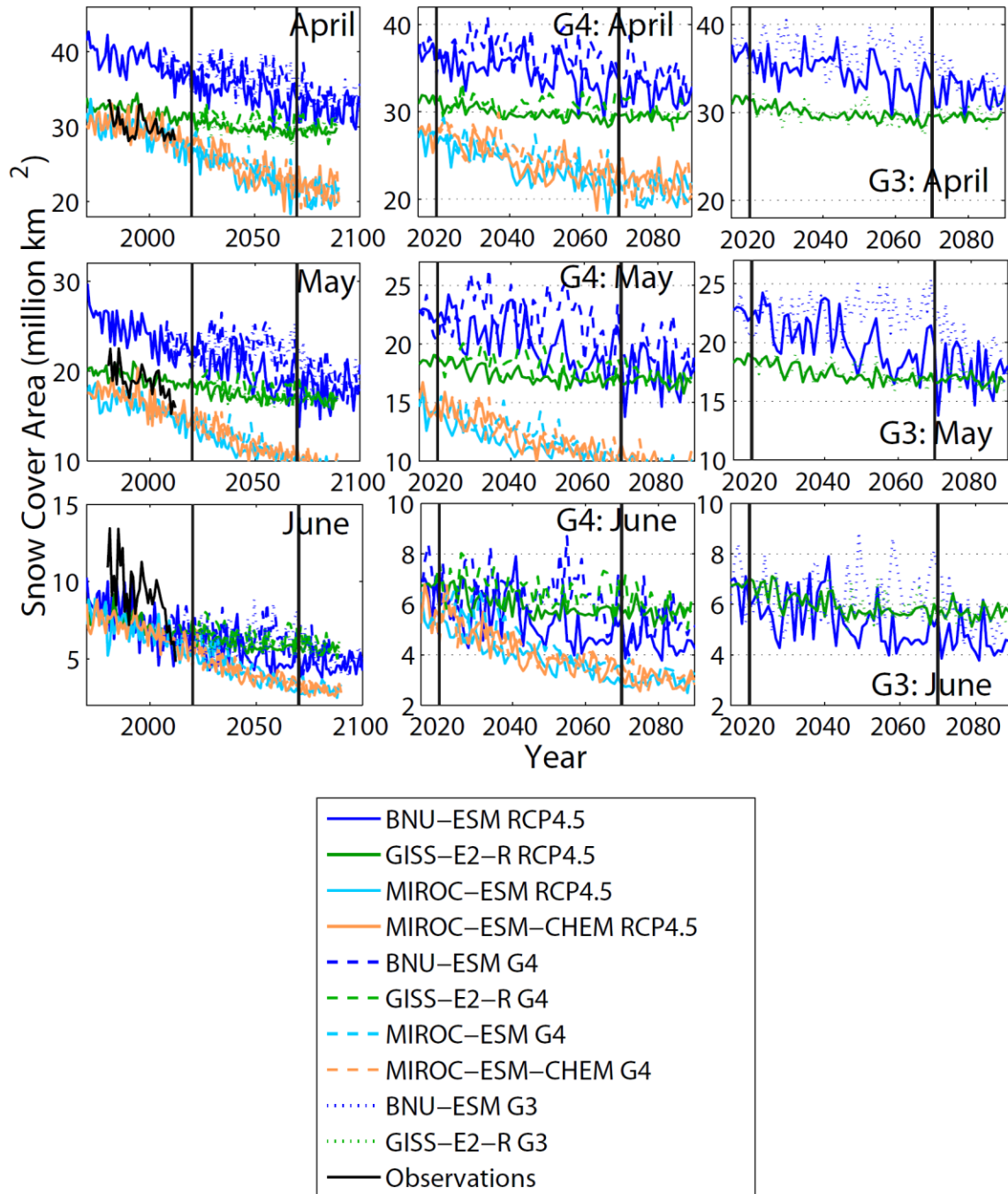


Figure 4.10. Spring (April-June) snow cover extent (> 50% coverage) for the Northern Hemisphere. During these months, snow extent is mostly limited to the Arctic. HadGEM2-ES fractional snow cover data are not available. Snow extent is increased during the G3 and G4 experiments, most for BNU-ESM, followed by GISS-E2-R and MIROC-ESM/MIROC-ESM-CHEM which show only slight snow extent increases. After 2070, snow extents in the G3 and G4 experiments decrease quickly back to RCP4.5 values.